OXIDATION IN MASS SPECTROMETRY: APPLICATIONS IN ANALYTE DETECTION IN COMPLEX MIXTURES

A Dissertation Presented for the

Doctor of Philosophy

Degree

The University of Tennessee, Knoxville

Lindsay P. Brown

December 2024

DEDICATION

To those who helped mold me into the analytical chemist I am today

ACKNOWLEDGEMENTS

I'd like to thank my PI, Dr. Shawn Campagna, for the resources he provided all these years. I am grateful that you let me pursue research that didn't necessarily align with the goals of the lab, simply because you knew I was passionate about it. I am very thankful to my committee members, Dr. Thanh Do, Dr. Michael Best, and Dr. Brynn Voy, for their continued support. Dr. Do, thank you for teaching me the most important class I've ever taken – Mass Spectrometry and Surface Characterization. Much of the information in this document is based on my learning from your class. I am also forever grateful for the UT-ORII SMaRT Program for funding me for 10 out of my 11 semesters spent in graduate school. I feel very fortunate to have had the opportunity to directly mentor nine talented and driven SMaRT interns over the years.

I would like to acknowledge the past and present members of the Campagna lab. Dr. Josh Powers, thank you for your kindness, understanding, and support during my first few months in the lab. Without you and the projects you gifted me, I wouldn't have had the opportunity to do research I'm passionate about. To my cohort – Dr. Brittni Woodall, Zane Vickery, and Dr. Wesley Seaton – I am beyond thankful that I we were able to endure this experience together. I wish you all the best in the future and I'm excited to see where your careers take you.

I am also thankful to the many wonderful collaborators I've worked with through the Biological and Small Molecule Mass Spectrometry Core. I'm sincerely thankful that each collaborator placed their trust in me as a mass spectrometrist and analytical chemist. To the Dr. Jennie Ivey lab – I will cherish the time I was able to spend with you all. You were all so kind in your willingness to accept me as an honorary member and you showed me what it felt like to be a valued member of a team – thank you so much for that. To the Dr. Joshua Baccile lab – without you all, there is an entire chapter in this dissertation that wouldn't have been possible. I'm thankful to the entire lab for allowing me to share your resources and space while making me feel welcome. Dr. Baccile, I am so grateful that you took the time to mentor me even though it wasn't your job. To Nick Trybala and Dillon McBee, thank you both for being great friends to me, talking science and research

with me, and being wonderful examples of what a dedicated, hard-working graduate student should be.

To Dr. Hector Castro – you will never understand how much your friendship and support has meant to me. I am so lucky to have had you as my lab manager and mentor. Without you, I wouldn't be here.

It is my firm belief that I owe every future opportunity to two of the most influential mentors I've ever had – my undergraduate research advisor, Dr. Carol Babyak, and my supervisor at Regeneron Pharmaceuticals, Inc., Dr. Stacey Helming. You both played pivotal roles in my career and helped me develop a scientific and personal foundation to stand on. Dr. Babyak, I will never forget the example you set for me almost a decade ago. You taught me to be kind and humble, and you allowed me the intellectual freedom to learn on my own, while never letting me stray too far from the correct path. Dr. Helming (your honor), you taught me to be confident in my work, always reminding me that *I know my research*. Through the example that you set for me at Regeneron, I know exactly what is needed to be a great leader and mentor and I hope to emulate that to lead a team of my own someday.

Finally, I'm thankful for my biggest support system – my family. To my parents, who I owe absolutely everything to, thank you for your continued support and understanding during these past five years. I'm especially thankful to my dad, who, whether he knew it or not, was an analytical chemist at a brewery some 30 years ago – I guess it is hereditary. And to my husband, Jesse, who day-in and day-out dealt with all the negative consequences of being married to a graduate student, thank you for sticking by me through it all.

ABSTRACT

The use of mass spectrometry in complex mixture analysis has had a profound impact on the way researchers approach scientific investigations. Although this versatile analytical tool can provide insight into the chemical components of a sample, mass spectrometric data can often be influenced by oxidation resulting from either the sample itself or chemical transformations that occur during ionization (i.e., biological oxidation and in-source oxidation, respectively). Oxidation can yield complex mass spectra that comprise unexpected ions and, ultimately, prevent the accurate characterization of components in a sample. In some instances, however, oxidation in mass spectrometry may be used advantageously in the analysis of hard-to-detect analytes. In the current work, various studies involving oxidation in mass spectrometry are discussed. Specifically, a fundamental investigation on the in-source oxidation of hydrocarbons was performed to explain the mechanism by which these transformations occur. This study presents a novel mechanism for in-source oxidation, for which few proposed mechanisms exist. An analysis of compounds that are more prone to in-source oxidation (i.e., sulfur-containing metabolites) was performed by mitigating chemical transformations through derivatization, allowing the proper characterization of a metabolic cycle in which readily oxidizable metabolites are essential. The downstream effects of biological oxidation were investigated in malnourished mammals through the use of various metabolite and lipid profiling methods. These investigations promoted the phenotyping of malnourished versus healthy subjects. Finally, novel graphical algorithms were developed and explored to evaluate signs of oxidation in the lipidome. This investigation yielded a promising data visualization technique that can distinguish oxidized lipids, as well as lipid classes. The collection of these studies not only advances the understanding of oxidation in mass spectrometry, but also expands the potential applications for utilizing or mitigating these chemical transformations in complex mixture analysis.

TABLE OF CONTENTS

LIST OF TABLES

LIST OF FIGURES

CHAPTER 1.
INTRODUCTION TO MASS SPECTROMETRY

1.1 Mass spectrometry represents a vital analytical technique

For over a century, mass spectrometry (MS) has served as an essential analytical tool to multiple divisions of science and industry.[1] From the analysis of single elements[2, 3] to the characterization of intact ribosomes[4], this detector has excelled in the analysis of analytes spanning a broad range of chemical properties, exceeding the sensitivity and selectivity of most other analytical instruments.[5] MS has commonly been used by researchers for the purposes of screening, quantitation, profiling, characterization, and structural elucidation of components in complex mixtures. Although several varieties of mass spectrometers exist, and new configurations are being developed consistently, it is common that the instrument possesses two main components: an ionization source and a mass analyzer.

*1.1.1 **Ionization source***

For an analyte to be detected by the mass spectrometer, it must first be either positively or negatively ionized as only charged molecules can be routed through the instrument. The resulting ion is commonly referred to as the mass-to-charge ratio (*m/z*) considering each ion exhibits a specific mass and charge. Many ionization sources possess the ability to generate either positively or negatively charged ions via an electric potential (e.g., an electrode or charged capillary). Often, analytes are infused into the ionization source in a liquid matrix and must be aerosolized and desolvated during the ionization process. Upon ionization, ions are channeled into the mass spectrometer inlet via a pressure difference produced by the interface's high vacuum.

In this work, two common atmospheric pressure ionization (API) sources are utilized: electrospray ionization (ESI) and atmospheric pressure chemical ionization (APCI). Both of these sources are considered "soft" ionization techniques, meaning they often generate intact ions as opposed to "hard" ionization sources that generate highly fragmented ionic products (i.e., electron impact ionization or EI). ESI and APCI represent two commonly used ionization sources in practice, but do not encompass the breadth of available ionization techniques.

1.1.1.1 Electrospray ionization (ESI)

In ESI, volatile, liquid solutions containing the analyte(s) of interest are infused through a charged capillary at a specific flow rate. Once the solution reaches the tip of the capillary, it encounters a positive or negative electric field that begins generating ions in solution. Upon exiting the capillary, the charged solution mixes with the sheath and/or auxiliary gas (often nitrogen). The combination of these events (i.e., liquid flow, charged capillary, and nitrogen flow) generates what is known as the Taylor Cone – a spray with a defined half angle of 49.3° that fosters ionization. The proper formation of the Taylor Cone is dependent on multiple factors (i.e., liquid surface tension, distance to the counter electrode, and vacuum permittivity) and stems from competition between the retracting behavior of the liquid's surface tension and the expanding manner of the electrostatic forces. It is this phenomenon that allows charged droplets to be emitted from the spray.

Although ESI is heavily used in practice, the exact mechanism by which the Taylor Cone emits ions is not strictly known. Two theories have been proposed that explain ESI – the charged residue model (CRM) and the ion evaporation model (IEM). In the CRM, it is believed that the desolvation of a charged droplet promotes the formation of an additional, droplet-specific Taylor Cone that emits smaller charged droplets. This process, theoretically, repeats itself until one ion remains. The alternative model (i.e., IEM), explains charged droplet emission through competition between surface tension and electric field; once the charged droplet becomes small enough, the surface charge density exceeds the Rayleigh limit and expels ions from itself.[6]

ESI is well-known for generating both singly and multiply charged ions, broadening its use from small molecule analysis to large molecule analysis. In its simplest form, ESI generates singly, positively charged molecules (or $[M + H]^+$) where $z = 1$ in the m/z. Analytes may also be generated where $z > 1$, promoting the mass spectrometric analysis of large molecules such as peptides and proteins. This is extremely useful for the characterization of large molecules that exceed the mass range of the instrument. For example, if the mass range of the instrument is 50 – 2,000 Da, a protein weighing 10,000 Da could not be detected without multiple charges as the instrument

detects *m/z*, not molecular weight. For this reason, ESI is regularly used in multiple industries to analyze large biomolecules, but is also essential in small molecule analysis.

1.1.1.2 Atmospheric pressure chemical ionization (APCI)

Contrary to ESI, APCI can ionize analytes in both the liquid and gas phases. For liquid-phase mixtures, the sample is pumped through a capillary contained within a heated chamber that exudes sheath/auxiliary gases (i.e., nitrogen).[3] The combination of high heat and desolvation gas promotes the nebulization of the liquid to the gas-phase. At the same time, a corona discharge (a type of plasma) is produced by a corona discharge needle via a high voltage and is positioned near the outlet of the APCI source. Here, the plasma interacts with highly prevalent atmospheric gases in the ionization environment (i.e., desolvation gas) where it undergoes the following cascade to ionize the ion of interest (M):[3]

$$N_2 + e \rightarrow N_2^{+\bullet} + 2e \quad (1)$$

$$N_2^{+\bullet} + 2N_2 \rightarrow N_4^{+\bullet} + N_2 \quad (2)$$

$$N_4^{+\bullet} + H_2O \rightarrow H_2O^{+\bullet} + 2N_2 \quad (3)$$

$$H_2O^{+\bullet} + H_2O \rightarrow H_3O^+ + HO^\bullet \quad (4)$$

$$H_3O^+ + H_2O + N_2 \rightarrow (H_2O)_2H^+ \quad (5)$$

$$(H_2O)_{n-1}H^+ + H_2O + N_2 \rightarrow (H_2O)_nH^+ \quad (6)$$

$$M + (H_2O)_nH^+ \rightarrow [M + H]^+ + (H_2O)_n \quad (7)$$

In the previous series of equations, the highly prevalent desolvation gas (N_2) initially becomes ionized by the corona discharge, generating highly energetic radical species. Because water is also in high concentrations in the ionization atmosphere, a charge transfer between the radical nitrogen species occurs to generate radical water species. After a recombination reaction, highly acidic water clusters are generated that promote an even-electron charge transfer of the acidic proton to M, which has previously been nebulized into the gas phase.

The analysis of samples already in the gas-phase is less common in practice, but it has been demonstrated that gaseous samples can be introduced to the corona discharge

needle through a route other than the capillary in the APCI source.[7] Using this sample introduction method, it appears that the cascade of ionization described by Equations 1-7 does not always represent the most abundant ion. This phenomenon is discussed in greater detail in **Chapter 2**.

APCI is well-known to produce intact, singly charged analytes in the form of $[M + H]^+$ and $[M - H]^-$ (or $[M - H]^+$ depending on the type of analyte) in high abundance and it is rare that other adducts are formed in notable abundance. This is, in part, due to the primary mechanism of ionization (i.e., proton charge transfer), but also is a product of the distance between the corona discharge and the mass spectrometer inlet. As this distance increases, the most thermodynamically stable products are formed as they have ample time to reach equilibrium.[3] If this distance is reduced, kinetically favored products tend to be the dominant species and the cascade of ionization is altered.

Considering APCI produces singly charged analytes, it is not necessarily useful in the analysis of large molecules as the *m/z* (where $z = 1$) would exceed the mass range of many detectors. The technique of APCI offers its benefits in small molecule analysis, specifically for analytes that can be difficult to detect by ESI due to volatility or low polarity.

*1.1.2 **Mass analyzer***

Subsequent to ionization and ion-routing through the mass spectrometer, the analyte reaches the mass analyzer, whose primary function is to resolve multiple ions based on their *m/*z. Several types of mass analyzers are utilized in practice (not all of which are discussed here), each offering specific benefits. For example, single quadrupole mass analyzers offer low mass resolution (on the order of 1000s) and a maximum mass range of approximately 2000 – 3000 Da. This mass analyzer is quite useful for small molecule quantitation methods, such as contaminant screening, where analytes greatly differ in *m/z*. For more complex applications where analytes may have similar *m/z*, higher resolving mass analyzers (i.e., Orbitraps) are often utilized. With a mass resolving power on the order of 100,000s and a maximum mass range of 2000 –

3000 Da, these analyzers are widely used in complex mixture analysis (i.e., "-omics" applications).

The current work utilizes a combination of the single quadrupole and Orbitrap mass analyzers and is commercially sold as either the Thermo Scientific Q Exactive (max resolution 140,000) or the Thermo Scientific Exploris 120 (max resolution 120,000). In these hybrid configurations, the single quadrupole is used as a mass filter that allows the selection of specific *m/z*. Here, an operator has the option to select specific *m/z* to isolate using the quadrupole or the instrument can be used in data dependent acquisition (DDA) mode, which isolates the most abundant ions in the sample. The primary purpose for isolating/filtering ions is to fragment specific *m/z* and gain insight to an ion's structure. The process of fragmenting ions is commonly referred to as MS^2 while full scans (i.e., no fragmentation) are referred to as MS^1. The instruments used in the current study induce fragmentation via higher-energy collisional dissociation (HCD), which is a subset of collision-induced dissociation (CID).[8] In HCD fragmentation, isolated ions (i.e., precursor ions) are sent to the HCD cell with high kinetic energy and fragmented through multiple collisions with the collision gas (i.e., nitrogen) to produce product ions.

Precursor or product ions are then routed to the Orbitrap mass analyzer. The Orbitrap is a unique configuration that consists of a "spindle-like" electrode capped by two smaller electrodes.[9] Ions enter the Orbitrap orthogonal to the spindle and begin to radially orbit the electrode. The two end-capped electrodes then promote the oscillation of ions axially across the Orbitrap ultimately yielding the frequency of axial oscillation, which is highly specific and correlates to *m/z*. After being digitally detected by the instrument, a coordinate transformation algorithm (i.e., Fourier Transform) is then applied to the frequency data to yield highly resolved *m/z* and its corresponding abundance. The result of this process yields a mass spectrum that can be interpreted by a researcher or data processing program.

*1.1.3 **Optional chromatographic separation***

Although mass spectrometers are able to provide highly resolved *m/z* data in complex mixtures, competitive ionization (i.e., the likelihood that one molecule will be

ionized to a greater extent than another due to differences in concentration or ionization efficiency) poses an issue for the accurate assessment of a sample. For this reason, chromatographic separation is often incorporated prior to detection by mass spectrometry, such that molecules elute at different times. This leads to a reduction in the effects of competitive ionization and higher selectivity and sensitivity.

Most chromatographic techniques incorporate a stationary phase and a mobile phase. The purpose of the stationary phase is to retain analytes (via adsorption) from a complex mixture based on each analyte's chemical properties. To elute the retained components, a mobile phase is passed through the stationary phase; when the chemical properties (e.g., polarity) of each component is matched by the mobile phase, the analyte desorbs from the stationary phase and is eluted. Often, chromatographic techniques are operated using a gradient to increase baseline resolution (i.e., peak separation). Some examples of gradient elution may be increasing mobile phase polarity over time (normal phase), decreasing mobile phase polarity (reversed-phase), or increasing temperature (gas-phase separations).

In the current work, two chromatographic techniques are utilized: liquid chromatography (LC) and gas chromatography (GC). As their names would imply, LC utilizes liquid mobile phases and is ideal for separating components dissolved in a liquid solution, while GC incorporates a gaseous mobile phase and is best suited to separate components in the gas-phase.

1.1.3.1 Liquid chromatography (LC)

Because of its capacity to separate non-volatile or thermally fragile species dissolved in solution, LC is regularly used to separate biological components, such as metabolites or lipids in various "-omics" extractions.[5] However, not all analytes are easy to analyze chromatographically, which has sparked the development of many variations of this separation technique. Analytes may be separated using columns packed with polar or non-polar stationary phase to operate in normal phase or reversed-phase, respectively. A large variety of stationary phases (e.g., polar, non-polar, size-based, etc.) are available as some stationary phase derivatives are more amenable in retaining specific classes of

compounds. For example, lipids (which possess both a hydrophobic and hydrophilic component) can be separated by their hydrophilic headgroup using a polar stationary phase and a mobile phase gradient that increases in polarity. Contrarily, lipids may also be chromatographically resolved by their hydrophobic tails using a non-polar stationary phase combined with a mobile phase gradient that decreases in polarity. The method by which the components are separated can be tailored to the analytical question being addressed.

The evolution of LC from separations using 500 – 5,000 mm glass columns with particle pore sizes on the order of 100s of μm to its current state has allowed LC to become a staple in most analytical laboratories.[5] Now, LC systems are capable of performing separations on 50 – 250 mm steel-encapsulated columns with pore sizes often measuring 1 – 10 μm. These advances have decreased separation time from several hours to minutes, depending on the complexity of the sample and/or the analytical question. With decreasing column pore size, however, comes an increase in pressure. Thus, one of the most important improvements in LC is the incorporation of a mobile phase pump that can consistently supply selective flow rates and withstand high pressures (up to 15,000 psi).

The combination of separation by LC and detection by MS was a monumental achievement in analytical chemistry. It was not until the development of the ESI source in the 1980s that liquid eluent from an LC was able to be coupled to MS.[10] Since then, LCMS has been used to separate and detect large and small biologically relevant compounds in complex matrices with high sensitivity and selectivity.

1.1.3.2 Gas chromatography (GC)

GC plays a particularly useful role in the analysis of low molecular weight compounds that exhibit low boiling points (or can be derivatized to a compound with a lower boiling point) and/or low polarity. Because GC separates gaseous samples, the length of GC columns (on the order of 10s of meters) is substantially longer than that of LC columns, so that the gas-phase analytes have a greater surface area of stationary phase to interact with. Similar to LC, multiple variations of stationary phases exist, but most are

composed of an immobilized liquid phase of polydimethyl siloxane derivatives that differ in polarity, making each column more amenable to separating different classes of compounds.[5]

Unlike LC, the GC's mobile phase (i.e., often an inert gas such as helium) is not wholly responsible for eluting compounds from the column. Instead, the column is encased in a temperature regulated oven that can follow defined temperature programs. Under this methodology, compounds are eluted from the column based on their boiling points after being retained based on their polarity.

Although GC can only separate components in the gas-phase, liquid samples containing semi-volatile analytes may also be analyzed with the instrument's high temperature injection port(s). Here, an aliquot of a liquid sample is injected into the injection port, the sample is then flash vaporized, and the gaseous vapor is then routed to the column for separation. Analysis of volatiles may be conducted using headspace GC, which allows an aliquot of analytes dissolved in a gas to be injected onto the column. Similarly, solid phase microextraction allows volatile compounds to adsorb to a fiber tip and subsequently be desorbed in the injection port and onto the column.

GC was initially coupled to MS in the 1950s, long before the inception of LCMS.[11] Because MS requires analytes to be in the gas phase for proper ionization, GC was the ideal instrument for coupling. It is common practice that GCMS systems utilize ionization sources under vacuum, but some instances of GC coupled to API techniques have been reported (refer to **Chapter 2** for a more thorough discussion). In fact, the National Institute of Standards and Technology (NIST) used GCMS with EI ionization to generate a database of over 240,000 standards that is still heavily used for compound identification.[12]

1.2 Types of oxidation affecting mass spectrometry

Oxidation is defined as the loss of electrons from a reactant and was termed as such because reactions with oxygen generally produce this end result.[13] Some of the most notable oxidation reactions are combustion reactions (Equation 8) and the oxidation of glucose to produce energy in biological systems via cellular respiration (Equation 9).

$$CH_4 + 2O_2 \rightarrow CO_2 + 2H_2O + \textit{heat} \quad (8)$$

$$C_6H_{12}O_6 + 6O_2 \rightarrow 6CO_2 + 6H_2O + \textit{energy} \quad (9)$$

In the above cases, oxidation is viewed positively as a chemical transformation due to its necessity to life. However, many oxidation reactions stem from undesirable reactions with oxygen that are influenced by environmental factors (i.e., time, temperature, humidity, etc.). A prevalent example of an unfavorable oxidation reaction is the corrosion or rusting of iron (Equation 10).[14]

$$2Fe + \left(\frac{3}{2}\right)O_2 + H_2O \rightarrow Fe_2O_3 \cdot H_2O \quad (10)$$

MS is also affected by desirable and undesirable oxidation reactions that occur either in-source or in the sample prior to analysis. Occasionally, these oxidation reactions can be used for structural elucidation of molecules or can provide insight to the state of a biological system. However, the main disadvantage of oxidation in MS is the complexity of the resulting mass spectra and the potential to incorrectly characterize a sample due to unexpected oxidation products. In the current work, two types of oxidation in MS are investigated: in-source oxidation and biological oxidation.

*1.2.1 **In-source oxidation***

API techniques offer versatility and accessibility over ionization techniques that require high vacuum; however, these techniques are susceptible to in-source oxidation. Importantly, the mechanisms by which in-source oxidation occurs are largely undefined for most ionization sources, making the oxidized products more difficult to predict. In some instances, however, in-source oxidation has been thoroughly investigated and can be used advantageously to characterize complex mixtures.[7, 15] Specifically, these chemical transformations increase the signal-to-noise ratio of analytes that are difficult to ionize, as well as aid in structural elucidation.[7, 15] A more through discussion of this is presented in **Chapter 2**.

Occasionally, the mitigation of in-source oxidation may be preferred. A suitable example of this is represented by the analysis of sulfur-containing metabolites, which are more prone to in-source oxidation than other substituents. In the event an experiment

requires the quantitation of sulfur metabolites, it would be necessary to control in-source oxidation by protecting (i.e., through derivatization) the sulfur moieties prior to analysis. An application of mitigating in-source oxidation is discussed in **Chapter 3**.

In-source oxidation is suspected to be induced by reactive oxygen species (ROS) at the site of ionization for API techniques that utilize high voltages. This phenomenon was observed in pharmaceutical products using desorption electrospray ionization (DESI) with increasing voltage.[16] ROS species have also been suspected to influence in-source oxidation using plasma-based ionization techniques.[7, 15, 17] Ionization parameters may be tuned to decrease in-source oxidation, but it is unlikely to be corrected completely.

*1.2.2 **Biological oxidation***

Though in-source oxidation illustrates a complex problem in MS, some oxidation products may be consequential of the sample itself. This occurrence is well-demonstrated by biological systems undergoing oxidative stress stemming from increased ROS. These species are commonly generated in biological systems as a result of normal biological processes; however, there exists a delicate balance between ROS production and neutralization (via antioxidants) that, if perturbed, can have detrimental consequences on the system.[18]

Unregulated ROS affect numerous biological pathways, where downstream effects can be observed at the simplest level of the biological system (i.e., through the phenotype or metabolome).[18] Instances of these downstream effects have been observed in malnourished mammalian subjects[19] and are further discussed in **Chapter 4**. The end-products of ROS perturbations may not be fully characterized and likely result in oxidized metabolic products, similar to what would be observed in in-source oxidation. For example, lipid peroxidation (i.e., the oxidation of lipid species) has been known to occur under conditions of oxidative stress, leading to lipid species that may be inadvertently ignored or misannotated.[20] To better understand the impact of oxidative stress due to ROS perturbations, it is necessary to incorporate sophisticated data processing and/or data visualization algorithms. An application of novel graphical methods to evaluate biological oxidation is detailed in **Chapter 5**.

1.3 Case studies of oxidation in mass spectrometry

This dissertation research expounds upon various case studies focused on in-source oxidation and biological oxidation in mass spectrometry. Here, a fundamental study on in-source oxidation is conducted to elucidate oxidation mechanisms of a major components of petrochemical mixtures (**Chapter 2**). In a separate study, which focuses on probing a specific cellular communication pathway in various bacterial species, in-source oxidation was mitigated by protecting easily oxidizable moieties through the process of derivatization (**Chapter 3**). Phenotypical differences resulting from biological oxidation in emaciated mammals (specifically, equine) were investigated and led to the metabolic understanding of malnutrition in horses (**Chapter 4**). In the final study, potential differences resulting from biological oxidation in the lipidome of emaciated equine were explored through the use of a novel graphical method that promotes the investigation of highly complex lipidomics data and the distinction of oxidized lipids resulting from lipid peroxidation (**Chapter 5**). The culmination of these studies represents one of the first studies focused on a broader understanding of how oxidation affects mass spectrometry either during ionization or prior to ionization.

CHAPTER 2.

A FUNDAMENTAL STUDY ON IN-SOURCE OXIDATION

Discovery of Combustion-like In-source Oxidation of Linear Saturated Hydrocarbons Using GC-APCI-HRMS

Data presented in this chapter has been adapted from the following published journal article:

Brown, L.P., Seaton, W.B., Powers, J.B., Campagna, S.R. "Discovery of Combustion-like In-source Oxidation of Linear Saturated Hydrocarbons using GC-APCI-HRMS." *Journal of Mass Spectrometry.* **2024,** 59(10): 1 – 8

2.2 Abstract

APCI is often used in the analysis of linear saturated hydrocarbons (LSHs) as this ionization technique commonly produces $[M - H]^+$ ions in high abundance. However, APCI (along with other atmospheric pressure sources) is often impacted by in-source oxidation, leading to a variety of ionic products. Identifying these products and understanding their mechanisms of formation is crucial for characterizing complex mixtures with substantial hydrocarbon content, such as those found in the petrochemical industry. In this study, in-source oxidation of LSHs was observed in GC coupled to high resolution mass spectrometry (HRMS) via a custom-built APCI interface. Studies showed that the abundance of these oxidized ions correlated positively with atmospheric water, yet occurred without the inclusion of water-based oxygen as judged by experiments with stable isotope labeled water. The oxidation of LSHs was further influenced by the reactive species in the ionization atmosphere. Fragmentation data using stable isotope labeled LSH standards unveiled multiple structurally unique ions with one or more oxidation sites on both primary and secondary carbons. These ionic products bear resemblance to combustion byproducts, suggesting the instrumental configuration fosters plasma-assisted combustion-like processes that encourage the radical-mediated oxidation of LSHs rather than generate $[M - H]^+$. Through these investigative efforts, a mechanism analogous to combustion was proposed for the formation of LSH oxidation products in GC-APCI-HRMS. Data demonstrate that these ions are robustly generated in petrochemical products, allowing for proper characterization of these complex mixtures.

2.3 Introduction

GCMS has long been a critical analytical tool in a diverse array of scientific fields and is particularly important in petrochemical analysis.[11, 21-25] Traditional GCMS setups

generally rely on EI or chemical ionization (CI); these instruments offer reliable data, but lack exact mass measurements and require dedicated systems due to the need for ionization at low-pressure. In response to the desire for high resolution GCMS measurements without the constraints of dedicated instrumentation, Powers and Campagna designed an APCI interface that coupled GC to high resolution mass spectrometry (HRMS), outperforming GCMS setups that used other sources (including EI).[7] APCI was chosen for this configuration as it is more desirable over other API techniques (e.g., electrospray ionization) for the analysis of low-polarity compounds with low boiling points, which are typical characteristics of compounds analyzed by GC as well as many petrochemical components.[2, 3, 26]

One of the common classes of analytes analyzed by APCI is that of saturated hydrocarbons, as these non-polar compounds typically produce intact ions (in the form of $[M - H]^+$ in positive mode) in high abundance.[7, 27, 28] Because hydrocarbons make up a significant portion of fuel content and their purity impacts combustion performance characteristics as well as fuel stability, accurate characterization of these analytes in petrochemical mixtures is essential.[23, 29, 30]

During the evaluation of linear saturated hydrocarbons (LSHs) using the GC-APCI-HRMS configuration for potential petrochemical application, it was found that, along with the expected $[M - H]^+$ ion, oxidized species were also generated (**Figure 2.1** and **Appendix Table 2.1**) and were indicative of in-source oxidation.[7] Interestingly, in-source oxidation products similar to those observed using GC-APCI-HRMS have commonly been reported using atmospheric pressure, plasma-based ionization sources for the reason that these techniques operate under exposure to atmospheric air and moisture.[15, 17, 31-36] To utilize the configuration of GC-APCI-HRMS for the accurate

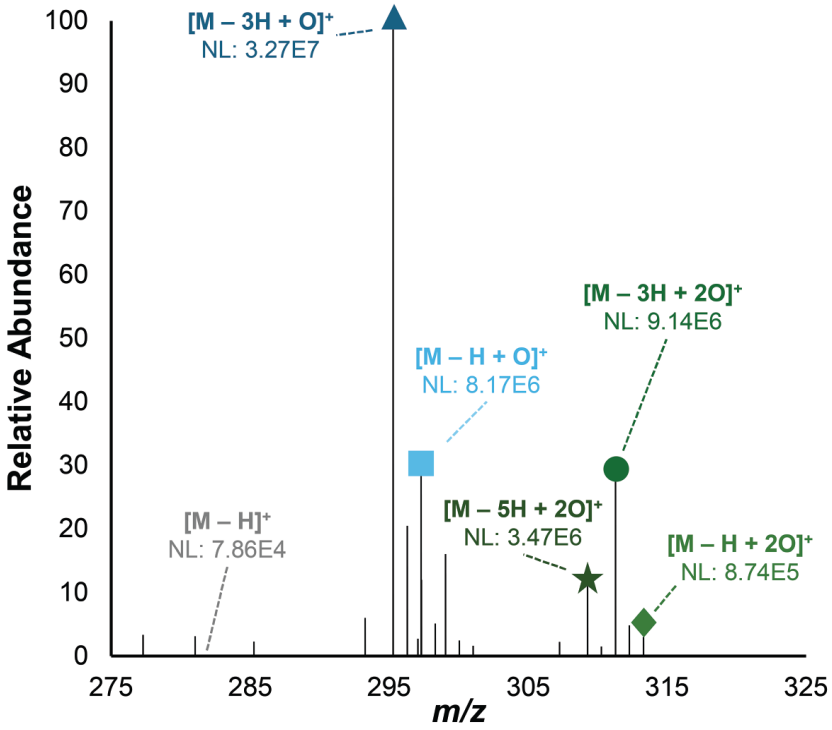

Figure 2.1. MS[1] analysis of eicosane ($C_{20}H_{42}$; used as a representative example of LSHs) using GC-APCI-HRMS.

characterization of petrochemical products, it is crucial to elucidate the structure of these LSH-derived in-source oxidation products and to understand the mechanisms and extent of their formation.

Herein, various experimental approaches were employed to evaluate the effect of the ionization atmosphere on in-source oxidation, determine elemental contributions from atmospheric compounds, and structurally elucidate the observed oxidation products to provide insight to potential mechanisms that influence their formation. These studies suggest a mechanism for combustion-like in-source oxidation that occurs consistently in complex, petrochemical mixtures.

2.4 Results and discussion

2.4.1 ***Oxidation products are influenced by changes in the ionization atmosphere***

Eicosane ($C_{20}H_{42}$; M = 282.3287 Da), a long-chain LSH, was chosen as the representative compound for mechanistic investigations as it produced both the expected $[M - H]^+$ ion as well as the in-source oxidation products in high abundance. To explore what factors might influence in-source oxidation, $C_{20}H_{42}$ was analyzed under various corona discharge currents, aqueous conditions, and reagent gas conditions and the resulting changes in LSH-derived oxidation products were evaluated (**Appendix Figure 2.6**).

High ionization voltage has been linked to increased oxidation levels using other API techniques (i.e., desorption electrospray ionization or DESI).[16, 33] Therefore, it was important to determine potential effects of variable corona discharge current (which correlates with voltage) on levels of oxidation in GC-APCI-HRMS by reducing the discharge current from the baseline level of 10 μA sequentially to 2.5 μA. Upon normalization, a direct correlation between discharge current and in-source oxidation was observed as the percent change in LSH oxidation products diminished with decreasing corona discharge current (**Figure 2.2** and **Appendix Figure 2.6**). Thus, byproducts are likely derived from a high energy process that involves reactive species in the ionization atmosphere similar to those observed with DESI.[16, 33]

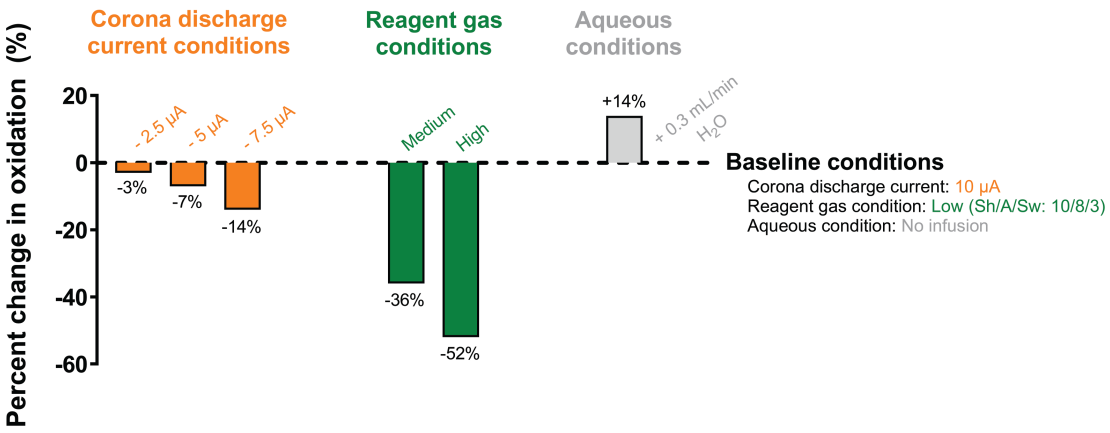

Figure 2.2. Evaluation of eicosane ($C_{20}H_{42}$) oxidation products using GC-APCI-HRMS under variable corona discharge current, reagent gas level (nitrogen; where medium and high are represented by Sh/A/Sw of 20/16/3 and 30/24/3, respectively), and atmospheric water concentration.

To build on the observation that reactive species may influence in-source oxidation, $C_{20}H_{42}$ was analyzed under various levels of reagent gas (i.e., nitrogen) by altering the sheath (Sh) and auxiliary (A) gases. It was speculated that increasing the concentration of nitrogen in the ionization atmosphere would displace molecular oxygen and its reactive byproducts, altering the profile of reactive ions and subsequent oxidation products. Increasing reagent gas content beyond baseline levels (Sh/A/Sw: 10/8/3) resulted in a substantial decrease in oxidation (**Figure 2.2**), likely caused by a shift in the most exergonic ionization mechanism. With higher reagent gas levels, the ionization atmosphere becomes saturated with highly energetic nitrogenous radical cations ($[N_2]^{+\cdot}$ or $[N_4]^{+\cdot}$); this primarily results in a radical cation-mediated mechanism for LSHs, leading to highly fragmented, low mass cations (such as $[C_4H_9]^+$, $[C_5H_{11}]^+$, $[C_6H_{13}]^+$, etc.) that resemble products of EI (**Appendix Figure 2.7**).[2, 3] From this, it is clear that increased concentrations of reactive nitrogen species were not responsible for the generation of LSH ions that were further oxidized.

In fact, the inverse relationship between oxidation and nitrogen content aligns with the hypothesis that dilution of atmospheric oxygen or oxygen-containing gaseous compounds (i.e., $OH^{\cdot}$, molecular oxygen or O_2, ozone or O_3, etc.) results in lower levels of oxidation products and further suggests the role of these compounds as the source of oxidation.[2, 3, 37, 38] Additionally, as the concentration of reagent gas increases, there is a decreased probability that the GC carrier gas (i.e., helium) becomes ionized due to the difference in ionization potential. This prevents subsequent charge transfers from helium, which has shown to both directly and indirectly impact the ionic products formed.[2, 15, 32, 34, 39, 40] Taken together, it is conceivable that helium and/or oxygenated gaseous compounds influence the formation of the oxidized products observed in GC-APCI-HRMS.

To investigate the involvement of the most prevalent oxygen-containing atmospheric compound (i.e., H_2O) in the oxidation mechanism, 0.3 mL/min of H_2O was infused into the ionization atmosphere during the analysis of $C_{20}H_{42}$, resulting in a 14%

increase in oxidation (**Figure 2.2**). Overall ionization also doubled (**Appendix Figure 2.6**) as the addition of H_2O promotes the generation of more highly acidic water clusters (i.e., $(H_2O)_nH^+$) that are responsible for soft ionization via proton transfer. The notable increase in oxidized products could implicate water as the source of oxygen and/or protons via interactions with acidic water clusters that could influence oxidation of LSHs.

*2.4.2 **LSH oxidation products do not incorporate oxygen from atmospheric water***

Although water was found to positively impact in-source oxidation, studies in similar API setups suggest that these oxidation reactions are not driven by atmospheric water.[17, 36, 41] To gain more mechanistic insight into the impact of water on GC-APCI-HRMS ionization, separate infusion experiments were performed with stable isotope labeled water in the form of deuterium oxide and heavy oxygen labeled water (i.e., D_2O and $H_2{}^{18}O$, respectively). These investigations were expected to provide conclusive evidence to potential donation of hydrogen (in the form of deuterium) or oxygen (in the form of ^{18}O) from atmospheric water.

The infusion of D_2O led to a mixture of hydrogen- and deuterium-protonated ions (**Figure 2.3** and **Appendix Table 2.2**), indicating that some oxidized molecules are protonated by acidic $(H_2O)_nH^+$ (or $(D_2O)_nD^+$ in this case), yet other ions are not. For example, $C_{20}H_{42}$ in the presence of additional H_2O yielded *m/z* 311.2941 ($[M - 3H + 2O]^+$), yet with additional D_2O, *m/z* 312.3006 ($[M - 4H + D + 2O]^+$) was highly prevalent while *m/z* 311.2941 was no longer observed. This difference, representing the exact mass shift between a hydrogen- and deuterium-protonated ion (Δm = 1.0065 Da), strongly suggests that *m/z* 311.2941 incurs ionization via atmospheric $(H_2O)_nH^+$ via proton transfer and that *m/z* 312.3006 arises from deuteron transfer from $(D_2O)_nD^+$. In contrast, *m/z* 309.2785 ($[M - 5H + 2O]^+$) did not show a mass shift due to the infusion of H_2O instead of D_2O. Because this ion does not utilize a proton from the atmosphere for ionization, it was concluded that the oxygen must carry the charge in the form of an oxonium ion or radical cation. The results obtained for $C_{20}H_{42}$ with D_2O infusion were

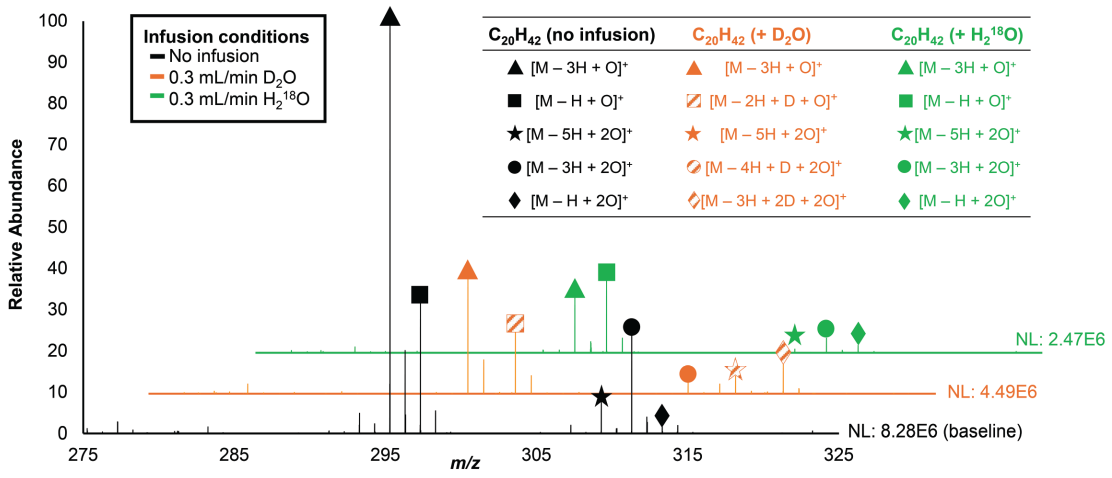

Figure 2.3. Analysis of eicosane ($C_{20}H_{42}$; M = 282.3287 Da) with infusion of water and heavy water (no infusion represented by the black trace, D_2O represented by the orange trace, and $H_2{}^{18}O$ represented by the green trace). Striped symbols represent deuterium incorporation. No mass shifts representative of ^{18}O incorporation were observed.

corroborated by analyzing $C_{20}D_{42}$ with H_2O (**Appendix Table 2.2**), providing additional evidence for the protonation via aqueous sources of only some oxidation products. Importantly, the results captured here align with a study using a similar instrumental configuration (i.e., GC coupled to HRMS via dielectric barrier discharge ionization) in which nine of the thirteen oxidation products observed for hexadecane ($C_{16}H_{34}$) under humidification with D_2O were influenced by aqueous content in the atmosphere.[34]

In the investigation to evaluate potential contributions of atmospheric oxygen to in-source oxidation (via infusion of $H_2{}^{18}O$), it was found that incorporation of ^{18}O was not observed in any of the oxidation products (**Figure 2.3**). This finding, along with variable reagent gas experiments, further suggests the incorporation of oxygen is from sources other than atmospheric water, which aligns with previous findings that in-source oxidation of hydrocarbons in other APCI setups were not induced by water.[17, 36, 41]

*2.4.3 **Fragmentation data reveals oxidation products with one or more oxidation sites on both primary and secondary carbons***

Fragmentation data via MS^2 were collected for each oxidized $C_{20}D_{42}$ (M = 324.5923) ion of interest with proton contributions from atmospheric H_2O (via infusion of H_2O). To annotate these spectra, the following characteristics were evaluated: common neutral losses (e.g., D_2O, HOD, C_xD_y, carbon monoxide, etc.) from the isolated precursor ions, double bond equivalencies (DBEs), predicted chemical formulae of the fragments, and the lowest *m/z* fragment containing oxygen(s) traced from the precursor ion. Combined, these evaluations allowed the structural elucidation of the ions of interest as a myriad of ions with oxidation sites on both primary and secondary carbons. Specifically, the following ions were annotated: $[M - 3D + O]^+$ as acylium ions, $[M - 2D + H + O]^+$ as various isomers of dialkyl ketones, $[M - 5D + 2O]^+$ as ketone oxonium ions, $[M - 4D + H + 2O]^+$ as various isomers of diketones, and $[M - 3D + 2H + 2O]^+$ as carboxylic acids (**Figure 2.4**). An explanation of the MS^2 spectral annotation is illustrated in **Appendix Figure 2.9.**

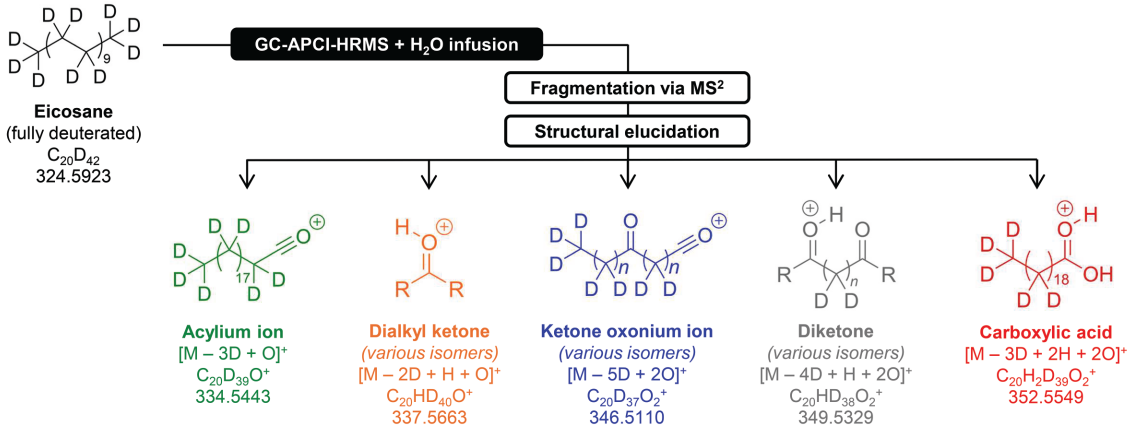

Figure 2.4. Annotation of oxidized ions of interest from fragmentation data under low collisional energies (i.e., stepped energies of 10, 30, and 50 eV). Annotated ion names, change in structure from the parent molecule (i.e., $C_{20}D_{42}$), chemical formula based on exact mass (within 5 ppm error), and observed *m/z* are listed for each ion (except for $C_{20}D_{42}$ for which the neutral mass is listed). Detailed fragmentation spectra and a thorough explanation of the assignment of these ions can be found in Supplementary Figures S4 and S5 – S9.

2.5.1 ***In-source oxidation in GC-APCI-HRMS does not align with reported heterolytic mechanisms***

Due to the presence of oxygen, API techniques are susceptible to in-source oxidation, sometimes resulting in products similar to those observed in the GC-APCI-HRMS configuration discussed here.[15, 17, 31-36] A notable example of this is illustrated by in-source oxidation of LSHs in atmospheric pressure gas chromatography (APGC).[17] However, one crucial difference between the APGC and GC-APCI-HRMS configurations is the detection of LSH-nitrogen adducts in APGC. Importantly, nitrogen adducts were not observed in GC-APCI-HRMS, suggesting a fundamental difference in ionization mechanism between these setups. Further, the proposed mechanism for in-source oxidation in APGC implicated O_3 as being the oxidant responsible for the observed products.[17] Upon evaluation of whether the products in GC-APCI-HRMS could be generated via this heterolytic mechanism, it was found that elucidated in-source oxidation products (specifically, ions with two sites of oxidation) could not be formed.

Similarly, O_3 was also proposed as the oxidant responsible for oxidation products observed in soft plasma ionization by glow discharge, where successive, heterolytic oxidation reactions subsequent to the generation of $[M - H]^+$ were postulated to occur.[36] If the in-source oxidation observed in GC-APCI-HRMS required the generation of $[M - H]^+$, oxidation via H_2O would be prominent as this abundant nucleophile would, in addition to O_3, react with the $[M - H]^+$ substrate. Considering the absence of water-based oxygen incorporation, the in-source oxidation mechanism in GC-APCI-HRMS does not proceed via $[M - H]^+$.

Because reported heterolytic mechanisms do not align with observations in GC-APCI-HRMS, it was postulated that a potentially unique in-source oxidation mechanism that is more energetically favorable than generating $[M - H]^+$ and is most likely radical-mediated. An important distinction between GC-APCI-HRMS and others[17, 36] that argue heterolytic dissociation is the use of helium as the GC carrier gas. Because it exhibits the highest ionization potential among the noble gases, helium impacts the reactive species in the ionization atmosphere, notably forming various radical species.[2, 15, 32, 34, 39, 40, 42] In

plasma, helium facilitates the generation of atomic oxygen ($O^{\cdot}$) from O_2 in the atmosphere and, similar to reactions with argon, may initiate a cascade of recombination reactions to produce a variety of potential oxidants, such as atmospheric oxygen-based $OH^{\cdot}$.[43] Additionally, $OH^{\cdot}$ (and additional O_2) can be generated by the homolytic decomposition of O_3.[44] Therefore, plasma-based ionization, especially when helium represents a primary atmospheric component, provides a complex ionization atmosphere that is saturated with highly energetic, O_2-based radical species that plausibly influence ionization mechanisms.

*2.5.2 **GC-APCI-HRMS fosters ideal conditions for plasma-assisted combustion-like ionization mechanisms***

Plasmas like corona discharge can undergo plasma-assisted combustion, which is utilized in the fuel industry to thermally and kinetically enhance the efficiency of the combustion process.[40] In fact, one of the most recognized sources of LSH oxidation is the combustion reaction of hydrocarbons with molecular oxygen, which, despite its apparent simplicity, is an intricate process likely entailing thousands of pathways that yield a wide array of products.[45, 46] Recently, neural network-based molecular dynamics simulations were employed to explore potential outcomes of the combustion process.[46] These simulations unveiled a web of radical-initiated reactions wherein hydrocarbons (i.e., methane) react with O_2, $OH^{\cdot}$, or $H^{\cdot}$ to yield a collection of intermediates and products, including formaldehyde and formic acid, which mirror the dialkyl ketone and carboxylic acid products detected in GC-APCI-HRMS. Computations suggest that the formation of these products in short-chain LSH (e.g., butane) combustion reactions arise from exergonic processes with relatively low activation barriers, easily surmountable with the energy supplied by a corona discharge.[45, 47] Along with being energetically feasible, the generation of radical species via combustion reactions is proposed to occur on the order of picoseconds (or shorter) – much faster than proton-transfer reactions.[43, 46, 48]

Taken together, a mechanism akin to plasma-assisted combustion represents a compelling explanation for the in-source transformations observed in GC-APCI-HRMS. Not only do the ionic products observed resemble byproducts of combustion (i.e., dialkyl

ketones and carboxylic acids), but the availability of molecular oxygen-based radical species to induce combustion-like reactions aligns with the observation that water-based oxygen is not involved in the in-source oxidation mechanism. The correlation between corona discharge current and in-source oxidation was also explained through this mechanism in that more highly energetic radical species (i.e., homolytic decomposition and/or recombination products) generated by a higher corona discharge current induce more radical-mediated combustion-like reactions that result in more oxidation products. Though plasma is a distinct environment that has not been thoroughly computationally explored, simulations from both gas and liquid phase models indicate that a radical-based oxidation mechanism of hydrocarbons is more energetically favorable than heterolytic mechanisms.[44, 49] This explains the low abundance of the $[M - H]^+$ ion, along with the fact that these radical-reactions occur at a faster rate. Overall, it is conceivable that the conditions of the GC-APCI-HRMS setup (specifically, the combination of plasma-based ionization and helium under atmospheric conditions) promote combustion-like ionization over the generation of $[M - H]^+$ for LSHs due to faster reaction rates and/or more energetically favorable processes.

A preliminary attempt to unravel the complex network of mechanisms leading to the observed ions is presented in **Appendix Figure 2.10**. It is imperative to note, however, that a definitive mechanism cannot be established without reaction rate studies and/or computational modeling, the latter of which is still in its infancy for plasma-based systems.[50, 51] The proposed mechanism represents a possible route of in-source oxidation in GC-APCI-HRMS, as supported by the data in this study.

*2.5.3 **Understanding combustion-like in-source oxidation in GC-APCI-HRMS is important for accurate characterization of complex petrochemical mixtures***

To evaluate GC-APCI-HRMS on complex mixture analysis, two petrochemical fuels were analyzed: unleaded gasoline (primarily composed of $C_4 - C_{12}$ LSHs) and diesel fuel (primarily composed of $C_8 - C_{25}$ LSHs).[52] The results from these analyses (**Figure 2.5**) aligned with expectations based on LSH content and fuel composition in

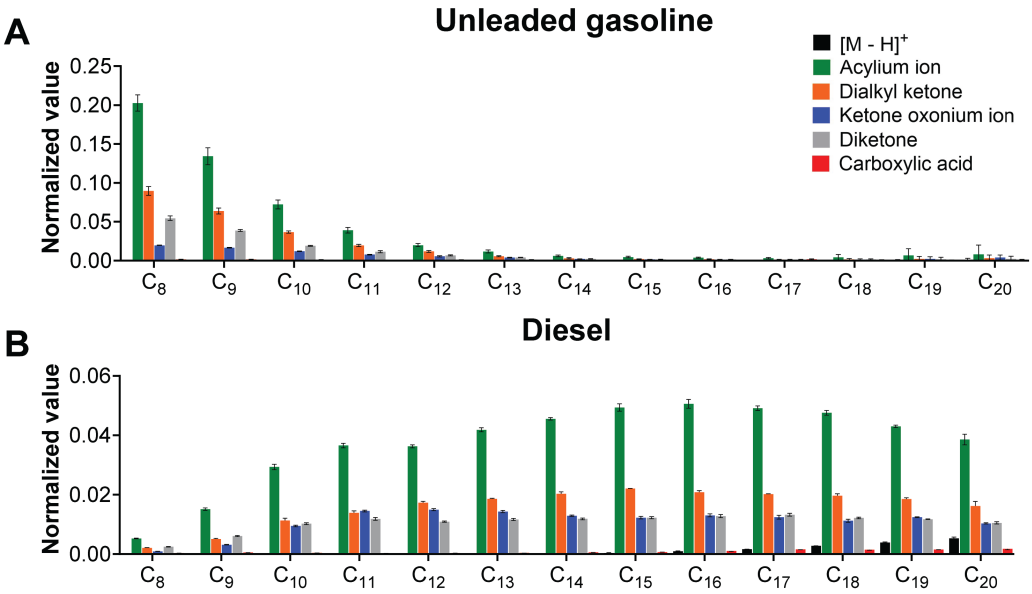

Figure 2.5. Analysis of the C_8 – C_{20} LSH content in A) unleaded gasoline and B) diesel fuel using GC-APCI-HRMS as identified by combustion-like in-source oxidation. All oxidized ions of interest and $[M - H]^+$ generation were evaluated and normalized by the sum of all ions detected per sample.

that shorter chain LSHs were primarily detected in unleaded gasoline while longer chain LSHs were detected in diesel fuel. The relative abundance of each identified in-source oxidation product in the complex mixtures were consistent with those measured from pure standards. Specifically, the acylium ion, dialkyl ketone, and diketones represented the three most abundant ions of interest despite the fact that these petrochemical products are composed of various isomeric compounds, including both linear and non-linear hydrocarbons.

Similar to the observations from pure standards, the formation of $[M - H]^+$ was not favored during the analysis of petrochemical products by GC-APCI-HRMS, further supporting the combustion-like mechanism in complex mixtures. Given that this instrumental configuration consistently produces in-source oxidation products whose identities and percent abundances can be accurately predicted through combustion-like mechanisms, it was concluded that GC-APCI-HRMS serves as a suitable configuration in the analysis of complex petrochemical mixtures.

2.6 Conclusions

In this study, a unique in-source oxidation mechanism of LSHs by GC-APCI-HRMS was discovered. The formation of multiple LSH-derived oxidation products was altered with changes in ionization atmosphere, specifically under conditions that varied reactive ions available for ionization. Oxidation was notably enhanced with the infusion of additional water; however, the utilization of stable-isotope labeled water revealed that only acidic protons from water clusters were used in the ionization mechanism, while water-based oxygen remained unincorporated in the observed products. Fragmentation spectra offered structural insight for each unique ion observed, alluding to the formation of a diverse set of products with oxidation sites on both primary and secondary carbons that resembled byproducts of combustion. From these studies, it was demonstrated that GC-APCI-HRMS can provide appropriate conditions for plasma-assisted combustion-like ionization to occur.[15, 16, 31, 32, 34] Additionally, it was shown that the percentage of in-source oxidation products was predictable, allowing for the accurate characterization of complex petrochemical mixtures despite lacking a prominent $[M - H]^+$ ion. In

conclusion, this study highlights the influence that atmospheric conditions and instrumental setups have on the fundamental properties of plasma-based ionization. These findings also refute the assumption that this ionization technique only proceeds via heterolytic mechanisms and add to the manifold of potential reactions that could occur in plasma-based ionization sources. Future work will consist of determining limits of detection and quantitation, dynamic range, and linearity of these oxidized ions, as well as determining combustion-like mechanisms as they relate to non-linear hydrocarbons.

2.7 Experimental section

2.7.1 ***Reagents and materials***

Deuterated eicosane (fully deuterated; chemical formula $C_{20}D_{42}$) was obtained from Cambridge Isotope Laboratories, Inc. (Tewksbury, MA). Naturally occurring eicosane (non-deuterated; chemical formula $C_{20}H_{42}$) and an alkane standard solution (C_8 – C_{20}) were obtained from Sigma Aldrich (St. Louis, MO). Standards were diluted in HPLC-grade hexanes (Fisher Scientific, Hampton, NH). Ultrahigh purity grade helium (GC carrier gas) was purchased from Airgas (Madison, WI) and nitrogen (APCI reagent gas and HRMS collision gas) was obtained in-house. Unleaded gasoline and diesel fuel were obtained from a local filling station.

2.7.2 ***GC-APCI-HRMS settings and data analysis***

A Thermo Scientific Trace 1300 GC and a Q Exactive™ Plus MS (Thermo Scientific, Waltham, MA) were used for all GC-MS analyses. A custom APCI interface was used to couple the instruments and generate ions.[7] Control of the instrument was performed using the Xcalibur software suite, Version 4.0.27.19. LSHs were separated and detected using modified methods previously described.[7] Briefly, a TG1-MS column (30 m x 0.25 mm i.d. x 0.25 µm df) purchased from Thermo Fisher Scientific (Thermo Scientific, Waltham, MA) and helium (1.4 mL/min) were used to separate analytes. Using a programmable temperature vaporizer (PTV) in CT split mode (330°C, 5:1 split), 2 µL injections of standards were volatilized. Analytes were separated on the column with the following temperature program: initial temperature of 55°C held for 5 min; ramp of 15.0°C/min to 280°C; and final temperature of 280°C held for 5 additional min. The

transfer line from the GC to the MS was kept constant at 300°C. Settings for the APCI source were as follows: sheath gas flow rate set to 10 arbitrary units, auxiliary gas flow rate to 8, sweep gas flow rate to 3, discharge current set to 10.00 µA, ion transfer capillary temperature to 350°C, S-lens RF to 50.0, and vaporizer temperature to 320°C. MS^1 scans (full scans) were acquired in positive mode using a resolution of 140,000, AGC target of 3e6, maximum IT of 50 ms, and scan range of m/z 50 – 750. For MS^2 analyses via parallel reaction monitoring with higher-energy collisional dissociation, data was also acquired in positive mode using a resolution of 17,500, AGC target of 2e5, maximum IT of 50 ms, isolation window of 1.0 m/z, stepped collisional energies of 10, 30, 50 and default charge state of 1. Analyte ions detected in full scan analyses and exact masses from theoretical structures (ChemDraw Version 16.0.1.4; Perkin-Elmer, Waltham, MA) were used to create inclusion lists. All structural figures were created using ChemDraw Version 16.0.1.4 and all feature-based data analysis was performed via FreeStyle™ Version 1.8 SP2 (Thermo Scientific, Waltham, MA) using a 5 ppm error window.

*2.7.3 **Variable atmosphere ionization studies***

To investigate effects of variations in ionization environment, experiments were performed that altered the following parameters: 1) corona discharge current, 2) aqueous concentration in the ionization atmosphere, and 3) levels of reagent gas (i.e., nitrogen). Discharge current and reagent gas levels were changed in the tune method parameters in the Xcalibur software (Thermo Scientific, Waltham, MA). Aqueous conditions were able to be altered due to the unique setup of the custom-built APCI interface, where solvents can be infused and vaporized before interacting with the gas eluent from the transfer line. Multiple infusion experiments were performed using the following: 1) 0.3 mL/min of water (HPLC grade; Fisher Scientific (Hampton, NH)), 2) 0.3 mL/min deuterium oxide or D_2O (99.9%; Cambridge Isotope Laboratories, Inc. (Tewksbury, MA)), and 3) 0.3 mL/min oxygen-labeled water or $H_2{}^{18}O$ (97%; Cambridge Isotope Laboratories, Inc. (Tewksbury, MA)). Visuals were generated in GraphPad Prism version 10.1.0 (La Jolla, CA).

2.7.4 ***Fuel analysis***

Unleaded gasoline and diesel fuel were diluted 1:10 with HPLC grade hexanes and analyzed using the chromatographic method described above. Ions of interest for the LSH component ranging from C_8 – C_{20} were evaluated. Values were normalized by the sum of all ions detected per sample.

Appendix

Table 2.1. Average percent abundance and standard deviation (listed in percentage) of ions observed during LSH analysis for a standard solution of C_8 – C_{20} LSHs (n = 9)

LSH	**$[M - H]^+$**	**$[M - 3H + O]^+$**	**$[M - H + O]^+$**	**$[M - 5H + 2O]^+$**	**$[M - 3H + 2O]^+$**	**$[M - H + 2O]^+$**
Octane (C_8)	ND	38.2% ± 3.5%	45.9% ± 6.3%	ND	15.7% ± 14.1%	ND
Nonane (C_9)	ND	39.1% ± 4.3%	45.5% ± 5.3%	ND	15.2% ± 9.6%	ND
Decane (C_{10})	ND	33.9% ± 2.3%	53.2% ± 2.2%	ND	12.7% ± 7.4%	ND
Undecane (C_{11})	ND	30.6% ± 3.2%	52.7% ± 2.8%	6.4% ± 12.3%	10.1% ± 6.9%	ND
Dodecane (C_{12})	ND	32.0% ± 2.3%	53.7% ± 1.5%	4.0% ± 7.9%	10.1% ± 6.3%	ND
Tridecane (C_{13})	ND	33.0% ± 1.7%	53.5% ± 2.3%	3.7% ± 9.8%	9.7% ± 7.6%	ND

Table 2.1 continued

Tetradecane (C_{14})	**ND**	**33.8% ± 3.9%**	**50.4% ± 3.4%**	**3.9% ± 10.2%**	**9.9% ± 5.6%**	**1.8% ± 14.0%**
Pentadecane (C_{15})	ND	34.0% ± 2.8%	49.2% ± 2.6%	5.8% ± 8.7%	9.2% ± 3.9%	1.7% ± 11.0%
Hexadecane (C_{16})	0.9% ± 21.0%	36.2% ± 2.9%	46.8% ± 2.2%	7.0% ± 16.6%	9.0% ± 6.6%	ND
Heptadecane (C_{17})	3.4% ± 32.3%	32.1% ± 1.8%	48.0% ± 3.7%	3.9% ± 8.6%	8.6% ± 5.3%	3.7% ± 11.8%
Octadecane (C_{18})	5.7% ± 19.7%	33.7% ± 3.8%	43.1% ± 3.3%	4.5% ± 8.1%	10.0% ± 4.9%	2.8% ± 10.5%
Nonadecane (C_{19})	2.8% ± 14.2%	37.6% ± 2.4%	42.2% ± 3.7%	4.3% ± 8.8%	10.3% ± 5.5%	2.5% ± 11.3%
Eicosane (C_{20})	3.2% ± 10.6%	36.9% ± 2.4%	42.0% ± 3.1%	4.1% ± 8.8%	10.8% ± 4.5%	2.7% ± 11.0%

ND: not detected

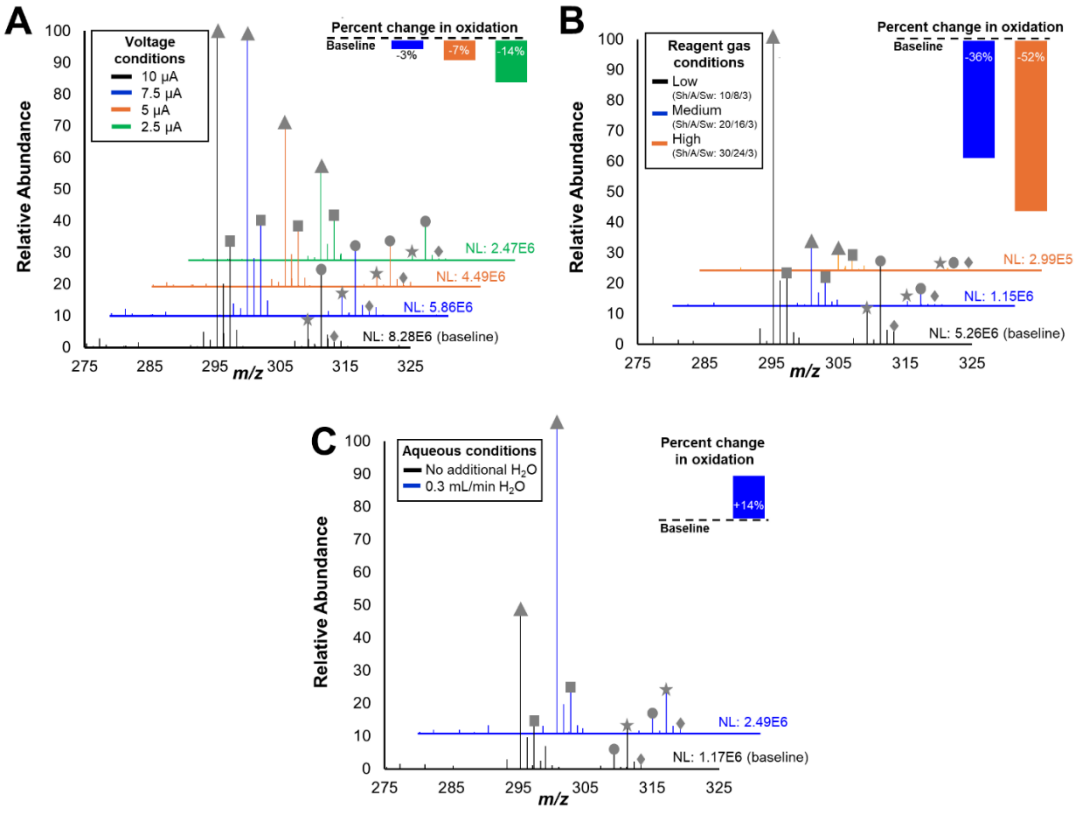

Figure 2.6. Evaluation of eicosane ($C_{20}H_{42}$) oxidation products using GC-APCI-HRMS under variable A) corona discharge current, B) reagent gas (nitrogen) level, and C) atmospheric water concentration. The normal operating conditions are termed "baseline" and the percent change in oxidation products (normalized by the sum of all ions detected) is illustrated by the bar graphs. NL: normalization level. Note: sweep (Sw) gas was not altered in reagent gas studies as increasing this parameter was expected to simply reduce the ions entering the inlet and prevent the acquisition of informative spectra.

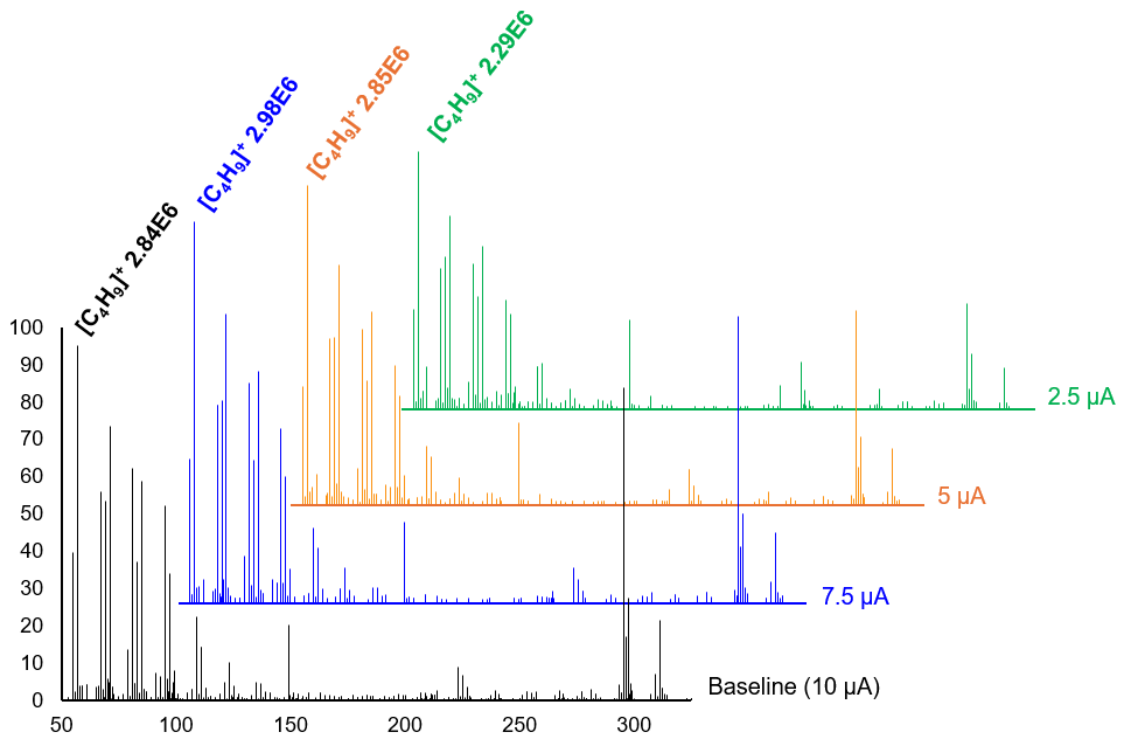

Figure 2.7. A) Overlay of eicosane ($C_{20}H_{42}$) analyzed under the following discharge currents: 10 µA (black trace, baseline), 7.5 µA (blue trace), 5 µA (orange trace), and 2.5 µA (green trace). The base peak of each trace is labeled with the NL.

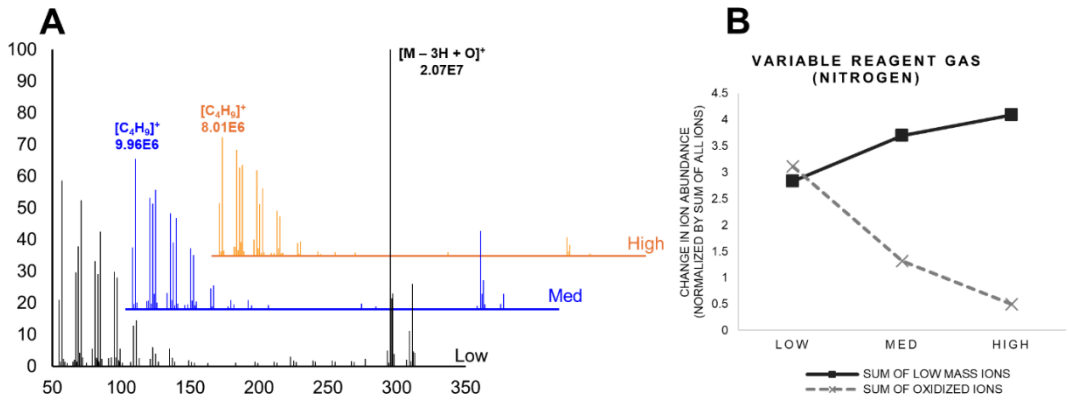

Figure 2.8. A) Overlay of eicosane ($C_{20}H_{42}$) analyzed under low (black trace), medium (blue trace), and high (orange trace) reagent gas (i.e., nitrogen) conditions from *m/z* 50 – 350 where the base peak of each trace is labeled with the NL. B) Indirect correlation between highly fragmented, low mass ions (i.e., $[C_4H_9]^+$, $[C_5H_{11}]^+$, and $[C_6H_{13}]^+$) resulting from radical mechanisms and oxidized ions with increasing reagent gas conditions.

Table 2.2. Aqueous infusion experiments with stable isotope labeled analytes

Analysis of $C_{20}H_{42}$ with H_2O			**Analysis of $C_{20}H_{42}$ with D_2O**			**Analysis of $C_{20}D_{42}$ with H_2O**		
Observed *m/z*	Corresponding formula (± 5 ppm)	Ion after change from parent structure ($C_{20}H_{42}$)	Observed *m/z*	Corresponding formula (± 5 ppm)	Ion after change from parent structure ($C_{20}H_{42}$)	Observed *m/z*	Corresponding formula (± 5 ppm)	Ion after change from parent structure ($C_{20}H_{42}$)
295.2995	$[C_{20}H_{39}O]^+$	$[M - 3H + O]^+$	295.2995	$[C_{20}H_{39}O]^+$	$[M - 3H + O]^+$	334.5435	$[C_{20}D_{39}O]^+$	$[M - 3D + O]^+$
297.3149	$[C_{20}H_{41}O]^+$	$[M - H + O]^+$	298.3214	$[C_{20}H_{40}DO]^+$	$[M - 2H + D + O]^+$	337.5654	$[C_{20}HD_{40}O]^+$	$[M - 2D + H + O]^+$
309.2785	$[C_{20}H_{37}O_2]^+$	$[M - 5H + 2O]^+$	309.2785	$[C_{20}H_{37}O_2]^+$	$[M - 5H + 2O]^+$	346.5103	$[C_{20}D_{37}O_2]^+$	$[M - 5D + 2O]^+$
311.2941	$[C_{20}H_{39}O_2]^+$	$[M - 3H + 2O]^+$	312.3006	$[C_{20}H_{38}DO_2]^+$	$[M - 4H + D + 2O]^+$	349.5322	$[C_{20}HD_{38}O_2]^+$	$[M - 4D + H + 2O]^+$
313.3105	$[C_{20}H_{41}O_2]^+$	$[M - H + 2O]^+$	315.3226	$[C_{20}H_{39}D_2O_2]^+$	$[M - 3H + 2D + 2O]^+$	352.5539	$[C_{20}H_2D_{39}O_2]^+$	$[M - 3D + 2H + 2O]^+$

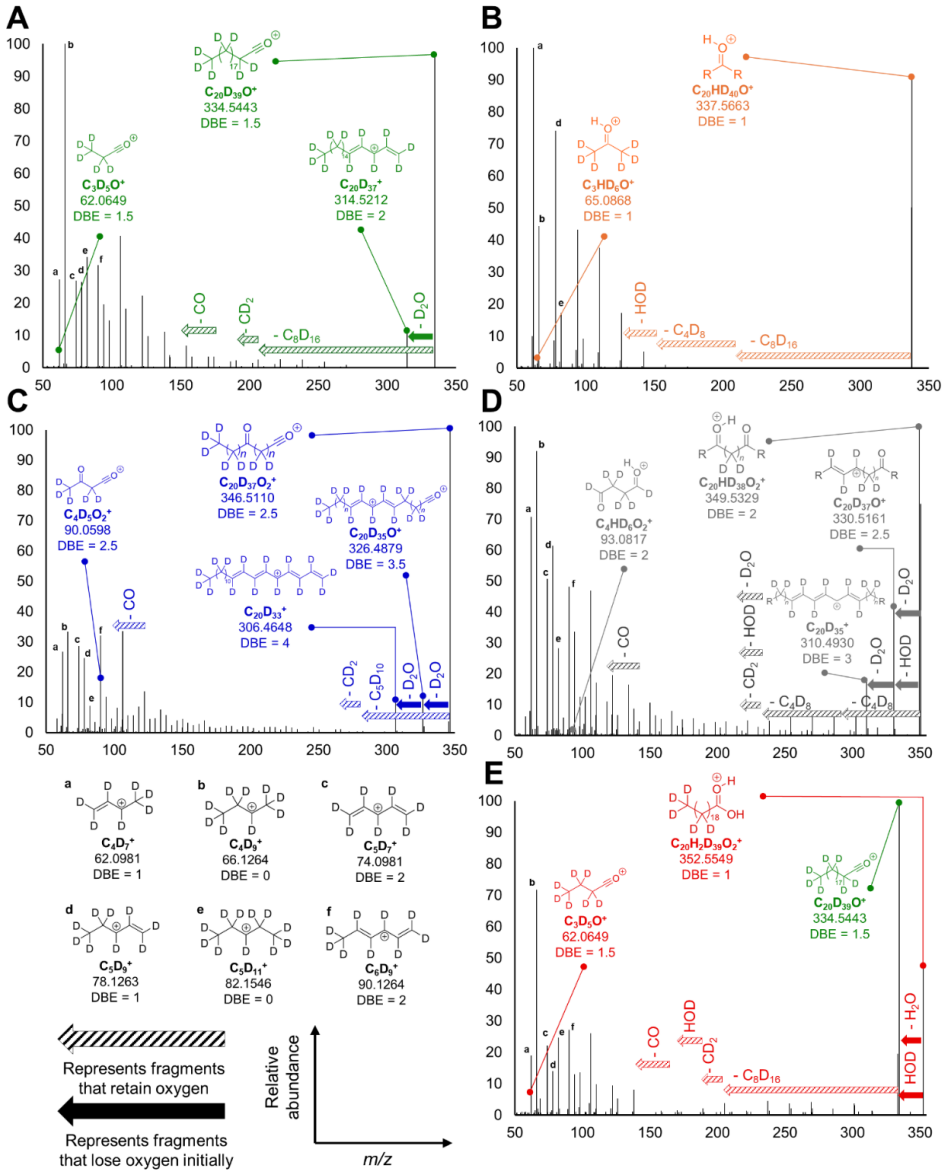

Figure 2.9. MS^2 spectra for A) $[C_{20}D_{39}O]^+$, B) $[C_{20}HD_{40}O]^+$, C) $[C_{20}D_{37}O_2]^+$, D) $[C_{20}HD_{38}O_2]^+$, and E) $[C_{20}H_2D_{39}O_2]^+$ from the analysis of $C_{20}D_{42}$ with H_2O infusion. Theoretical intact structures and important fragments are shown in each spectrum. Not all resonance structures are shown. Notable losses from the precursor ion that retained oxygen are shown by striped arrows and solid arrows represent initial loss of oxygen. Lowercase letters represent common fragments.

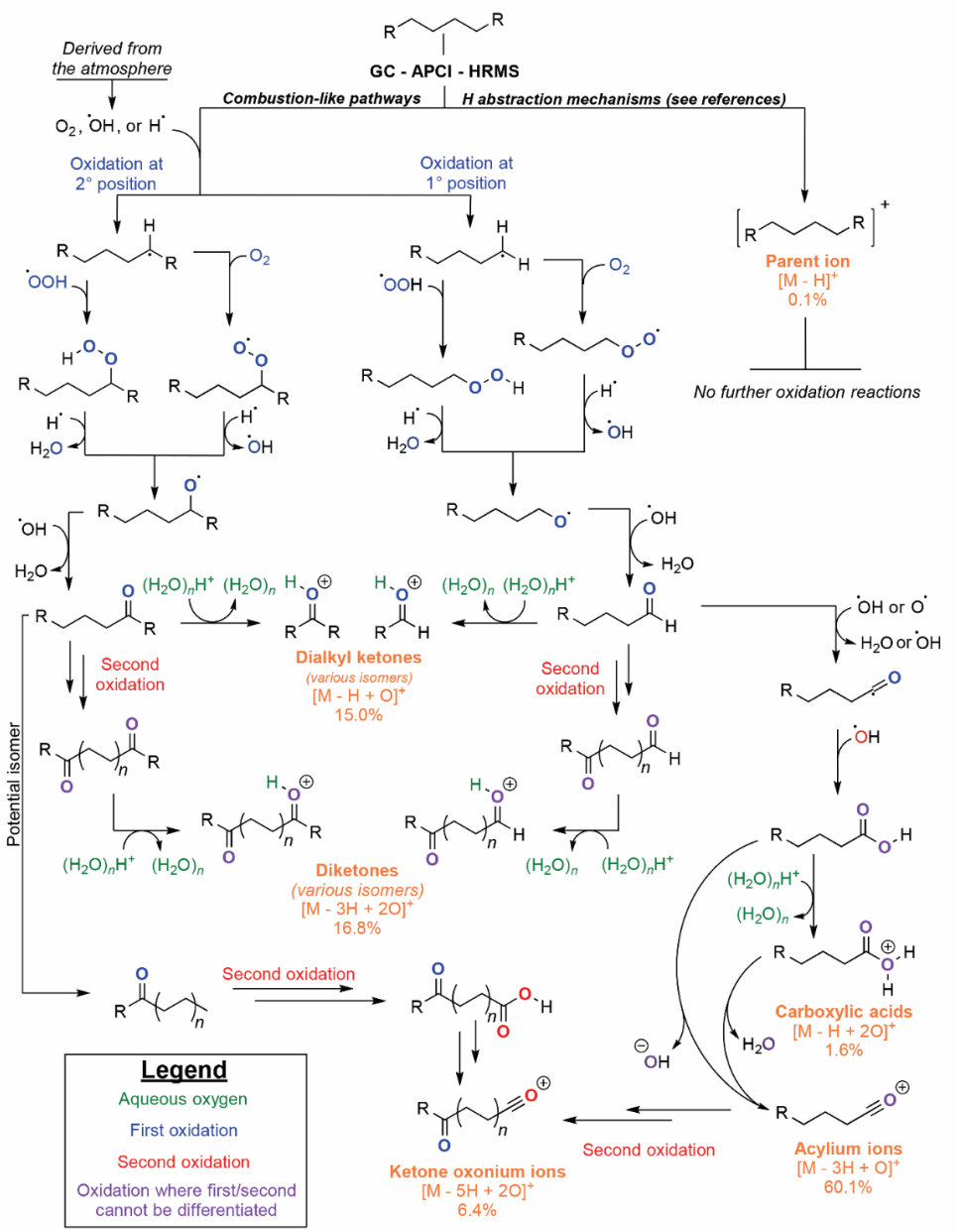

Figure 2.10. Proposed ionization mechanisms to generate the observed minor $[M - H]^+$ ion[25, 53, 54] and major oxidation products via combustion-like pathways[46] for LSHs using GC-APCI-HRMS. Elements arising from atmospheric water are shown in green while elements contributed from non-aqueous sources are shown in blue and red representing the first and second oxidation, respectively. Purple elements indicate that two oxidations have occurred, where either oxygen could arise from either oxidation step. Ions observed during analyses and their relative abundances are shown in orange.

CHAPTER 3.

MITIGATING IN-SOURCE OXIDATION IN BIOLOGICAL MATRICES

Autoinducer-2 is a Metabolic Byproduct in Non-pathogenic E. coli

3.1 Abstract

The highly regulated signaling systems in bacteria allow these organisms to execute various physiological functions among bacterial communities through the regulation of gene expression. This process, termed quorum sensing, is largely mediated by two families of signaling molecules – autoinducer 1 and 2 (AI-1 and AI-2, respectively). Some bacteria, like the aquatic pathogen *Vibrio harveyi*, utilize both AI-1 and AI-2 to induce infection in marine species, as well as promote bioluminescence. Pathogenic strains of *Escherichia coli*, however, only utilize AI-2 to promote virulence. Non-pathogenic strains of *E. coli* (i.e., Keio collection strains) exhibit tendencies to produce AI-2 in an unregulated manner, begging the question as to why this organism produces AI-2 when pathogenesis is not possible. In this study, potential biological purposes as to why non-pathogenic *E. coli* produces AI-2 via the activated methyl cycle (AMC) are investigated through the analysis of a non-pathogenic *E. coli* wildtype and a *ΔluxS* mutant that cannot produce AI-2. Because the AMC is important to many essential biological functions (i.e., epigenetic modification, cell to cell signaling, and metabolism), DNA methylation, quorum sensing molecule production, and metabolism were monitored. Analysis of global DNA methylation between *E. coli* phenotypes indicated no significant differences, suggesting *E. coli* does not produce AI-2 as a byproduct of genetic regulation. In comparison to the *ΔluxS* mutant and *V. harveyi* phenotypes, the *E. coli* wildtype accumulated more AMC-related metabolites. Untargeted metabolomics revealed that the knockout of the LuxS gene impacted coenzyme biosynthesis, a perturbation that was suspected to impact fatty acid biosynthesis and induce lipidome alterations. Lipidomics data indicated that *E. coli* (regardless of LuxS) alters its lipid composition over time. Taken together, these studies suggest that when nutrients (i.e., glucose) are in excess, non-pathogenic *E. coli* utilizes the AMC to synthesize acetyl coenzyme A to induce fatty acid biosynthesis and membrane changes. Therefore, it was concluded that AI-2 is simply a byproduct of metabolism in *E. coli* when virulence induction is not possible.

3.2 Introduction

The ability of bacterial cells to communicate between and within species through the production of various small molecule signals, termed autoinducers (AIs), has long been referred to as quorum sensing.[55-57] Bacterial organisms that produce these chemical signals often use them to perform specific physiological functions (i.e., bioluminescence, virulence, biofilm formation, etc.) amongst many cells once the threshold of a specific AI has been exceeded.[57, 58] It has been shown that some species use quorum sensing to induce a specific phenotype through regulation of gene expression – a change which can be inherited from parent cells to progeny, resulting in a long-term, phenotypical adaptation.[59, 60]

Many bacterial species have been heavily studied for their quorum sensing aptitude, including the opportunistic pathogen *Escherichia coli* and the aquatic pathogen *Vibrio harveyi*.[61, 62] In fact, *V. harveyi* was the first species in which an AI was identified as an acyl-homoserine lactone (AHL), representing AI-1 intraspecies quorum sensing signals.[63] Contrarily, *E. coli* does not synthesize AHLs for intraspecies communication, yet both species contain the LuxS gene, which promotes the synthesis of the interspecies signal, AI-2.[64-67] In *V. harveyi*, both AI-1 and AI-2 quorum sensing signals are well-known to influence bioluminescence and virulence.[68] Contrarily, *E. coli* (specifically the infectious strain O157:H7) only utilizes AI-2 quorum sensing to control virulence.[61] Despite its inability to become virulent, non-pathogenic strains of *E. coli* (i.e., BW25113 from the Keio collection) still produced significant amounts of AI-2, seemingly in response to available nutrients.[69-71] This phenomenon was not observed in *V. harveyi*, which regulates AI-2 production to communicate cell density.[69, 70] Thus, it is suspected that non-pathogenic *E. coli* does not utilize AI-2 for quorum sensing purposes.

Importantly, AI-1 and AI-2 production are controlled by a single metabolic pathway – the activated methyl cycle (AMC; **Figure 3.1**).[65, 72] AI-1 is generated using the precursor *S*-adenosyl methionine, which also serves as a methyl donor for various critical functions, most notably DNA methylation. AI-2 is generated via the LuxS enzyme, which converts

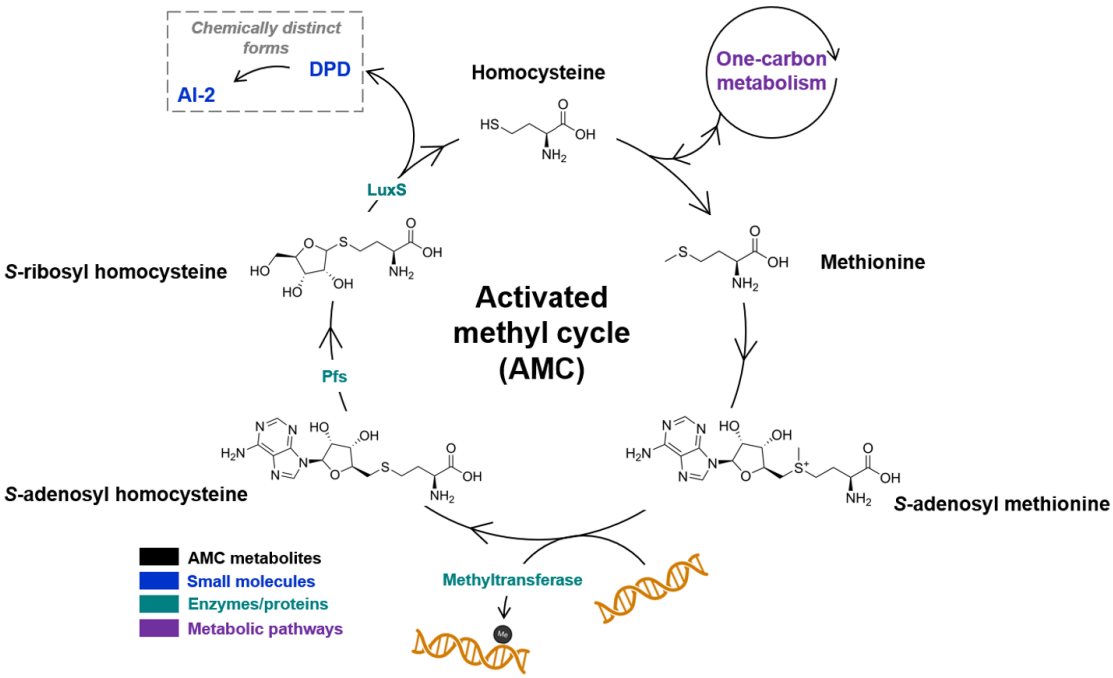

Figure 3.1. The metabolic pathway of the AMC. This cycle is responsible for quorum sensing, epigenetic modification, alterations in metabolism.

S-ribosyl homocysteine to homocysteine and generates organism-specific, chemically distinct forms of dihydroxypentanedione (DPD) as a byproduct.[65] Specifically, *V. harveyi* has been shown to produce DPD in the form of 4,5-dihydroxy-2,3-pentanedione that yields a specific AI-2, elucidated as (2S,4S)-2-methyl-2,3,3,4-tetrahydroxyhydrofuran-borate.[62, 66] Upon the generation of homocysteine, this metabolite may feed back into the AMC or other metabolic cycles, such as one-carbon metabolism.

Although the AMC represents an intersection between many essential biological functions (i.e., quorum sensing, epigenetic modification, and metabolism), this metabolic cycle requires relatively uncommon sulfur-containing compounds and produces toxic intermediates (e.g., *S*-adenosyl homocysteine) that must be immediately recycled. This begs the question as to why *E. coli* would complete this cycle to produce AI-2 if not for use a quorum sensing signal. Herein, we investigate potential biological purposes behind the AMC in *E. coli*. In this study, both *E. coli* and the model quorum sensing species, *V. harveyi*, were evaluated. To investigate the potential for AI-2 to drive phenotypical differences, both the wildtype and ***ΔluxS*** mutant (incapable of synthesizing DPD) of each strain were analyzed. These evaluations suggest that AI-2 is a byproduct of lipid composition remodeling in non-pathogenic *E. coli*.

3.3 Results and discussion

3.3.1 ***E. coli produces AI-2 in response to available nutrients***

Previously, it was shown that potential AI-2 production in *E. coli* steadily increased in response to added nutrients, followed by a steady decrease once nutrients were consumed.[69-71] Importantly, this phenomenon was not observed in *V. harveyi*, which appears to regulate AI-2 production regardless of available nutrients.[69] To confirm that the same patterns were observed in the current study, the levels of DPD (the precursor to AI-2) were quantified using an established derivatization procedure (**Figure 3.2**).[71] In response to 0.2% (w/v) added glucose, *E. coli* showed a similar trend to what was previously reported in the literature.[71] Specifically, the *E. coli* wildtype did not regulate levels of AI-

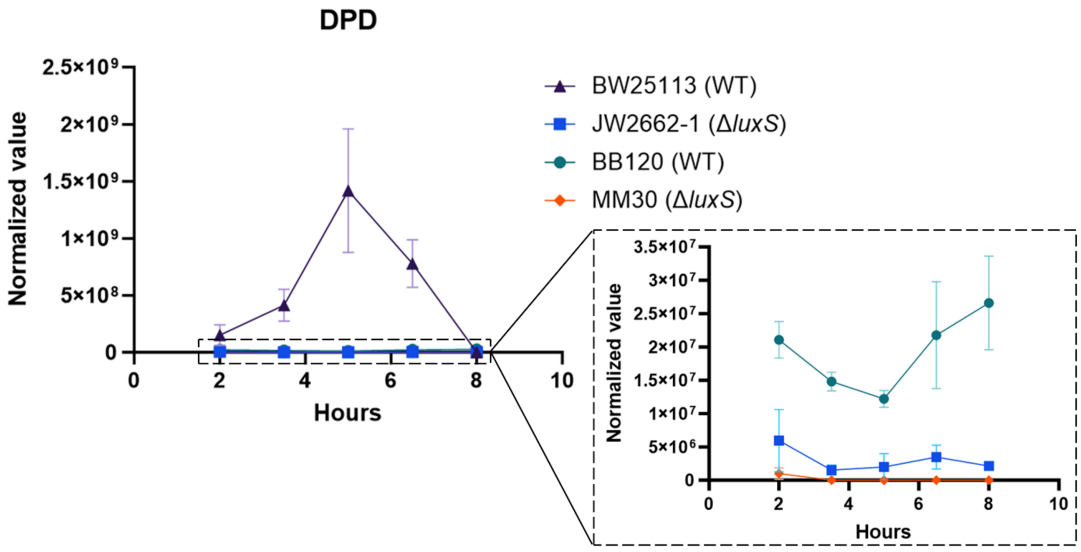

Figure 3.2. Potential AI-2 production as determined through the measurement of DPD in *E. coli* and *V. harveyi* ***ΔluxS*** mutants and wildtypes supplemented with 0.2% (w/v) added glucose. Levels of DPD detected in the ***ΔluxS*** mutants represent the baseline. *V. harveyi* wildtype exhibited levels of DPD slightly above baseline, but remained relatively consistent over time. Levels of DPD were not regulated in the *E. coli* wildtype and appeared to respond to available nutrients. Values were normalized by dividing the area detected for DPD by the cell density at each timepoint.

2 evident by the change in DPD production over the time tested (i.e., 8 hours). Contrarily, the *V. harveyi* wildtype produced low, consistent levels of DPD while both ***Δ****luxS* mutants exhibited baseline levels.

3.3.2 ***Global epigenetic modification remains unchanged between wildtypes and ΔluxS mutants***

To investigate the possibility that *E. coli* utilizes the AMC for the purpose of modifying its epigenome in response to the interspecies signal AI-2, genomic DNA from wildtype and ***Δ****luxS E. coli* and *V. harveyi* was extracted and purified, and the percent methylation of each strain was quantitated over the timepoints tested. A significant difference in methylation was evident between the two bacterial species (**Figure 3.3**), yet there was no significant difference within either species at any one timepoint. Importantly, the level of global methylation did not change over time within either species, suggesting that each species regulates global DNA methylation regardless of AI-2 synthesis.

This does not negate, however, phenotypical changes in response to AI-2 that do not result in global DNA methylation differences. For example, it is possible that *E. coli* may utilize the AMC for epigenetic modification of few genes in response to external stimuli, resulting in non-detectable changes in DNA methylation levels. To be certain of methylation levels at the single-base level, more sensitive methods would be required (e.g., whole genome sequencing).

3.3.3 ***E. coli accumulates more AMC metabolites than V. harveyi***

To evaluate potential impacts that AI-2 has on the AMC, associated metabolites were qualitatively analyzed. Because the components of the AMC are relatively unstable and prone to in-source oxidation, cell extracts and supernatants were derivatized prior to analysis using a modified procedure.[72] Multiple pairwise comparisons were made at $t = 5$ h to evaluate potential metabolic differences between the *E. coli* wildtype and ***Δ****luxS* mutant, *V. harveyi* wildtype and ***Δ****luxS* mutant, as well as *E. coli* and *V. harveyi* wildtypes (**Figure 3.4**).

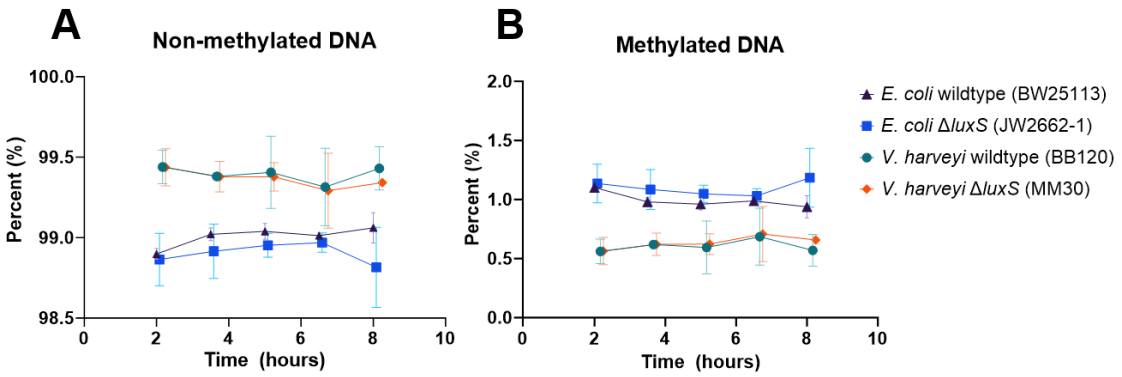

Figure 3.3. Percentages of global A) non-methylated and B) methylated DNA among *E. coli* and *V. harveyi* wildtype and *ΔluxS* mutants. Levels of methylation remained consistent within each species and did not appear to correlate with the AI-2 production in the *E. coli* wildtype.

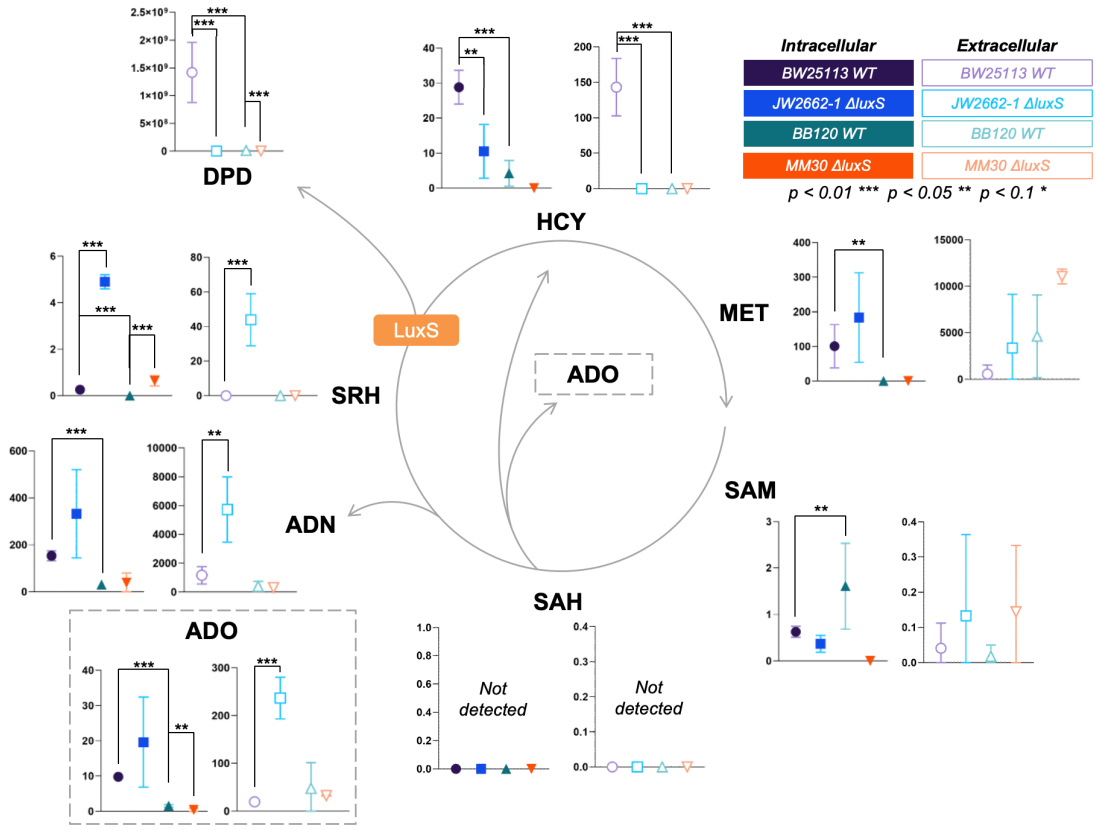

Figure 3.4. Analysis of intracellular and extracellular AMC metabolites in *E. coli* and *V. harveyi* wildtypes and *ΔluxS* mutants at $t = 5$ hours. Pairwise comparisons were made between *E. coli* wildtype and *ΔluxS* mutant, *V. harveyi* wildtype and *ΔluxS* mutant, and *E. coli* and *V. harveyi* wildtypes. Intracellular evaluations are shown with filled symbols while extracellular comparisons are shown in outlined symbols. Significance is indicated for each comparison. HCY: homocysteine; MET: methionine; SAM: *S*-adenosyl methionine; SAH: *S*-adenosyl homocysteine; AND: adenine; ADO: adenosine; SRH: *S*-ribosyl homocysteine.

As expected, DPD was detected in higher abundance in the wildtypes compared to their *ΔluxS* mutants. As a consequence of the *ΔluxS* knockout, SRH was significantly increased in mutants of both species. In *E.* coli, however, SRH was significantly more abundant both intra- and extracellularly, while *V. harveyi* only exhibited greater concentrations within the cell. This suggests that *E. coli* has the ability to excrete SRH to the extracellular matrix.

SAH was not detected in any of the samples as this metabolite and its byproducts (ADN and ADO) are tightly regulated due to their intracellular toxicity.[73] Both ADN and ADO were present in higher abundance in the *E. coli* wildtype compared to *V. harveyi*. However, in the extracellular space, the *E. coli ΔluxS* knockout exhibited significantly greater levels of these byproducts. Excretion of ADN and ADO likely represents a negative feedback loop to regulate levels of SAH and SRH in the cell, which appear to be in greater abundance in *E. coli* than *V. harveyi*.

SAM, another metabolite that exhibits toxicity in high amounts, was only found to be significantly abundant in the *E. coli* wildtype compared to the *V. harveyi* wildtype.[74] However, considering this metabolite is also highly regulated by the cell, the levels of SAM were consistently low in all cultures.

Levels of HCY were significantly greater intra- and extracellularly in the *E. coli* wildtype when compared to other strains. Substantial HCY build-up appears to be attributed to excessive metabolic AMC activity, but may also be the result of multiple metabolic processes.[75, 76]

Intra- and extracellular levels of multiple AMC metabolites were significantly greater in *E. coli* compared to *V. harveyi*. Whether this is a result of greater AMC activity in *E. coli* compared to *V. harveyi* or that *V. harveyi* utilizes AMC metabolites for downstream metabolic processes requires further investigation. Regardless, it appears more likely that, in response to available nutrients, DPD and AI-2 serve as metabolic byproducts in non-pathogenic *E. coli* rather than a quorum sensing signal.

3.3.4 ***Coenzyme biosynthesis is important factor in E. coli metabolism***

To investigate potential impacts AI-2 may have on metabolism, wildtype and *ΔluxS* strains of *E. coli* and *V. harveyi* were subjected to untargeted metabolomics. Differential analysis between the phenotypes indicated 129 features in *E. coli* and 283 features in *V. harveyi* were significantly different, while 1368 features were significantly altered between the two wildtypes (**Figure 3.5**). Significant features were composed of both known metabolites annotated using fragmentation data as well as unannotated features. A pathway analysis demonstrated that no common pathways were significantly altered between *V. harveyi* and *E. coli* (**Figure 3.5A** and **B**), hinting at the diverse impact AI-2 has on these species. Of the pathways affected by the inability to produce AI-2 in *E. coli*, three (specifically, alanine, aspartate, and glutamate metabolism, beta-alanine metabolism, and pantothenate and coenzyme A (CoA) biosynthesis) were linked to coenzyme biosynthesis. Indeed, calculated fold changes at this timepoint indicate that the mutant displayed significantly higher abundance of acetyl CoA and pantothenate than the wildtype (**Figure 3.5D**). Coenzymes are utilized in numerous essential biological functions and changes in their biosynthesis could have multiple biological implications.[77-79] Perturbations in coenzyme biosynthesis in the *E. coli ΔluxS* mutant are speculated to be due to the disruption of the AMC (i.e., the inability to convert SRH to HCY) rather than the inability to produce AI-2.

Metabolic pathways significantly affected in *V. harveyi* primarily involved cycles in which pyruvate plays a substantial role (i.e., pyruvate metabolism, tricarboxylic acid (TCA) cycle, glyoxylate and dicarboxylate metabolism, and methane metabolism). Additionally, heatmaps indicate that TCA cycle intermediates were significantly more abundant in the wildtype than the mutant (**Figure 3.5D**). When supplemented with glucose, luminous marine bacteria (including *Vibrio* species) exhibit tendencies to excrete excess pyruvate catabolized from glucose to regulate levels of this metabolite inside the cell.[80] The AMC also influences the production of pyruvate through conversion of HCY to cystathionine and cysteine.[75] Therefore, the disruption of the AMC in *V.*

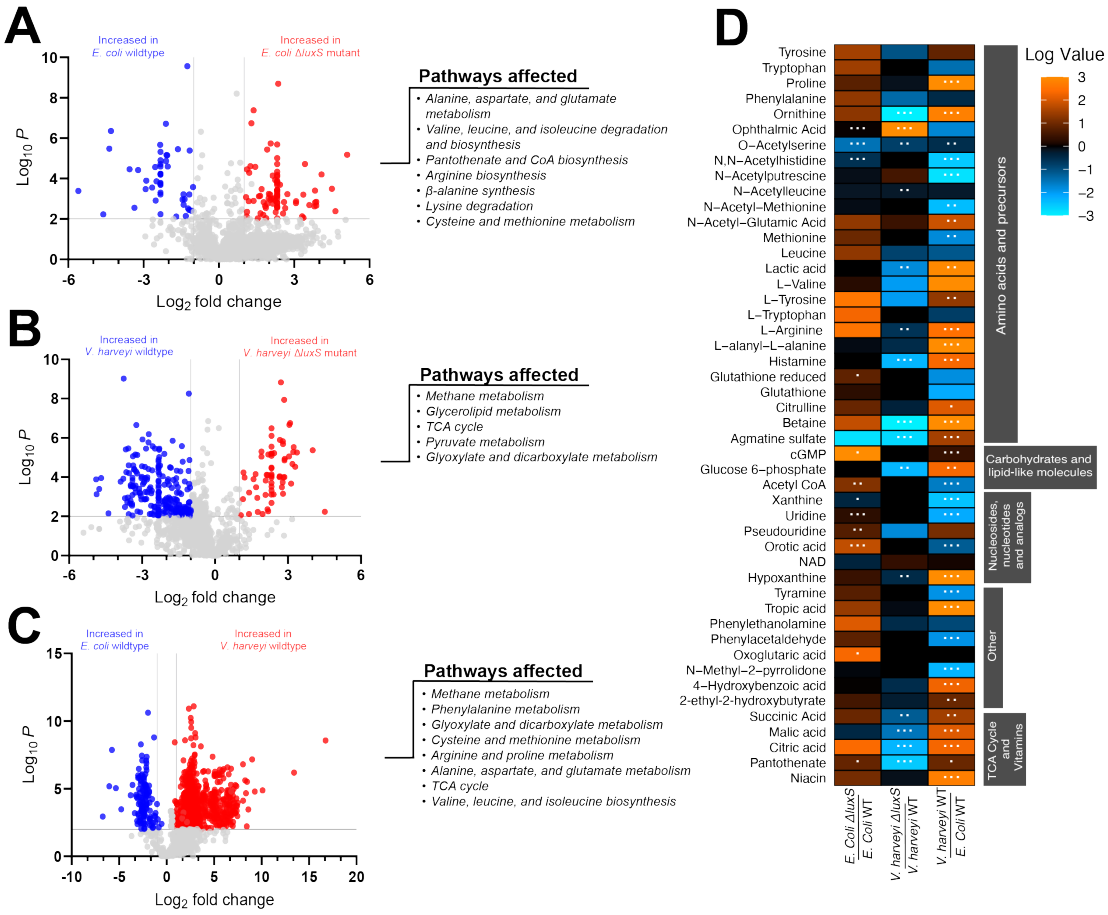

Figure 3.5. Untargeted metabolomics analysis at $t = 5$ h. Volcano plots and pathway analyses illustrate differential analyses between A) *E. coli* wildtype and *ΔluxS* mutant, B) *V. harveyi* wildtype and *ΔluxS* mutant, and C) *E. coli* and *V. harveyi* wildtypes. D) The heatmap shows fold changes and statistical significance for features that were confirmed by MS^2 matching. Note: $p < 0.01$ ***, $p < 0.05$ **, $p < 0.1$ *

harveyi ΔluxS likely induces the observed shifts in pyruvate biosynthesis as glucose catabolism is able to supplement the diminished pool of pyruvate in the mutant. The inability to communicate cell density through AI-2 production has been shown to alter this species in other physiological ways (i.e., growth rate, dim bioluminescence, volatile organic sulfur gas production, etc.), which certainly attribute to the significant differences observed between phenotypes.[81, 82]

Comparative analysis between the two wildtypes indicated that pathways significantly impacted in **Figure 3.5A** and **B** were also statistically altered between the two species (**Figure 3.5C**). This further suggests the importance of coenzyme biosynthesis and pyruvate biosynthesis to *E. coli* and *V. harveyi*, respectively. The substantial amount of significantly altered features between wildtypes provides some insight as to the considerable differences in metabolism of these two organisms.

3.3.5 Lipid composition changes over time in E. coli

Metabolomics data revealed that pathways related to coenzyme biosynthesis were altered between the wildtype and *ΔluxS* phenotypes of *E. coli.* When supplemented with excess glucose, some bacteria utilize acetyl CoA (derived from glucose) in fatty acid and sterol biosynthesis.[77] This prompted the investigation of the lipidome of *E. coli* wildtype and *ΔluxS* mutant as compared to that of *V. harveyi* phenotypes.

Multivariate analysis of the *E. coli* phenotypes over the time points tested showed clustering that was time-based rather than phenotype-based (**Figure 3.6A**). Specifically, the *E. coli* wildtype and *ΔluxS* mutant displayed noticeable clustering at t = 2 h and t = 3.5 h. The remaining timepoints (i.e., t = 5, 6.5, and 8 h) primarily clustered together. This suggests that, regardless of the ability to produce AI-2, *E. coli* alters its lipidome over time. Importantly, these clusters align with the availability of nutrients (i.e., glucose) in the environment, which have shown to drastically deplete beginning at 5 h.[83] Lipid headgroup analysis between the clustered timepoints revealed significant changes in lipid species. Specifically, PG, PE, TG, and LPE lipids were significantly different between *E. coli* wildtype and mutant at t = 2 and 3.5 h, while PG, PE, and CL lipids were

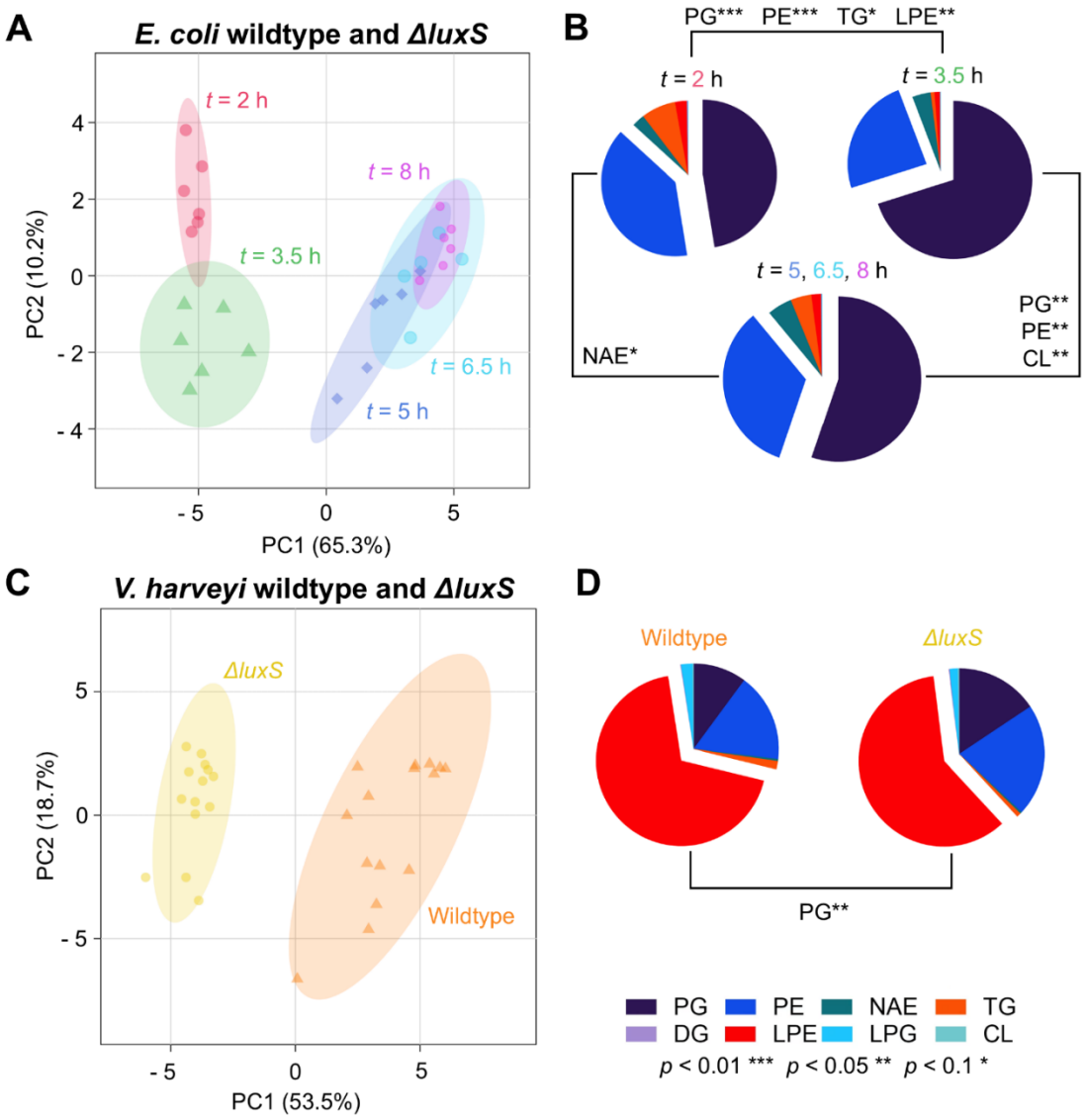

Figure 3.6. Lipidomics analysis of *E. coli* and *V. harveyi* wildtypes and *ΔluxS* mutants. Principal component (PCA) analysis showing the optimal groupings within A) *E. coli* and C) *V. harveyi.* Pie charts and statistical analysis of lipid headgroup changes that drive separation in B) *E. coli* PCA and D) *V. harveyi* PCA.

significantly different at t = 3.5 h and later timepoints (i.e., t = 5, 6.5, and 8 h). Only NAE lipids were significantly different between the 2 h and later timepoints, indicating that significant changes in membrane composition occur from 2 to 3.5 h and resembles initial membrane composition (in terms of species abundance) after 5 h. A fold change analysis indicated that the abundance of multiple PG and PE lipids was altered between the two timepoints (**Figure 3.7**). In general, lower molecular weight lipid species (i.e., 32-carbons and below) were in higher abundance at t = 2 h and in lower abundance at t = 3.5 h, aligning with the understanding of fatty acid synthesis in *E. coli,* which elongates lipid species in response to the availability of acetyl CoA.[84]

The *V. harveyi* lipidome did not cluster based on time, but rather based on phenotype, largely driven by PG lipids. From this, it is clear that the membrane of *V. harveyi* wildtype is different than that of the *ΔluxS* mutant, suggesting AI-2 may play an important role in cell membrane composition. Growth rates in *V. harveyi* have shown to be greater in quorum sensing mutant strains than wildtype strains likely due to the regulation of growth and conservation of nutrients with quorum sensing.[81] Thus, the unique membrane composition in *V. harveyi* wildtype and *ΔluxS* is likely due to regulation of fatty acid biosynthesis tightly regulated by quorum sensing.

3.3.6 E. coli produces AI-2 as a metabolic byproduct during membrane composition changes in a nutrient favored state

Data from this study indicate that, in a nutrient favored state, *E. coli* (specifically, a non-pathogenic strain) alters its lipid composition primarily through coenzyme biosynthesis. The accumulation of AMC metabolites in the *E. coli* wildtype suggests that this metabolic pathway influences the downstream production of coenzymes (specifically, acetyl CoA) to induce membrane changes through fatty acid biosynthesis.

Specifically, the AMC generates HCY, which is then converted to cystathionine and cysteine. HCY (and its subsequent conversion products) are also generated from one-carbon metabolism via the catabolism of glucose.[76] To generate acetyl CoA from cysteine, reaction with D-4'-phosphopantothenate to produce multiple pantothenate-

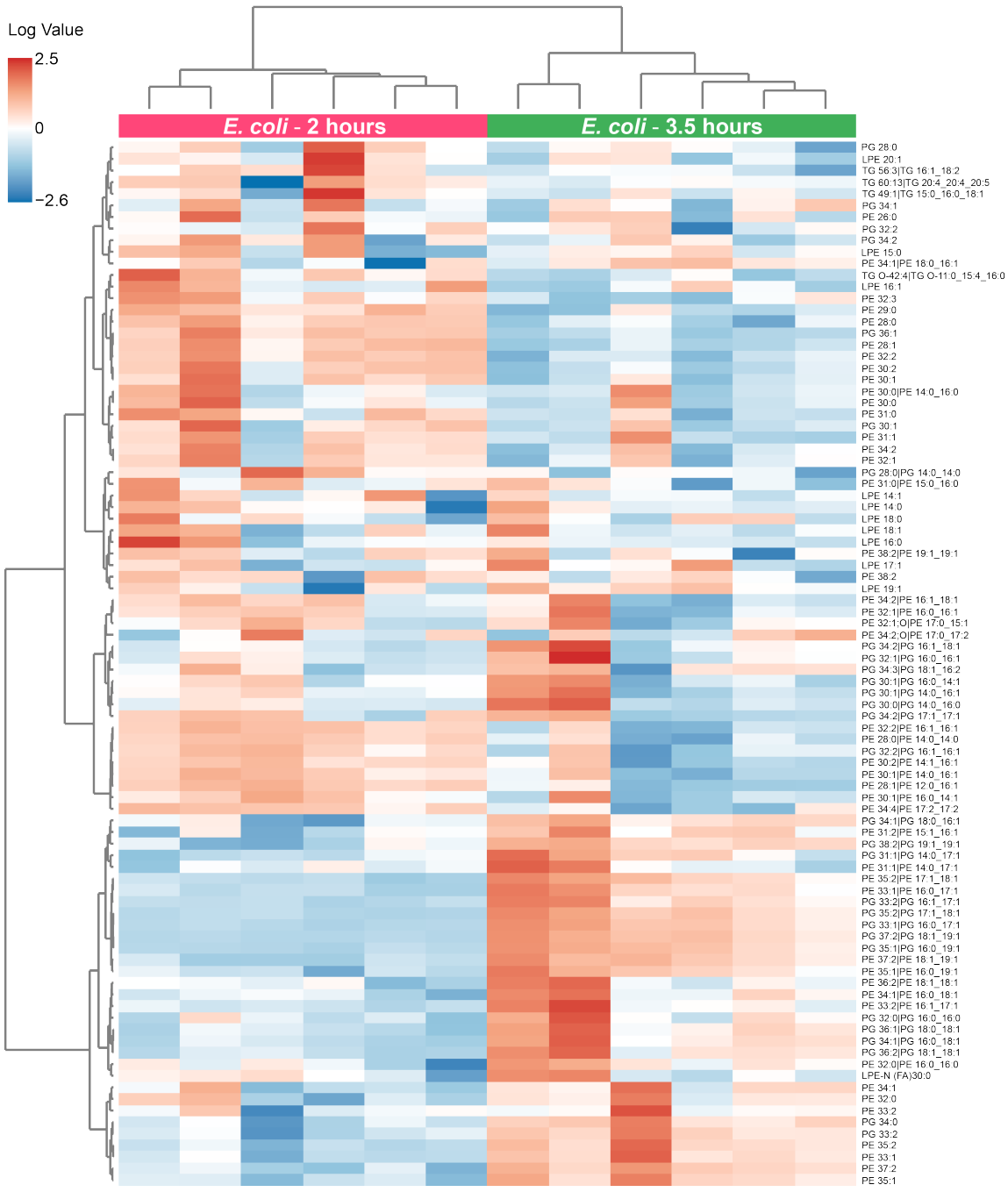

Figure 3.7. Heatmap showing differences of annotated lipids (identified by MS^2 data) of *E. coli* wildtype and mutant biological replicates ($n = 6$) grouped by timepoint (i.e., 2 and 3.5 hours). Data includes lipid species from headgroups that were significantly different between the time points (i.e., PG, PE, LPE, and TG).

based products is required. Interestingly, D-4'-phosphopantothenate was the only metabolite that showed a pattern similar to AI-2 production that seemed to correlate with available nutrients (**Appendix Figure 3.9**) despite the fact that there is no known relationship between AI-2 and D-4'-phosphopantothenate. The current understanding of D-4'-phosphopantothenate synthesis in *E. coli* is that pantothenate degrades to yield β-alanine and pantoate, which are then utilized to synthesize acetyl CoA instead of incorporating the intact pantothenate molecule.[79, 85] Due to increased levels of N-acetyl aspartate in the *ΔluxS* mutant (**Appendix Figure 3.9**), a significant difference in alanine, aspartate, and glutamate metabolism was observed between the *E. coli* phenotypes. N-acetyl aspartic acid plays a role in many biological processes (e.g., amino acid metabolism and biosynthesis) via the conversion to aspartate, yet the metabolic build-up of this molecule may also implicate a relationship between AI-2 and/or DPD to the pantothenate and CoA/β-alanine pathways. It is possible that the LuxS pathway influences coenzyme synthesis through pantothenate and CoA metabolism, but further investigation would be required to conclude this.

Considering lipid composition was statistically similar between *E. coli* phenotypes at specific timepoints, it was suspected that cysteine could be generated from an additional pathway to account for the disruption of the AMC in the *ΔluxS* knockout. Using flux experiments, the recycling of glutathione disulfide to cysteine has been demonstrated in the *E. coli* strains used in this study.[83] Therefore, it was proposed that acetyl CoA and fatty acid biosynthesis was driven by one carbon metabolism and aspartate metabolism in combination with the AMC for the non-pathogenic *E. coli* wildtype or glutathione metabolism when the AMC is disrupted (**Figure 3.8**).

Although the data suggest that AI-2 is a metabolic byproduct in *E. coli*, the potential effects of supplemented DPD and/or antibiotics on the *ΔluxS* mutant are still in question. Thus, to further support the finding that AI-2 represents a metabolic byproduct, an additional study will be performed that supplements the mutant with biologically relevant concentrations of DPD[83] both with and without antibiotics (i.e., kanamycin) to evaluate any potential effects from these excipients.

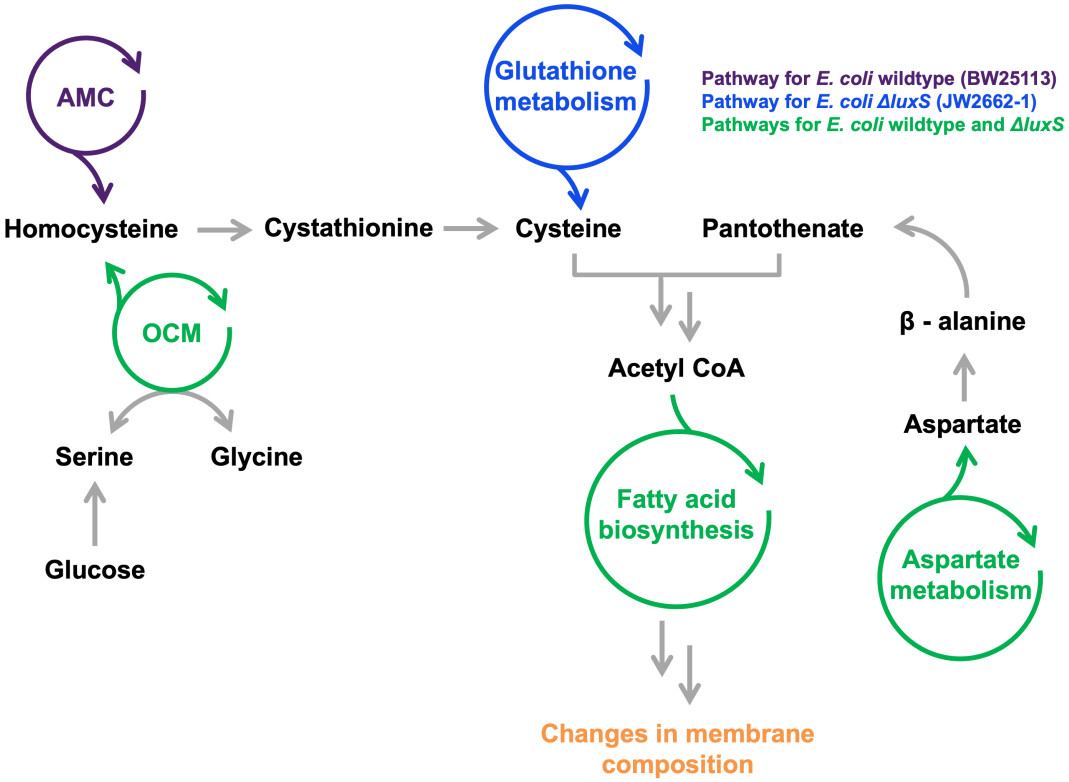

Figure 3.8. Proposed pathways for changes in *E. coli* membrane composition over time. Green cycles are characteristic of both *E. coli* phenotypes, while the purple cycle is specific to *E. coli* wildtype and blue cycle is specific to the *E. coli ΔluxS* mutant that necessitates the recycling of glutathione disulfide to account for disruptions in the AMC.

3.4 Conclusions

In this study, the unregulated production of the quorum sensing signal AI-2 in non-pathogenic *E. coli* was investigated. Because AI-2 is suspected to impact epigenetic modifications, global DNA methylation between *E. coli* that could produce AI-2 via LuxS and a *ΔluxS* knockout were evaluated and found to be statistically similar. Despite the fact that there were no detectable differences in global DNA methylation, the *E. coli* wildtype accumulated more AMC-related metabolites than its *ΔluxS* mutant, as well as the wildtype and *ΔluxS* mutant of the marine pathogen, *V. harveyi*. Untargeted metabolomics revealed that coenzyme biosynthesis pathways were significantly changed in the *E. coli ΔluxS* mutant and was not significantly altered in *V. harveyi*. Because fatty acid biosynthesis is a primary function of coenzymes, specifically acetyl CoA, the lipidomes of *E. coli* phenotypes were evaluated and it was found that, regardless of LuxS activity, the lipid composition of *E. coli* changed with respect to time. This investigation led to the understanding that, in a nutrient favored state (i.e., supplemented with glucose), *E. coli* modifies its membrane composition via the biosynthesis of acetyl CoA through one carbon metabolism, the AMC, and aspartate metabolism. When the AMC is disrupted, as is the case in the *E. coli ΔluxS* mutant, glutathione metabolism is used to compensate for the loss in acetyl CoA production via the generation of cysteine.

In the well-studied organism, *E. coli*, only pathogenic strains are understood to utilize AI-2 as a quorum sensing signal to control virulence. Here, in a non-pathogenic strain, AI-2 is demonstrated to be a metabolic byproduct of acetyl CoA production to induce changes in fatty acid composition. Taken together, these data suggest that quorum sensing may only be utilized in *E. coli* to promote pathogenesis, unlike other bacteria that utilize signaling to promote a multitude of physiological activities.[58]

3.5 Experimental section

3.5.1 ***Bacterial strains and growth conditions***

The *E. coli* strains used in the study were established as part of the Keio Collection[86] and purchased from Coli Genetic Stock Center at Yale University. The wildtype strain used was BW25113 and the *ΔluxS* mutant was JW2662-1. Both strains of

E. coli were grown in Luria-Bertani medium (LB) at 37 °C with aeration, while only the *ΔluxS* mutant was grown on 25 µg/mL of kanamycin. *V. harveyi* strains were graciously gifted from B.L. Bassler (Princeton University and the Howard Hughes Medical Institute). The *V. harveyi* wildtype (BB210) and *ΔluxS* mutant (MM30) were grown on Luria Marine (LM) media at 30 °C with aeration. The *ΔluxS* mutant was supplemented with 25 µg/mL of kanamycin. Overnight cultures of *E. coli* and *V. harveyi* were grown in their respective media and temperatures at 200 rpm and used to perform time-course experiments (from 0 – 8 hours) in biological triplicate with added sterile glucose (0.2% w/v). Bacterial growth was monitored through the timed experiment using optical density (OD_{600}). Growth curves are shown in **Appendix Figure 3.10**.

3.5.2 DPD tagging reagent synthesis

Dimethyl 2,2'-(4,5-diamino-1,2-phenylene)bis(oxy)diacetate was used as the tagging reagent for DPD quantitation. The synthesis of this molecule has been thoroughly described elsewhere.[71]

3.5.3 DPD extraction

At each timepoint, 300 µL of each bacterial culture was aliquoted and centrifuged at 14,000 rpm for 5 minutes. A volume of 260 µL of supernatant was combined with 26 µL of 5 mg/mL TAG diluted in methanol. Samples were allowed to incubate for at least 45 minutes at room temperature protected from light before performing two liquid-liquid extractions with 0.1% acetic acid in ethyl acetate. From each extraction, 100 µL of the acidic ethyl acetate layer was pooled into a vial and dried under nitrogen. Dried extracts were resuspended in 50% acetonitrile before LCMS analysis. Glass vials were used where possible.

3.5.4 DNA purification, extraction, and degradation to nucleosides

Approximately 15 – 20 mL of bacterial culture was aliquoted and centrifuged at 3000 rpm for 10 minutes to produce a sizable pellet. Supernatant was decanted and pellets were extracted using a modified protocol of the Zymo Quick-DNA Miniprep kit (Zymo Research, Irvine, CA, USA). Specifically, pellets were resuspended in 200 µL of MilliQ water. To this suspension, 200 µL of BioFluid & Cell Buffer and 40 µL proteinase

K were added. The solution was vortexed and digested for 30 minutes at 55°C. The samples were centrifuged at max speed for 5 minutes and the supernatant was transferred to a new vial. An aliquot of 500 µL Genomic Binding Buffer was added followed by vortexing. The solution was transferred to a Zymo-Spin™ IIC-XLR Column, placed in a collection tube, and centrifuged at 16,000 rpm for 1 minute. A series of buffers were added separately followed by a centrifugation step before the next addition. The series was as follows: 400 µL DNA PreWash Buffer, 700 µL g-DNA Wash Buffer, 200 µL g-DNA Wash Buffer, followed by 200 µL g-DNA Wash Buffer. Subsequent to the final centrifugation step, an additional "dry-spin" centrifugation step was conducted. Spin columns were placed into a collection vial and 30 µL of water was added. A final centrifugation step was conducted to elute the purified DNA off the column and into the collection vial. DNA concentration and purity was measured using a Thermo Scientific (Waltham, MA, USA) Nanodrop™ One Spectrophotometer. DNA was degraded into individual nucleosides using Zymo DNA Degradase Plus (Zymo Research, Irvine, CA, USA). Briefly, 2000 ng of DNA was combined with 2.5 µL 10X DNA Degradase™ Reaction Buffer and 1 uL DNA Degradase™ Plus. MilliQ water was added to bring the volume to 25 µL. Samples were digested at 37°C overnight followed by a heat-inactivation step at 70°C for 20 minutes. Solutions were then directly analyzed by LCMS.

*3.5.5 **Metabolomics extraction***

Samples for metabolomics analyses were prepared using an adapted extraction procedure.[87] Specifically, 1.5 mL of bacterial culture was filtered through 0.2 µm filters and immediately flash frozen in liquid nitrogen. Frozen filters were stored at -80°C until all samples were ready to be extracted. At the time of extraction, all steps were performed on ice. To extract, filters were placed cell-side down in a petri dish containing ice-cold 1.3 mL extraction solvent (40:40:20 acetonitrile:methanol:water with 0.1% formic acid and an isotopically labeled internal standard) and allowed to extract at -20°C for 20 minutes. Extraction solvent was then transferred to an Eppendorf tube, filters were flipped with sterile tweezers and subsequently rinsed with 400 µL of extraction solvent. Samples were allowed to extract again for 20 minutes at -20°C. Solvent was then pooled,

centrifuged at 4°C for 5 minutes, and the supernatant was transferred to a new centrifuge tube. The cell pellet was resuspended in 200 µL of extraction solvent and extracted at -20°C for an additional 20 minutes. Samples were then centrifuged, supernatant was pooled, and dried under nitrogen. Dried extracts were stored at -80°C and resuspended in 150 µL at the time of analysis using LCMS, which was adapted from a reported method.[88]

*3.5.6 **Extraction of sulfur-containing and unstable metabolites***

To extract sulfur-containing analytes of interest and other compounds that may be sensitive to in-source oxidation, procedures by Halliday and co-workers were utilized with some adaptation.[72] Aliquots of bacterial culture (5 mL) were quenched with 15 mL 0.9% ice cold saline solution and centrifuged at 4°C. The supernatant was decanted into a separate falcon tube. Samples were frozen in liquid nitrogen and lyophilized. Lyophilized samples were resuspended in 80% methanol prepared with an internal standard (0.5 mL for cell pellets and 1 mL for supernatant samples). Cell pellet samples were subjected to two separate freeze-thaw cycles using liquid nitrogen followed by vortexing and sonication. Samples were centrifuged at max speed for 5 minutes and supernatant was added to a separate vial. The previous two steps were repeated with 0.5 mL 80% methanol and the supernatant was pooled, concentrated under vacuum, and lyophilized. For consistency, supernatant samples were subjected to the same processes, but with 2 mL of 80% methanol.

To derivatize compounds following reported procedures[72], all samples (i.e., both cell pellet and supernatant samples) were resuspended in 80 µL water. To each sample, volumes of 0.05 M tris-(hydroxypropyl)phosphine (THP) was added (30 µL in cell pellet samples and 160 µL in supernatant samples). Samples were allowed to derivatize at room temperature shielded from light for 30 minutes. Subsequently, 40 µL of 1:3 pyridine:isobutanol was added to each vial, followed by 10 uL of isobutylchloroformate. Samples were thoroughly vortexed and extracted with 200 µL 1:2 dichloromethane:methyl tert butyl ether. To a glass vial, 150 µL of the top layer (organic

layer) was added and samples were evaporated to dryness. Samples were immediately resuspended in 100 µL 50% methanol and analyzed by LCMS.

*3.5.7 **Lipidomics extraction***

Lipids were extracted using a modified Bligh and Dyer method.[89] Briefly, at each timepoint, 2 mL of cell culture was centrifuged and the supernatant was decanted. Splash Lipidomix (Avanti Polar Lipids, Alabaster, AL, USA) internal standard was added to each sample followed by 750 µL 1:2 chloroform:methanol. Samples were briefly mixed and aliquots of 250 µL chloroform followed by 250 µL water were added. Samples were vortexed and then centrifuged for 10 minutes at 15,000 rpm. The bottom layer was transferred to a glass vial. To the original sample, 250 µL chloroform and 250 µL water were again added. Samples were vortexed and centrifuged for 10 minutes at 15,000 rpm. The bottom layer from the second extraction was pooled into the glass vial. Liquid extracts in glass vials were dried under nitrogen and resuspended in 50% acetonitrile immediately before LCMS analysis.

*3.5.8 **LCMS conditions***

All analyses were conducted using a Thermo (Waltham, MA, USA) Vanquish Horizon liquid chromatography (LC) system with a binary solvent pump coupled to a Thermo (Waltham, MA, USA) Exploris 120 high resolution MS detector with a heated electrospray ionization source. LC and MS conditions specific to each analysis can be found in **Appendix Table 3.1**.

*3.5.9 **Data processing and statistical analyses***

For targeted analyses (i.e., DPD, DNA, and sulfur-containing/unstable metabolites), compound structures were drawn in ChemDraw (Perkin Elmer, Waltham, MA, USA) and analyte peaks were evaluated using El-Maven (Elucidata, San Francisco, CA, USA). Exact mass, fragmentation patterns, and/or retention time confirmation using external standards were used to confirm compound identifications where possible. Excel was used to normalize data and subsequently graphed using GraphPad Prism 10.0 (GraphPad Software, LLC, Boston, MA, USA). All statistical analyses for targeted methods were performed using a Student's t-test (two-tailed, homoscedastic). The

metabolomics data (i.e., untargeted) were evaluated using MZMine 3.[90] Feature finding and compound annotation were performed through MZMine 3, where features were annotated based on both MS^1 using the *E. coli* Metabolome Database (https://ecmdb.ca/) and MS^2 using the MassBank of North America (University of California Davis, Davis, CA, USA). Untargeted lipidomics data was processed using MS-Dial 4.9[91] and features were identified using MS^2 data with the MS-Dial library. Positive and negative mode data were normalized and aligned using in-house Python scripts. Further statistical analysis of untargeted data was conducted using Metaboanalyst 6.0[92] and GraphPad Prism 10.0. Manual evaluation of metabolic pathways was derived using the Kyoto Encyclopedia of Genes and Genomes (KEGG).[75] The heatmap generated for untargeted metabolomics was conducted using an in-house R script.

Appendix

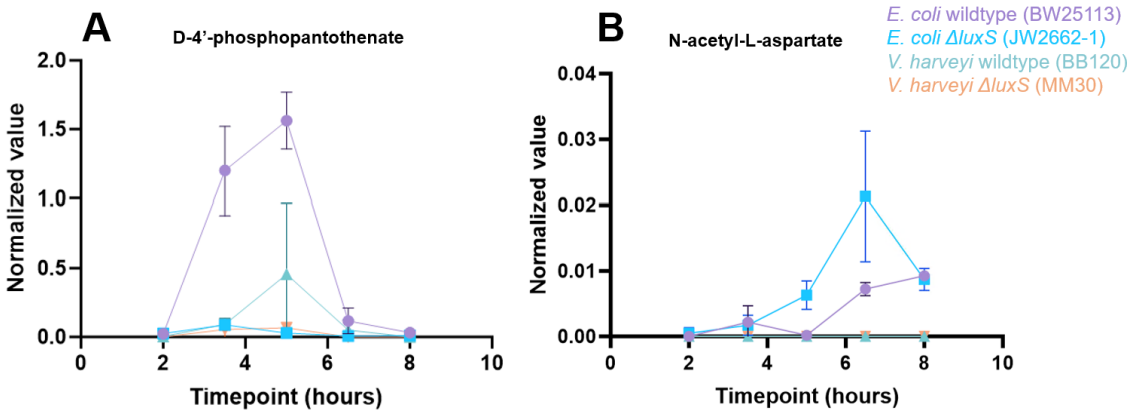

Figure 3.9. Semi-quantitated values of A) D-4'-phosphopantothenate and B) N-acetyl-L-aspartate from untargeted metabolomics data.

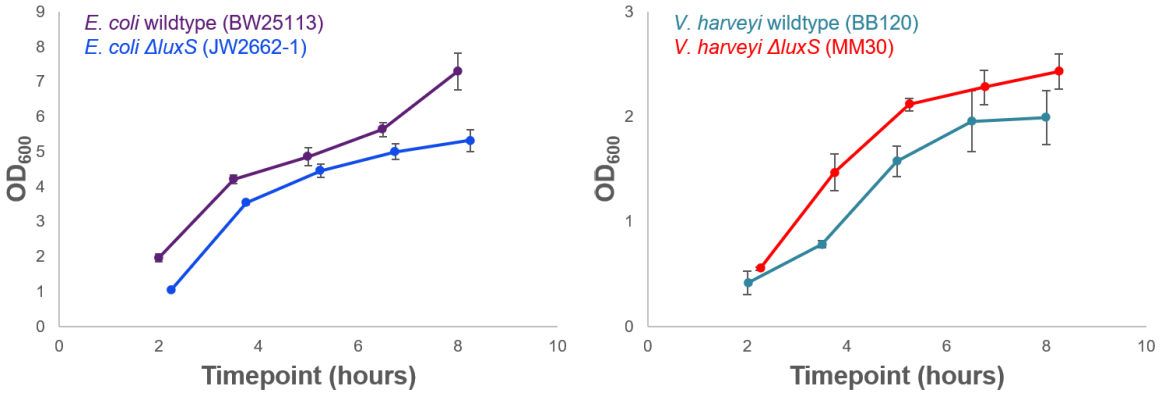

Figure 3.10. Growth curves measured at OD_{600} for the *E. coli* (left) and *V. harveyi* (right) wildtype and ***ΔluxS*** mutant. Measurements were made in biological triplicate.

Table 3.1. LCMS conditions used in each analysis.

Analysis ***Parameters***	**DPD**	**DNA**	**Metabolomics**	**Sulfur-containing/unstable metabolites**	**Lipidomics**
LC parameters					
Mobile phase A	0.1% formic acid in water	0.1% formic acid in water	95:5 water:acetonitrile with 20 mM ammonium acetate and 20mM ammonium hydroxide (pH 9.6)	0.1% formic acid and 10 mM ammonium formate in water	60:40 water:acetonitrile with 10 mM ammonium formate and 0.1% formic acid
Mobile phase B	0.1% formic acid in acetonitrile	0.1% formic acid in 60% acetonitrile	Acetonitrile	0.1% formic acid and 10 mM ammonium formate in methanol	90:10 isopropanol:acetonitrile with 10 mM ammonium formate and 0.1% formic acid

Table 3.1 continued

Mobile phase gradient	0 minutes: 1% B 2 minutes: 1% B 15 minutes: 99% B 17 minutes: 99% B 17.5 minutes: 1% B 20 minutes: 1% B	0 minutes: 1% B 1.5 minutes: 1% B 5 minutes: 4.8% B 17 minutes: 30% B 20 minutes: 99% B 23 minutes: 99% B 23.5 minutes: 1% B 26 minutes: 1% B	0 minutes: 90% B 2 minutes: 90% B 3 minutes: 75% B 7 minutes: 75% B 8 minutes: 70% B 9 minutes: 70% B 10 minutes: 50% B 12 minutes: 50% B 13 minutes: 25% B 14 minutes: 25% B 16 minutes: 0% B 20.5 minutes: 0% B 21 minutes: 90% B 25 minutes: 90% B	0 minutes: 55% B 1.5 minutes: 55% B 15 minutes: 100% B 20 minutes: 100% B 22.5 minutes: 55% B 26 minutes: 55% B	0 minutes: 32% B 1.5 minutes: 32% B 4 minutes: 45% B 5 minutes: 52% B 8 minutes: 58% B 11 minutes: 66% B 14 minutes: 70% B 18 minutes: 75% B 21 minutes: 97% B 25 minutes: 97% B 25.1 minutes: 32% B 30 minutes: 32% B
Flow rate	0.150 mL/min	0.150 mL/min	0.150 mL/min	0.200 mL/min	0.260 mL/min
Method run time	20 minutes	26 minutes	25 minutes	26 minutes	30

Table 3.1 continued

Column	Waters Cortecs® T3 2.1 mm x 150 mm, 2.7 µm	Waters Cortecs® T3 2.1 mm x 150 mm, 2.7 µm	Waters Xbridge BEH amide 2 mm x 150 mm, 2.5 µm	Waters Cortecs® T3 2.1 mm x 150 mm, 2.7 µm	Thermo C30 2.1 mm x 150 mm, 2.6 µm	
Column temperature	25°C	25°C	35°C	30°C	45°C	
MS parameters						
Capillary voltage	3500 V	3500 V	3500 V (+), 2500 (-)	3500 V	3500 V	
Sheath gas	35 arbitrary units	35 arbitrary units	35 arbitrary units	35 arbitrary units	35 arbitrary units	
Auxiliary gas		7 arbitrary units	7 arbitrary units	7 arbitrary units	7 arbitrary units	7 arbitrary units
Sweep gas		0 arbitrary units	0 arbitrary units	0 arbitrary units	0 arbitrary units	0 arbitrary units
Ion transfer tube temperature		320°C	320°C	320°C	320°C	320°C
Vaporizer temperature		275°C	275°C	275°C	275°C	275°C
Resolution (MS1)		120000	120000	120000	120000	120000
Scan range		100-1000 *m/z*	100-1000 *m/z*	70-1000 *m/z*	100-1000 *m/z*	150-2000 *m/z*

Table 3.1 continued

Time	100 ms	100 ms	100 ms	100 ms	100 ms
AGC target	Standard	Standard	Standard	Standard	Standard
Polarity	Positive	Positive	Positive and negative	Positive	Positive and negative
Data dependent acquisition (DDA) isolation window	NA	NA	1.2 *m/z*	2 *m/z*	1.5 *m/z*
DDA resolution	NA	NA	15000	30000	60000

CHAPTER 4.

EVALUATION OF OXIDATION IN SYSTEMS UNDER BIOLOGICAL STRESS

Metabolomic Profiles in Starved Light Breed Horses During the Refeeding Process

Data presented in this chapter has been adapted from the following published journal article:

Main, S.C.; **Brown, L.P**.*; Melvin, K.R.; Campagna, S.R.; Voy, B.H.; Castro, H.F.; Strickland, L.G.; Hines, M.T.; Jacobs, R.D.; Gordon, M.E.; and Ivey, J.L.Z.* "Metabolomic Profiles in Starved Light Breed Horses during the Refeeding Process." *Animals*, **2022**, *12*: 2527. https://doi.org/10.3390/ani12192527

4.1 Abstract

The large population of emaciated horses continues to be an issue troubling the equine industry. However, little is known regarding the collection of equine metabolites (metabolome) during a malnourished state and the changes that occur throughout nutritional rehabilitation. In this study, ten emaciated horses underwent a refeeding process, during which blood samples were collected for a blood chemistry panel and metabolomics analysis via ultrahigh performance liquid chromatography–high resolution mass spectrometry (UHPLC-HRMS). Significant differences among blood chemistry analytes and metabolite and lipid abundance during the critical care period (CCP; Days 1–10 of rehabilitation) and the recovery period (RP; the remainder of the rehabilitation process) were observed. Potentially toxic compounds, analytes related to liver, kidney, and muscle function, as well as energy-related metabolites were altered during the refeeding process. The combination of blood chemistry, metabolomics, and lipidomics analyses on starved equine during rehabilitation provide vital biological insight and evidence that the refeeding process has a significant impact on the equine metabolome.

4.2 Introduction

The equine industry continues to be plagued with a significant number of "unwanted" horses and other equids with an estimated 138,000 equids deemed unwanted in the United States alone each year.[93, 94] For various reasons (including lack of nutritional knowledge by the owner, misalignment of expectation to actual cost of equine ownership, and in some cases, criminal neglect), many unwanted equids can become emaciated.[94] Despite the commonality of emaciated horses, there has been minimal research dedicated to the evaluation of their nutritional recovery and metabolic repair.

The literature describes some studies on rehabilitating or refeeding the starved horse, yet these studies span only 10 to 15 days, while the average refeeding period lasts for several months.[95, 96]

Malnutrition is diagnosed as a lack of nutrition due to inadequate or unbalanced intake of nutrients, or their impaired assimilation or utilization.[97] Severe malnutrition or starvation yields proteolytic and lipolytic responses that can result in negative physiological issues including refeeding syndrome, cachexia, serous atrophy, muscle contractions due to low calcium stores, and heart arrythmia.[98] The Henneke body condition scoring system is an important tool for the rapid, qualitative assessment of nutritional status; however, this system cannot assess the underlying factors associated with respective changes in body composition, metabolism, and overall health.[99] Because malnutrition is a complex condition that is influenced by an array of factors, it is often difficult to determine and label the true state of malnutrition in equids, for which starvation is typically classified using a low body condition score (BCS; < 3 on a 1–9 scale).[94, 99] Elements influencing nutritional status including genetics, background, predisposition to disease, and dietary history are often unidentified within the unwanted and starved horse populations. Thus, a consistent evaluation method coupled with an understanding of changes in metabolism is important to understanding emaciated phenotypes and, if possible, a recovery to a healthy body weight and condition.

A more quantitative approach to evaluating a biological system is that of metabolomics, the global measurement of the suite of small molecule metabolites that constitute an organism's metabolome. The metabolome is made up of numerous small molecules that are derived from or utilized by all known metabolic pathways. Metabolomics provides insight into an organism's physiological state (i.e., phenotype) and, thus, can serve as a quantitative, global measurement to supplement other qualitative approaches, such as the BCS system.[99, 100] Investigating the metabolic profile of emaciated equids could provide information as to which metabolic pathways are affected during a state of malnutrition.[101]

At the present time, little research has been conducted in the field of equine metabolomics regarding nutritional rehabilitation. Current equine studies mainly focused on healthy thoroughbreds, pregnant mares, exercise, and doping.[102-105] Metabolomics research conducted in malnourished pigs and humans with cachexia can serve as a foundational comparison for emaciated equids, but species-specific knowledge through dietary intervention periods is warranted.[101, 106, 107] Despite the vast array of information available pertaining to the increasingly popular field of metabolomics, no studies are dedicated to the malnourished horse or the refeeding and rehabilitation process over the nutritional recovery period. Research pertaining to the equine metabolome throughout stages of malnutrition and the refeeding process could provide insight into specific nutritional requirements and allow owners to make dietary adjustments accordingly. Thus, this study focused on evaluating the metabolome of various malnourished horses during the refeeding process to determine metabolic differences between the starved and rehabilitated horse during the refeeding process.

4.3 Results and discussion

4.3.1 ***Refeeding outcomes of equine with unknown origin and source***

Originally, ten equids with a BCS of 2 or less were enrolled into the project; however, due to health circumstances, four horses were not able to complete the refeeding process. Specifically, the following situations occurred for each horse removed from the project (termed "Did not complete" in **Table 4.1**): 1) impaction colic resulting in euthanasia on Day 6 of the CCP; 2) positive respiratory swab for Equine Herpes Virus 1, wild type (EHV-1), *Streptococcus equi*, and influenza type A virus, resulting in euthanasia on Day 8 of the CCP; 3) positive respiratory swab for EHV-1, resulting in euthanasia on Day 1 within the RP; and 4) positive respiratory swab for influenza virus type A resulting in subsequent pneumonia, and due to lack of body weight gain was disenrolled on Day 73 of the RP. The remaining six horses (C diet $n = 3$ and S diet $n = 3$) were refed successfully to either a BCS

Table 4.1. Outcomes for equine enrolled in the refeeding program.

Subject Identifier	**Program Outcome**	**Samples taken**	
		CCP	**RP**
A	Did not complete	5	NA
A2	Did not complete	7	NA
B	Did not complete	7	NA
C	Completed	7	4
D	Did not complete	7	1
E	Completed	7	4
F	Completed	7	3
G	Completed	7	3

of 3.5 or 4 (termed "Completed" in **Table 4.1**). Initial weight at enrollment was 368 ± 58 kg (mean ± standard deviation; n = 10) and final weight after refeeding was 426 ± 54 kg (n = 6). Of the six horses that completed the project, the entire refeeding process from enrollment to successful disenrollment lasted 129 ± 28 days.

Large animal nutrition studies create unique opportunities and challenges due to management, availability, and cost for such trials. Within our study, emaciated animal availability that met the enrollment criteria were difficult to source during the recruitment period. Extensive respiratory disease was prevalent in many potential animals that met the desired BCS (1 or 2). During the enrollment process an additional 12 horses were assessed for respiratory disease and all were positive EHV-1. Given the risk of transmission and morbidity rate for infectious respiratory diseases, alongside physiologic changes present during starvation, the pool of horses available to utilize for the project was limited.[108]

Despite low sample numbers, power analysis prior to study approval and commencement indicated that animal numbers utilized in this study are adequate to detect statistical significance between treatment groups. Additionally, equine nutrition studies utilizing low animal numbers have been successfully completed and contribute meaningful information to the existing literature to advance clinical and management level decisions.[109-111]

It is important to note that the backgrounds and histories of the horses enrolled in this study were largely unknown due to the variance in origin and ownership of the equine subjects. For this reason, it was not possible to consider factors that may influence the metabolome, such as diet history and the presence of past or current parasites, comorbidities, and disease. Perhaps these factors should not be considered as no two subjects will present with identical histories and such diversity contributes to a better overall understanding of rehabilitating emaciated horses. Despite these unknown variables, statistical analyses conducted on the refeeding process indicate a distinct difference between the equine metabolome during the CCP vs. the RP. This study

supports the necessity of the refeeding process for the malnourished horse via blood chemistry and metabolomics analyses, despite its history and individual attributes.

*4.3.2 **Blood chemistry analysis suggests improved biological function during the RP***

Box plots were created to display differences in blood chemistry analyte levels between the CCP and RP (**Figure 4.1**). Results indicated statistical significance in analytes present in blood plasma samples (**Appendix Table 4.5**). LDH, ALB, AST, and CREAT levels were all statistically increased during the RP compared to the CCP. Evaluation of blood serum corroborated a significant change in LDH, ALB, and CREAT (**Appendix**

Figure 4.6). Non-esterified fatty acids (NEFA) were also shown to significantly decrease in serum during the RP. Statistical differences were also detected when comparing diet, sex, and age group in blood plasma and serum samples (**Appendix Table 4.6**). Albumin, a family of proteins primarily synthesized by the liver, was detected at lower levels during the CCP compared to the RP.[112] Low albumin levels in equine were previously thought to be associated with liver disease and/or liver failure, but a retrospective study of literature data concluded that consistently low albumin levels (hypoalbuminemia) reported were not directly associated with severe liver disease.[112] This finding does not dismiss the possibility that low albumin levels can be associated with improper hepatic function due to insufficient biological resources, such as those unobtainable during starvation.

Creatinine, a small molecule prominently present in plasma, was significantly altered between the CCP vs. RP. This nitrogenous molecule used to evaluate renal function and overall muscle mass was found to be lower during the CCP than that of the RP.[113-115] This compound is consistently produced in equine as a function of their muscle mass and body weight, dependent on proper renal function.[114] This finding directly correlates to increasing BCS scores during the refeeding process; as the malnourished horse undergoes the refeeding process and their BCS score increases, a positive correlation with increasing creatinine levels is observed, most likely due to a gain in muscle mass and body weight.

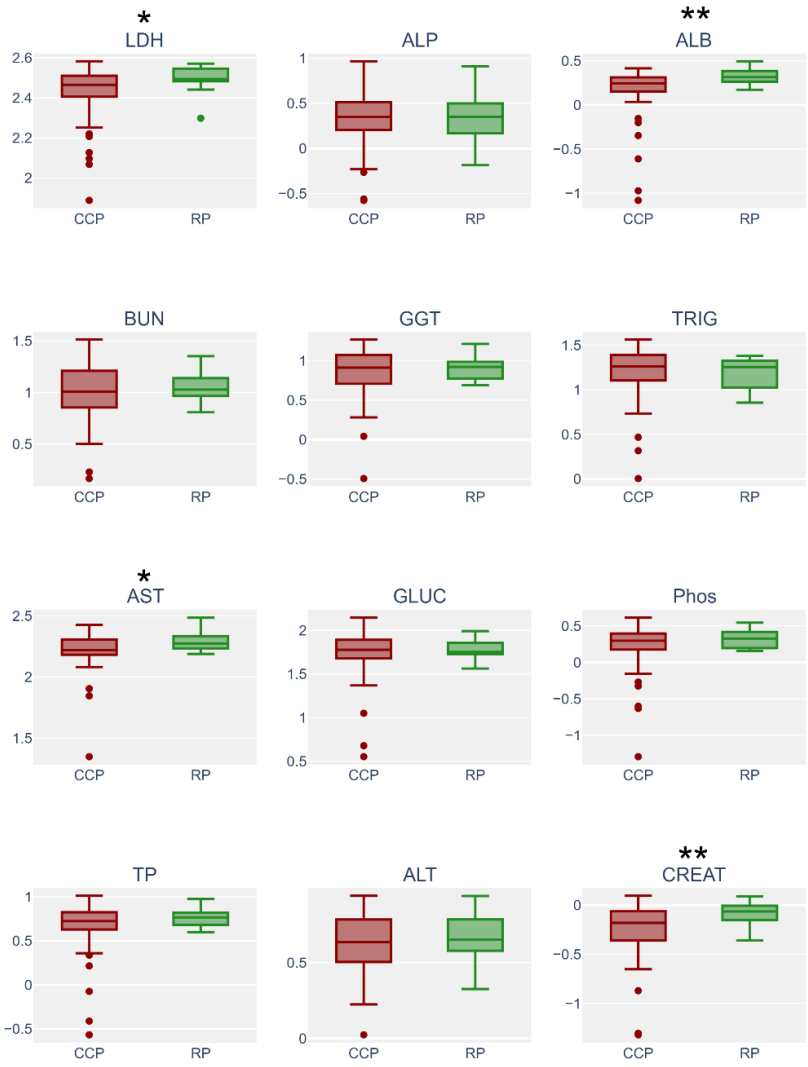

Figure 4.1. Box plots of blood plasma data conveying the differences between blood during the CCP (n = 68) and the RP (n = 15). Asterisks represent statistical significance (p value ≤ 0.1 = *; p value ≤ 0.05 = **). LDH: lactate dehydrogenase (p value 0.06), U/L; ALP: alkaline phosphatase, U/L; ALB: albumin (p value 0.04), g/dL; BUN: blood urea nitrogen, mg/dL; GGT: gamma-glutamyl transferase, U/L; mg/dL; TRIG: triglycerides, mg/dL; AST: aspartate amino transferase (p value 0.09), U/L; TP: total protein, g/dL; GLUC: glucose, mg/dL; Phos: phosphate, mg/dL; ALT: alanine transaminase, U/L; CREAT: creatinine (p value 0.04).

Lactate dehydrogenase and aspartate aminotransferase are two enzymes that serve essential roles in anaerobic and aerobic metabolic pathways, respectively, with important emphasis in hepatic, renal, and skeletal muscular metabolism.[116, 117] Interestingly, these enzymes serve as non-specific, clinical biomarkers of disease as their high-level presence is associated with cellular death.[116, 117] In the present study, levels of these enzymes were statistically higher in equine during the RP than the CCP, which was an unanticipated observation as horses are not likely to experience as much cellular death during the RP compared to the CCP. Interestingly, increased levels of lactate dehydrogenase and aspartate aminotransferase have also been observed in a Japanese breed of equine that was fed a roughage-based diet; it was theorized that these enzymes were primarily higher due to diet.[118] Despite statistical increases observed in the present study, the average levels of these enzymes were within reference ranges for equine in both the CCP and RP, suggesting an increase not necessarily indicative of disease.[119]

Blood chemistry panels are an efficient way to measure overall health and function of major organs, such as the liver and kidneys. However, these panels are limited in the amount of information attainable due to the sensitivity of methods and instrumentation. This problem of sensitivity is solved when characterizing blood (i.e., plasma) via metabolomics methods, which provide a vast array of quantitative information on the complexities of numerous metabolic pathways. Though metabolomics methods only measure small molecules (unlike blood chemistries which can detect small molecules, proteins, and enzymes), the variety of metabolites detected and low concentrations at which these compounds can be measured provide more global information on the metabolic processes, without the need for separate protein or enzyme analysis. Therefore, blood chemistries were used herein as a supplement to the more globally informative metabolomics analysis.

4.3.3 ***Potentially toxic metabolites and indicators of oxidative stress were in lower abundance during the RP***

Fold changes (i.e., comparisons of metabolite abundance between sample types) were calculated for metabolites present in blood plasma. Of the metabolites detected,

those classified as amino acids (amino acids, precursors, derivatives, and metabolism byproducts) showed the most perturbations (**Figure 4.2**). Overall, amino acid related metabolites such as glutamine, methionine, phenylalanine, alanine/sarcosine, and creatine showed statistically significant decreases during the RP compared to the CCP; however, *N*-acetylornithine showed a significant increase in abundance during the RP. Additionally, metabolites such as uridine, allantoin, and uric acid showed significant decreases. With the exception of *N*-acetylornithine, metabolites showing significant fold changes exhibited an overall decreased abundance during the RP compared to the CCP (**Appendix Table 4.7**).

Fold change analysis of metabolites detected during the RP compared to the CCP showed perturbations in metabolites with varying biological activity (Error! Reference source not found.). It is important to note that fold change analyses of global metabolomics data may show increases or decreases in overall abundance but cannot discern the ultimate metabolic fate of a particular metabolite. For example, if a metabolite is found in higher abundance, it is possible that this compound is produced by the biological system at a higher rate, resulting in higher abundance; alternatively, this compound may be utilized by the system at a lower rate that also results in a higher concentration. To determine which of these scenarios is actually occurring, studies utilizing stable-isotope labeled metabolite tracers would be required to measure the fluxes of the metabolites of interest and ascertain the activity of pathways utilizing these molecules.[120] Nonetheless, one can often infer whether metabolites are being actively metabolized by looking at changes in several or all molecules in pathways in the context of the system state instead of analyzing data for individual molecules.

During the study, it was observed that metabolites shown to exhibit toxicity when found in high concentrations were found in lower abundance during the RP. In particular, allantoin, phenylalanine, and methionine were found to be significantly decreased in horses with higher BCS scores. Allantoin and methionine are both small molecules that are often considered indicators of oxidative stress, a condition marked by increased levels of free radical species that is often associated with disease and impaired nutritional

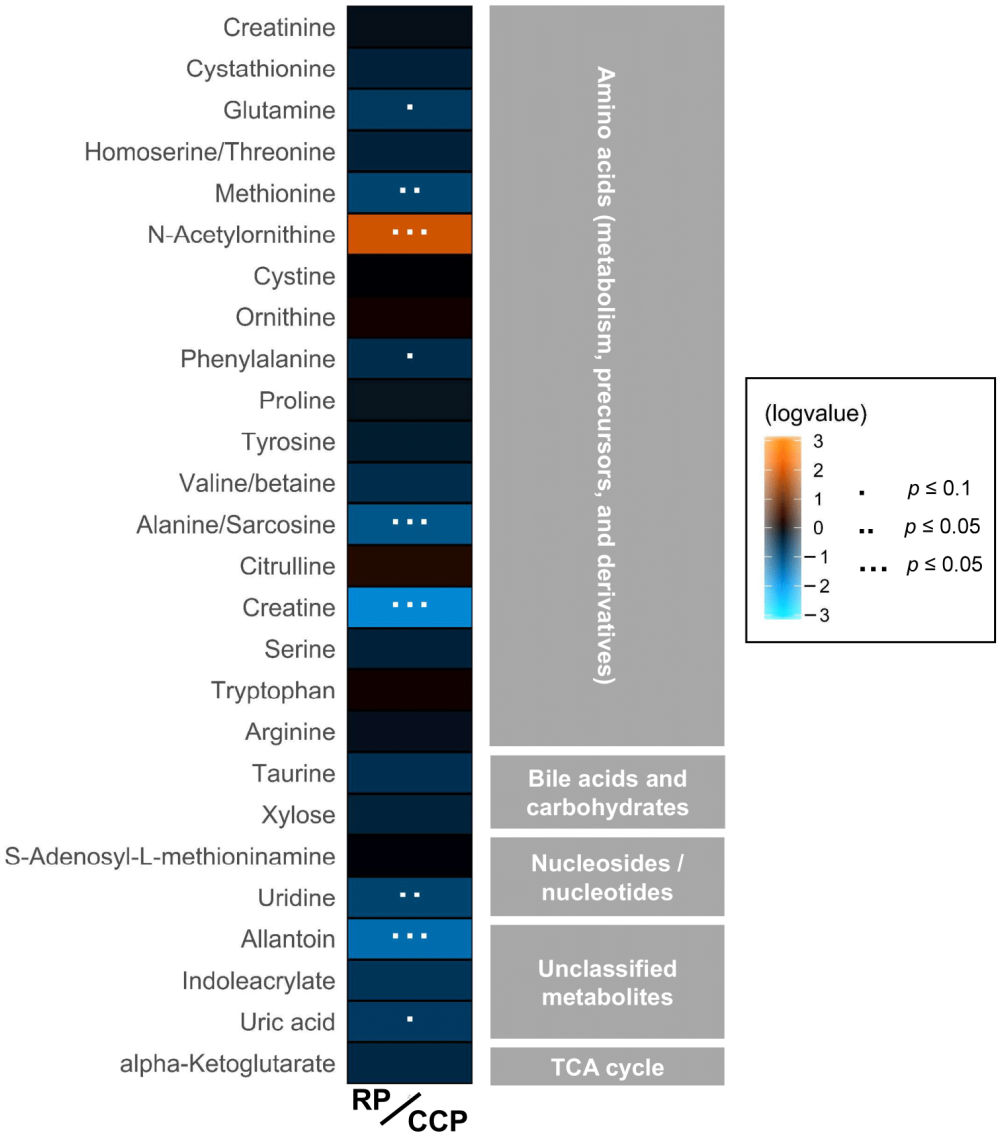

Figure 4.2. Heatmap showing increased or decreased abundance of detected metabolites organized by compound class between the RP (n = 20) and the CCP (n = 68; fold change of RP/CCP). Eight compounds exhibited significantly lower abundance while one compound showed significantly higher abundance during the RP.

status.[121] Specifically, methionine has been observed to be enhanced in subjects with severe acute malnutrition.[121-124] Because these potential biomarkers were found in lower abundance during the RP, it is theorized that the equine subjects are likely experiencing less oxidative stress due to these compounds acting as a defense against free radical species or their production at lower rates as their biological need to dissolve the radical species is lessened.

Similarly, phenylalanine appeared in higher abundance in equine during the CCP. Despite phenylalanine's proteinogenic properties, it serves as a toxic metabolite when found at chronically high concentrations. As this compound is an essential amino acid, an overall reduction in this compound's abundance during the RP may indicate an increase in health as this amino acid is potentially shunted to upregulate protein synthesis.

4.3.4 ***Metabolites regulated by skeletal muscle were altered between the CCP and RP***

Creatine was found to be significantly higher in abundance during the CCP. This finding supports a similar study conducted in juvenile pigs, which revealed that creatine levels were more abundant during a state of malnourishment.[101] This finding could be accredited to muscle wasting, a process in which muscle is broken down to be utilized for energy.[125] It is theorized that muscle wasting may cause the release of creatine from the muscle cells into circulation, yielding higher plasma creatine levels in horses with lower body condition scores. It has been observed that creatine supplementation does not significantly increase plasma creatine level, furthering the notion that increased plasma creatine abundance in horses during the CCP is due to muscle wasting.[126] As previously mentioned, methionine (a catalytic precursor of creatine) was also found in lower abundance in horses during the RP.

Glutamine is an important non-essential amino acid highly expressed in skeletal muscle, similar to that of creatine. Approximately 90% of all glutamine synthesized is via skeletal muscle; it is then transferred to the blood, where it represents the most abundant free amino acid.[124] Interestingly, this amino acid was present in lower abundance during the RP. Low levels of glutamine are often associated with disease, as consistent levels are required for proper function of many metabolic processes and organs (brain, lungs, gut,

immune system, skeletal muscle, kidney, etc.). With this information and the observation that other toxic metabolites appear to decrease during the RP, it is more likely that glutamine levels are decreased in equine with higher BCS's due to high utilization by the system for other biological processes.

In addition to creatine, two metabolites commonly associated with skeletal muscle (alanine and sarcosine) were detected. The methods of detection utilized in this study were unable to differentiate these two isomeric compounds, yet a notable feature was detected either representing the isomers together or separately. In the event this feature is significantly changed due to a decrease in sarcosine (a product of creatine), a simple explanation of decreased abundance of precursors during the RP may be offered. Though, an alternative hypothesis is that muscle wasting and oxidative stress were overall less prevalent during the RP, resulting in decreased sarcosine abundance. Regardless, this cascade of metabolites was important to the discernment of the CCP and RPs. However, the metabolic feature associated with this finding is more likely due to the presence of alanine, as this amino acid is one of the more highly abundant amino acids found in plasma and is known to be found in higher concentrations than sarcosine.[127, 128] There are many theories as to why alanine was present in higher abundance during the CCP (including muscle wasting), but perhaps the most compelling is that of the shift in energy metabolism during starvation coordinated by metabolic crosstalk between skeletal muscle and the liver.[129] Gluconeogenesis, glycogenolysis, glycolysis, and protein break-down all retain the common factor alanine transaminase, an enzyme that produces ala-nine partly to prevent skeletal muscle from accumulating toxic nitrogenous products and to produce hepatic glucose.[129] Thus, this offers an alternative to glucose homeostasis and energy metabolism.[129] Alanine levels have also been observed to increase in equine during and after exercise (i.e., when energy requirements change), which may mimic that of starvation.[127] Perhaps alanine was observed in greater abundance during the CCP due to high production amounts to satisfy the need of energy metabolism via hepatic pathways; yet, additional metabolites detected in this study provide evidence that hepatic function may be compromised, resulting in a build-up of this alternative energy product.

4.3.5 ***Significant differences were observed in metabolites related to liver and kidney function during the CCP and RPs***

During the RP, uric acid, allantoin, and uridine were found in lower abundance while *N*-acetylornithine was found to be significantly increased. Uric acid is a purine derivative synthesized in the liver and, in excess amounts, is converted to allantoin, which is then filtered and excreted by the kidneys.[130] In mammals, allantoin reflects an end-point of purine metabolism, unless it is shunted through the glyoxylate or glycine, serine, and threonine metabolism pathways.[131-133] The observation of altered levels of allantoin could be attributed to kidney function; starved, malnourished horses may experience kidney disfunction due to a lack of nutrients and resources, which prevent the ability of the kidneys to filter allantoin from the body. However, because uric acid is a precursor to allantoin and is not utilized in other metabolic processes (other than bile secretion), decreased levels of this compound indicate that it is being produced at a lower rate, yielding a lower rate of allantoin production.[131-133] Perhaps this is due to a lessened biological need for purine degradation, as these molecules are being directed to other pathways and are not present in excess.

Like uric acid and allantoin, uridine, a pyrimidine nucleotide important to RNA synthesis, is synthesized in the liver and excreted by the kidneys, if not catabolized.[134] Similar hypotheses exist for uridine as uric acid and allantoin. Lower levels are possibly detected during the RP as RNA is synthesized at a higher rate (i.e., less excess pyrimidine), which may indicate an increase in liver function. Yet, it's also likely that uridine is better excreted by the kidneys during this phase, resulting in lower plasma levels.

The only metabolite found to be in higher abundance during the RP was that of *N*-acetylornithine, a small molecule involved in the biosynthesis of amino acids and a precursor to the urea cycle during arginine biosynthesis.[131-133] Endogenous arginine synthesis and the urea cycle primarily occur in the kidneys.[135] Because *N*-acetylornithine was the only significantly altered metabolite involved in this cascade (arginine, citrulline, and ornithine fold changes were not statistically different), increased production and

subsequent utilization in the cycle is less likely than a build-up due to non-use. Isomers of *N*-acetylornithine have been detected in high concentrations in various food sources, such as wheats and some fruits and vegetables. Thus, it is more likely that horses with higher BCSs that have undergone the refeeding process accumulate higher levels of *N*-acetylornithine in plasma from their diet.

4.3.6 The plasma metabolome illuminates differences in equine subject-specific attributes

Partial least squares – discriminant analyses (PLS-DAs) allow complex data (i.e., metabolomics data) to be reduced to a simple three-dimensional scores plot, which clusters data based on variability between the samples.[136] Using these plots, one can generate hypotheses as to potential differences in metabolomic profiles between groupings, as well as investigate the metabolites that drive those differences. A PLS-DA was performed on the metabolomics data (known metabolites and unidentified features) to investigate potential differences in metabolomic profiles between equine in the CCP vs. the RP. Comparison of features unique to these groups resulted in a clear separation (**Figure 4.3**). As the known metabolites represent only a small portion of the data presented here, unidentified features were included in this analysis as these features provide insight into metabolic processes that have not yet been well described and contribute to a global view of all characteristic data points in a sample, serving as an important component of metabolic pro-file. Data from these analyses, combined with statistical fold change analysis, suggest that differences in the metabolome can be observed for equine subjects in the CCP vs. those in the RP undergoing the refeeding process.

Metabolic profiles (including known metabolites and unidentified features) were compared using the variety of metadata provided within the study: diet (C vs. S), sex (mare vs. gelding), and age group (below 20 years old vs. 20 years old and above). Analysis on breed specifications were not conducted due to low replicates (e.g., only one equine subject was of the Standardbred breed). PLS-DAs comparing diet, sex, and age group showed distinct groupings (**Figure 4.4**). Features were evaluated using a t-test and

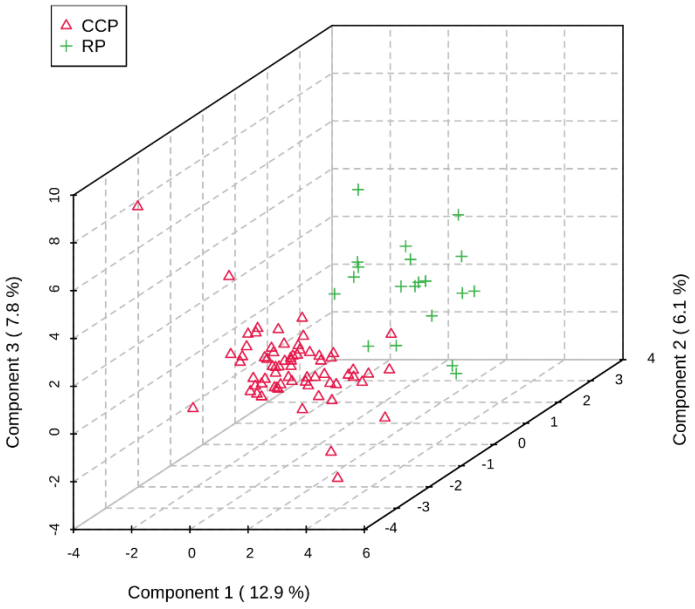

Figure 4.3. PLS-DA containing known metabolites and unidentified features detected during the CCP (n = 68) and RP (n = 20). The resulting plot shows separation between the groupings, indicating differences in the equine metabolomic profile during the CCP and the RP.

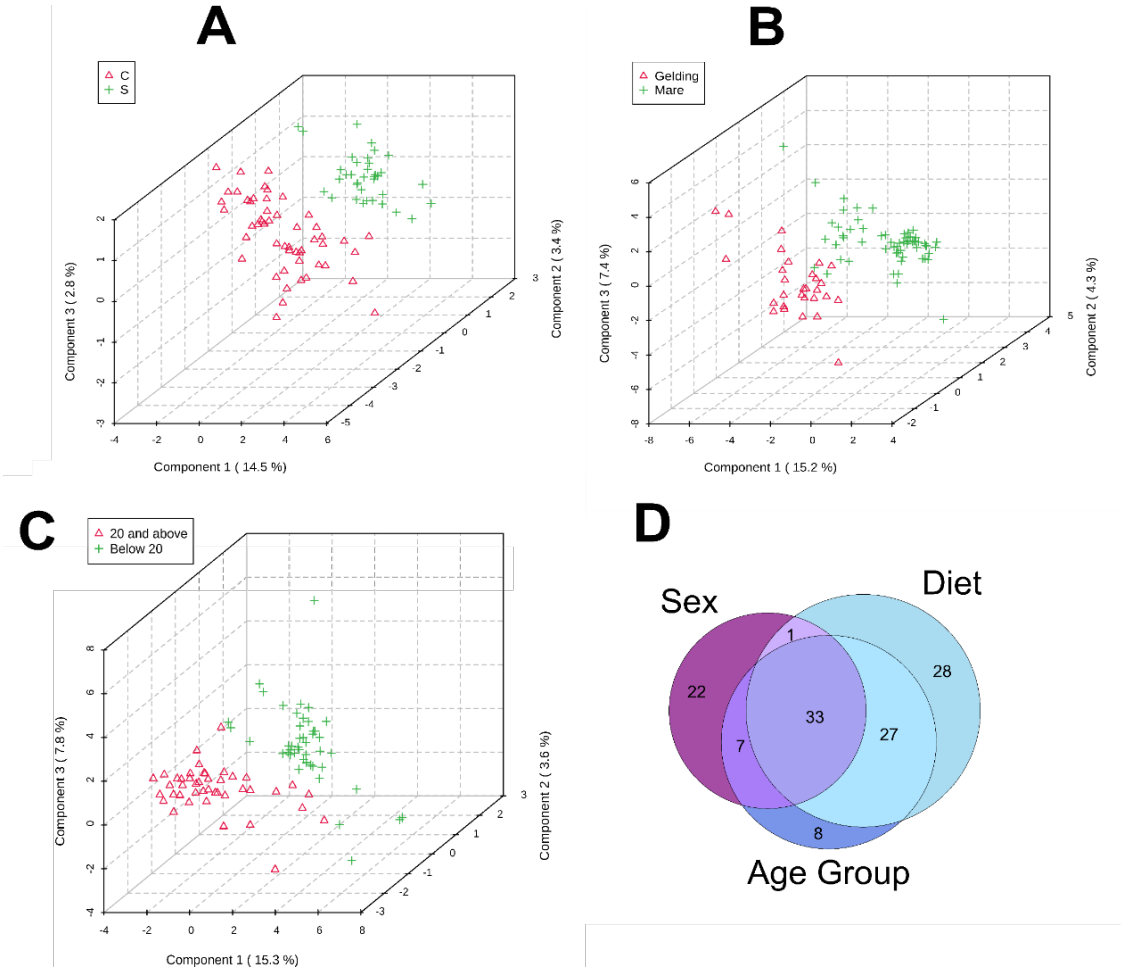

Figure 4.4. PLS-DAs of known metabolites and unidentified features detected in the metabolomes of all horses that were enrolled in the refeeding program grouped by A) diet (C vs. S), B) sex (mare vs. gelding), and C) age group (below 20 and 20 and above). Sample sizes used for PLS-DAs were as follows C: $n = 52$; S: $n = 36$; mare: $n = 59$; gelding: $n = 29$; below 20: $n = 45$; 20 and above: $n = 43$. Venn Diagram (D) displaying similarities and differences between features in each grouping.

yielded 127, 157, and 40 statistically significant compounds (p value ≤ 0.1) for diet, sex, and age comparisons, respectively (**Appendix Table 4.8**, **Appendix Table 4.9**, and **Appendix Table 4.10**).

Statistically significant differences between specific metabolites and metabolic pro-files were observed between the CCP and RP for ten equine subjects of various sex, age, breed, and origin. Differences were evident between designated diet, mares and geldings, as well as age group (below 20 years old and above 20 years old); yet, these differences were not evident in the analysis of the CCP vs. RP (e.g., sex-specific clusters were not evident in the CCP vs. RP discriminant analysis), indicating that these subject-specific attributes did not affect the conclusion that the metabolomic profiles of horses undergoing the refeeding process were statistically different.

As diet played an essential role in the current study, an analysis to determine potential differences in metabolomic profiles in equine assigned to a particular diet was conducted. Various statistical analyses suggest perturbations in metabolism with respect to diet. In the event of a negative energy balance (e.g., in the case of malnourishment), particular care is placed on diet such that the subject can consume and digest nutrients without inducing refeeding syndrome or overfeeding (i.e., the process of introducing nutrients in excess such that metabolic homeostasis cannot be maintained.[135] Over-feeding may result in further metabolic damage, particularly in the liver and kidneys, both major organs which have shown to be impaired during the CCP in the current study. Thus, diets for malnourished equine must be carefully tailored to slowly reintroduce nutrients in a manner such that further metabolic damage is not inflicted. Though an in-depth analysis of the effects of a particular diet or set of nutrients on equine outcome was not within the scope of this study, it is worth noting the differences observed in the global metabolome in this study; further investigation is required to determine the detailed effects of diet and nutrients that cause this separation.

With advances in equine feed that cater to aging horses, the average lifespan of the equid is increasing, which has prompted a surge in research devoted to older horses (i.e., horses 20 years old and above).[137] For this reason, an analysis to evaluate the

metabolome of younger vs. older horses in the present study was conducted and resulted in clear differences between the two groups. The amount of metabolites that drove this distinction was not as prominent as other comparisons (i.e., diet and sex), though various statistical tests support perturbations based on age group. It is theorized that many metabolic factors may play a role in this age-based separation, including alterations in muscle fiber type and renal function.[137] Similar to effects from diet, further studies are warranted to establish clear relationships between the aging horse and metabolism.

It is important to note that the analysis of the metabolome provides a biochemical snapshot of the metabolic state for the system, which is highly complex. For this reason, it is not surprising that attributes such as diet, sex, and age affect metabolic profiles. Moreover, these attributes contribute diversity to the study of the impacts of refeeding to gain a better understanding of caring for malnourished equine.

4.3.7 ***The equine lipidome during the CCP indicates oxidative stress and organ failure***

Lipid profiles in mammals, especially young children, have shown to be remarkable indicators of malnutrition.[138, 139] Because serum NEFA levels were elevated during the CCP, it was suspected that, even in plasma, perturbations would be observed in other lipid classes as an indicator of emaciation. Pooled samples of the CCP and RP were subjected to lipidomic analysis and results include both known lipids (via fragmentation matching) as well as unidentified lipid features.

A PLS-DA of the lipid profiles between the CCP and RP indicates the lipidome of each group is significantly different (**Figure 4.5A**). Additionally, a volcano plot illustrates that 94 features were statistically upregulated (or more abundant) in the CCP and 51 features were significantly more abundant in the RP (**Figure 4.5B**). Upon evaluation of these significant features, it is clear that more unidentified lipid features were present in the CCP while many known lipids (i.e., phospholipids and lysophosopholipids) were important in the RP (**Appendix Table 4.11**). Although blood chemistry analyses did not find TRIG (or TG) plasma levels to be statistically different,

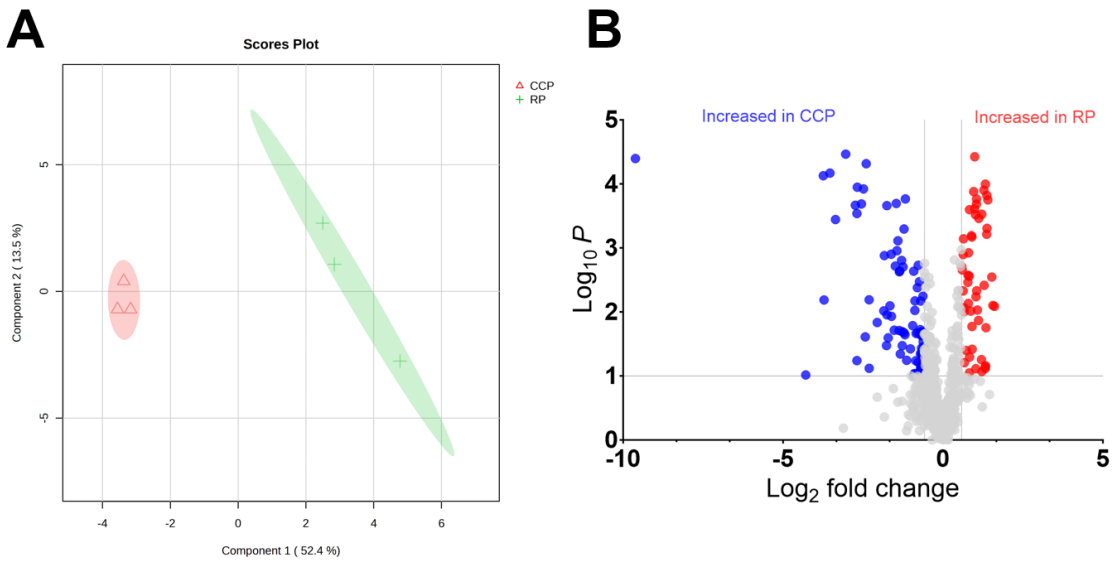

Figure 4.5. A) PLS-DA and B) volcano plot illustrating significant differences in lipidome profile between CCP and RP.

lipidomics data revealed that this lipid class, along with ether phosphatidyl choline (PC-O) lipids, were important drivers in the difference between the CCP and RP lipidomes. Higher levels of TRIGs are often indicators of metabolic disorders due to obesity, but may also be linked to pancreatitis and organ failure.[140] Ether lipids, including PC-Os, function as antioxidants; their increased prevalence during the CCP indicates that the equine was undergoing oxidative stress, further supporting metabolomics data.[141] It was expected that equine in the CCP would exhibit signs of lipid peroxidation due to oxidative stress, though, no oxidized lipids were detected in either group. Regardless, the large number of unidentified lipids in the CCP compared to the RP is peculiar and suggests that these features may be lipid-like products of oxidative stress that cannot be matched to databases as they have not yet been annotated and/or characterized.

4.4 Conclusions

Comparison of the equine metabolome during a state of malnourishment versus rehabilitation illuminated significant differences that provide essential biological insight to the process of refeeding the emaciated horse. After commencement of the refeeding process (i.e., during the RP), a decrease in potentially toxic metabolites was observed, metabolic alterations suggesting increased liver and kidney function were shown, and metabolite changes related to muscle gain/repair and changing energy demands were evident. Blood chemistry panels also showed statistical differences between analyte abundance between the CCP (i.e., state of malnourishment) and the RP, further indicating improper liver and kidney function during the CCP. The combination of blood chemistry and metabolomics analyses on the equine subjects in this study provided essential insight to the biological processes that are influenced when rehabilitating the malnourished horse. Despite differences observed between the metabolome with respect to subject-specific attributes (i.e., diet, sex, and age group), a clear discernment between the metabolome unique to the CCP and RP were observed, providing evidence that the refeeding process has a profound impact on equine rehabilitation.

4.5 Experimental section

4.5.1 ***Equine enrollment***

Ten light breed horses aged 19 ± 3 years were enrolled into the study over a three-month period (**Table 4.2**). Horses for the study were obtained from three outlets: (1) in cooperation with the Tennessee Department of Agriculture (TDA) and the Tennessee State Veterinarian by owner surrender as a result of neglect cases, (2) purchased from public auction, and (3) private owner surrender. Enrollment criteria included: (1) BCS of 2 or less[99], (2) light breed mares or geldings, and (3) apparent good health, aside from malnourishment, as defined by temperature, pulse and respiration rates within normal limits, and no evidence of coughing or nasal discharge at the time of enrollment. Due to the nature of horse acquisition and enrollment, previous diet history on each horse could not be acquired. All study procedures were approved by the University of Tennessee Institutional Animal Care and Use Committee (Protocol #2811-1220).

4.5.2 ***Study timeline and sample collection***

The first ten days of the study were labeled as the critical care period (CCP). During this period, horses were housed and maintained at the University of Tennessee College of Veterinary Medicine (UTCVM; Knoxville, TN, USA) where their initial health status was evaluated by a veterinarian and a Coggins test was performed. Blood samples were collected from the jugular vein on the day of intake and every other day thereafter. Weekly, horses' BCS were assessed by two individual, trained reviewers.[94] Vital signs including temperature, pulse, respiration, capillary refill time, and skin tent were assessed every 12 hours during the CCP to monitor horses for disease onset and overall health status in compliance with UTCVM policy. If horses displayed signs of potential infection, a respiratory swab was performed to check for Equine Herpes Virus (EHV), Strangles, and Influenza. If horses tested positive for any of these diseases, attending veterinarians worked in conjunction to provide care and treatment while maintaining refeeding protocols. Body weight (BW) was assessed daily using a

Table 4.2. Available metadata for equine subjects enrolled in the refeeding program.

Subject Identifier	**Sex**	**Breed**	**Approximate Age (Years)**
A	Mare	Quarter Horse	19
A2	Mare	Tennessee Walking Horse	22
B	Mare	Appendix	20
C	Mare	Quarter Horse	20
D	Mare	Tennessee Walking Horse	20
E	Mare	Quarter Horse/Arabian	18
F	Gelding	Appendix	16
G	Gelding	Appendix	23
H	Mare	Standardbred	15

commercially available equine scale (Optima, Rancho Cucamonga, CA, USA).

The remainder of the study duration (days 10–165) was designated as the recovery period (RP). During the RP, horses were housed and maintained at either UTCVM, the University of Tennessee Veterinary Research and Education Center (VREC; Knoxville, TN, USA), or at Middle Tennessee Research and Education Center (MTREC; Spring Hill, TN, USA), based on housing availability. Horses were always moved as a cohort, and at least six days of acclimatization was allowed before the next sampling period. Before transportation, all horses tested negative for infectious diseases.

Weekly BW measurements were taken throughout the duration of the study. Every two weeks, BCS was evaluated by two independent trained reviewers for each horse and jugular venipuncture blood samples were collected at each BCS increase. Fecal samples and respective fecal float and centrifugation tests were performed on Day 14 and horses were dewormed based on fecal test results. Horses were determined to progress to the next BCS when all reviewers agreed that the next BCS was reached, and a weight gain of 16–20 kg from the previous BCS was achieved.[142, 143] If horses reached a BCS of 4 before the end of the rehabilitation period, final measurements and samples were taken prior to study disenrollment. Plasma blood samples were maintained on ice until centrifugation at 3000× g for 10 min. Serum blood samples were allowed to clot overnight and then centrifuged at the same speed and duration. All aliquots were stored at −80 °C until analysis.

*4.5.3 **Diet formulation***

Upon enrollment, each horse was randomly assigned one of two diet groups for the duration of the study: control (C) diet which consisted of timothy hay and a commercially available vitamin mineral product (Purina Free Balance) where diets were formulated to meet DE requirements from forage alone; and senior (S) diet, in which 50% of DE requirements were provided from a commercially available complete feed, and the remaining 50% provided by timothy hay (**Table 4.3**). Diets were formulated to be isocaloric and meet daily National Research Council (NRC) nutrient requirements for mature horses weighing under 600 kg.

Table 4.3. Nutrient analysis of forage of diet components

Nutrient	**Timothy Hay**	**Equine Senior**	**Free Balance Mineral**
Digestible Energy (mCal/kg)	1.95	2.7	0
Protein (%)	9.88	15.5	1.55
Lysine (%)	0.34	0.7	N/A
Fat (%)	1.29	6.2	0.1
Acid Detergent Fiber (%)	39.50	22.54	N/A
Neutral Detergent Fiber (%)	62.23	38.89	N/A
Calcium (%)	0.21	0.77	13.52
Phosphate (%)	0.27	0.55	12.66
Potassium (%)	2.39	1.6	0.66

The refeeding diet protocol was established based on previously published methods.[96, 144] During the CCP, from day of intake until Day 3, horses were fed 50% of daily digestible energy (DE) requirements split into six feedings. On Days 4 and 5, feeding amount increased to provide 75% of daily DE requirement over six feedings. On Days 6 to 10, horses were fed 100% of daily DE requirement over three different feedings.

Diets were formulated to provide adequate DE for 0.45 kg of BW gain per day. Initially, DE was increased to 125% of daily DE requirements based on weekly BW measurements. If horses did not gain weight at an appropriate rate for two consecutive BW measurements, DE was increased by 10%, to 135 or 145%, respectively.

*4.5.4 **Blood chemistry analysis***

Plasma and serum chemistry quantitative values (**Table 4.4**) were determined via photometric absorbance values utilizing a COBAS C311 analyzer under guidelines determined by the manufacturer and utilizing approved reagent and standards (Roche, Switzerland).

*4.5.5 **Metabolomics extractions***

The metabolomics extraction procedure was adapted from Rabinowitz and Kimball.[87] Briefly, 100 µL of plasma was mixed with 1.3 mL of chilled extraction solvent (4:4:2 acetonitrile:methanol:water with 0.1% formic acid) in an Eppendorf tube and allowed to extract for 20 min at −20 °C. Samples were centrifuged and the supernatant was pooled into a separate glass vial. To the solution remaining in the Eppendorf tube, 200 µL of ex-traction solvent was added, the mixture was vortexed, and allowed to extract for 20 min at −20 °C. Samples were then centrifuged, and the supernatant was pooled into the glass vial with the supernatant from the first extraction. Pooled samples were dried under nitrogen and resuspended in 300 µL of water prior to mass spectrometric analysis.

Table 4.4. Measured parameters for blood plasma and serum

Analyte	**Abbreviation**	**Units**	**Matrix**
Lactate dehydrogenase	LDH	U/L	Plasma/serum
Alkaline phosphatase	ALP	U/L	Plasma/serum
Albumin	ALB	g/dL	Plasma/serum
Blood urea nitrogen	BUN	mg/dL	Plasma/serum
Gamma-glutamyl transferase	GGT	U/L	Plasma/serum
Aspartate amino transferase	AST	U/L	Plasma/serum
Glucose	GLUC	mg/dL	Plasma/serum
Phosphate	PHOS	mg/dL	Plasma/serum
Total protein	TP	g/dL	Plasma/serum
Alanine transaminase	ALT	U/L	Plasma/serum
Creatinine	CREAT	mg/dL	Plasma/serum
Triglycerides	TRIG	mg/dL	Plasma/serum
Creatine kinase	CK	U/L	Serum only
Non-esterified fatty acids	NEFA	mEq/L	Serum only
Serum calcium	SCA	mg/dL	Serum only

*4.5.6 **Ultrahigh performance liquid chromatography mass spectrometry high resolution mass spectrometry (UHPLC-HRMS)***

The metabolomics analyses were conducted at the Biological and Small Molecule Mass Spectrometry Core at the University of Tennessee Knoxville (Knoxville, TN, USA). The sample extractions, chromatographic separations, and mass spectral analyses were performed according to an established method using UHPLC-HRMS.[145] The collected metabolomes were stored at 4 °C in an UltiMate 3000 RS autosampler (Dionex, Sunnyvale, CA, USA) until analyses were performed. All chromatographic solvents used were HPLC grade (Fisher Scientific, Hampton, NH, USA). Reverse phase separations were carried out using a Synergi 2.6 µm Hydro RP column (100 mm × 2.1 mm, 100 Å; Phenomenex, Torrance, CA, USA) and an UltiMate 3000 pump (Dionex, Sunnyvale, CA, USA). The chromatography utilized a 25-minute binary gradient elution using a 97:3 water:methanol mixture with added 10mM tributylamine and 15 mM acetic acid (mobile phase A) and 100% methanol (mobile phase B). The flow was set to 0.200 mL/min, and the gradient was as follows: 20% B at 5 min, 55% B at 13 min, 95% B at 15.5 min, 0% B from 19 to 25 min. The separated metabolites were ionized via negative mode electrospray ionization prior to analysis on an Exactive Plus Orbitrap MS (Thermo Scientific, San Jose, CA, USA). The resolution of the mass spectrometer was set to 140,000 with an automatic gain control setting of 5 × 105 and injection time of 100 milliseconds. The sheath, auxiliary, and sweep gases were set to 25, 8, and 3 arbitrary units, the spray voltage was 3.5 kV, and the capillary temperature was 320 °C.

*4.5.7 **Data analysis***

Descriptive statistics for refeeding parameters were assessed using STATA SE (ver-sion 16.1, StataCorp, College Station, TX, USA).

To evaluate the known metabolites, raw data collected by the instrument were converted to .mzML files via MSConvert (ProteoWizard). Features were then picked using an in-house library in EL-MAVEN based on exact mass (5 ppm) and retention time (± 0.5 min). Unidentified features were evaluated via Metaboanalyst 5.0.[146] Spectra in the form of .mzML files were compressed, uploaded to Metaboanalyst, and processed using

the Auto-optimized feature in the LC-MS Spectra Processing module. As some batch effects were observed, features that were found to significantly vary (p value < 0.05) between batches based on an analysis of variance (ANOVA) were removed to lessen the chance of false statistical assumptions; this resulted in analysis of 26 known metabolites and 459 unidentified features. Heatmaps were generated using R with a custom script. Known and unidentified features were uploaded to Metaboanalyst for statistical analyses and visualization using the following parameters: features with missing values (< 25%) replaced by one-fifth of the minimum positive value, normalized by sum, and log transformed. All other statistical analyses (e.g., partial least squares discriminant analyses or PLS-DAs) were performed using Metaboanalyst. Venn Diagrams were created using an in-house Python script.

Equine bloodwork was statistically evaluated in Metaboanalyst by performing 2-sample unpaired, equal group variance t-tests between various groupings (CCP vs. RP, diet, sex, and age group) using the same normalization and transformation procedure as metabolomics data. Box plots were generated using an in-house Python script.

Statistical conclusions based on *p* values were categorized as follows: *p* values of ≤0.01, ≤0.05, and ≤0.1 reflect statistical assumptions made with confidence intervals of 99%, 95%, and 90%, respectively.

Appendix

Table 4.5. Metaboanalyst results from T-Test comparisons between CCP and RP for blood chemistries (plasma)

Analyte	**t.stat**	**p.value**	**FDR**
CREAT	-2.0819	0.04051	0.28524
ALB	-2.0757	0.041096	0.28524
LDH	-1.899	0.061123	0.28524
AST	-1.6905	0.094774	0.33171

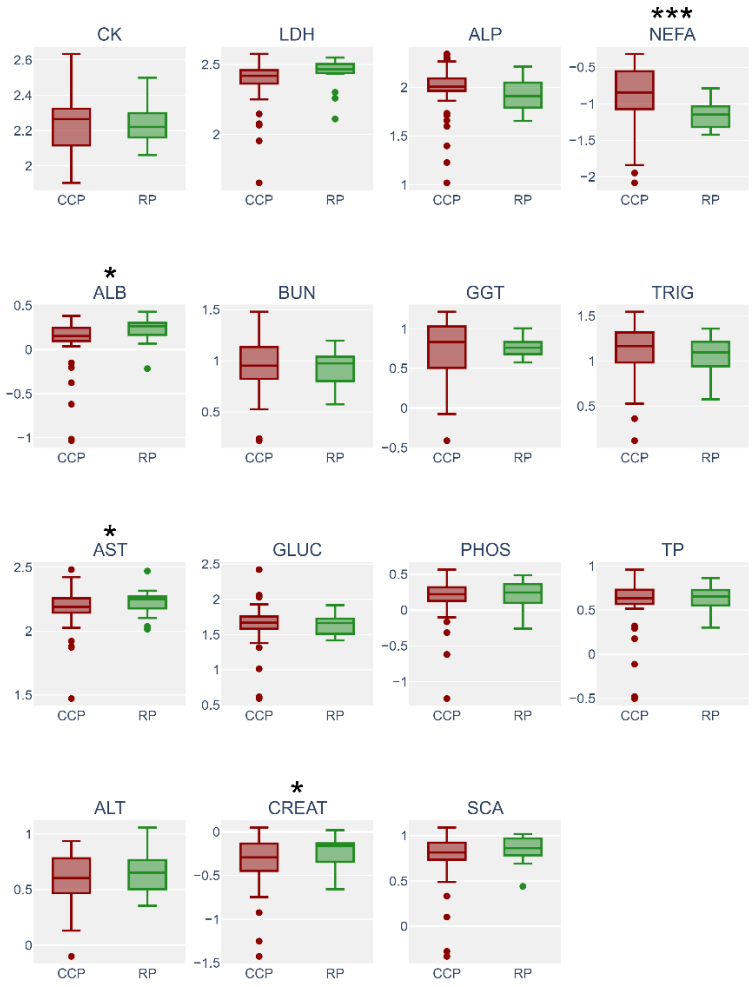

Figure 4.6. Box plots of blood serum data conveying the differences between the CCP and RP. Asterisks represent statistical significance (p value ≤ 0.1 = *; p value ≤ 0.05 = **; p value ≤ 0.01 = ***). LDH: lactate dehydrogenase (p value 0.07), U/L; ALP: alkaline phosphatase, U/L; ALB: albumin (p value 0.06), g/dL; BUN: blood urea nitrogen, mg/dL; GGT: gamma-glutamyl transferase, U/L; AST: aspartate amino transferase, U/L; TP: total protein, g/dL; GLUC: glucose, mg/dL; PHOS: phosphate, mg/dL; ALT: alanine transaminase, U/L; CREAT: creatinine (p value 0.08), mg/dL; TRIG: triglycerides, mg/dL; CK: creatinine kinase, U/L; NEFA: non-esterified fatty acids (p value 0.00_6), mEq/L; SCA: serum calcium, mg/dL

Table 4.6. Metaboanalyst results from T-Test comparisons between groups

	Analyte	**t.stat**	**p.value**	**FDR**
Diet (C vs. S) for blood chemistries (plasma)	BUN	-3.1391	0.002364	0.033102
	Phos	-2.7717	0.006916	0.048412
	TP	-2.3217	0.022765	0.10624
	ALB	-1.9277	0.057404	0.16412
	GLUC	-1.8552	0.067205	0.16412
	LDH	-1.8339	0.070336	0.16412
Sex (mare vs. gelding) for blood chemistries (plasma)	CREAT	2.8082	0.006241	0.047123
	Phos	2.7092	0.008228	0.047123
	ALB	2.6343	0.010098	0.047123
Age group (below 20 vs. 20 and above) for blood chemistries (plasma)	Phos	-3.7581	0.000322	0.004503
	ALB	-3.1685	0.002162	0.015134
	LDH	-2.4968	0.01456	0.067946
	TP	-2.0713	0.041513	0.14528
	ALT	1.9732	0.051884	0.14528
	BUN	-1.7888	0.077386	0.18057
Diet (C vs. S) for blood chemistries (serum)	BUN	-2.5498	0.012687	0.10881
	PHOS	-2.5235	0.013601	0.10881
	TP	-2.1816	0.032076	0.17107
	ALT	2.026	0.0461	0.1844
	SCA	-1.867	0.065564	0.2098
	ALB	-1.7397	0.085757	0.22868

Table 4.7 continued

Sex (mare vs. gelding) for blood chemistries (serum)	PHOS	3.1301	0.00244	0.022982
	ALB	3.0758	0.002873	0.022982
	CREAT	2.9336	0.00437	0.023309
	TRIG	2.2569	0.026744	0.10698
	SCA	1.8891	0.062502	0.20001
	CK	1.6753	0.097773	0.22348
Age group (below 20 vs. 20 and above) for blood chemistries (serum)	PHOS	-3.6473	0.00047	0.007525
	ALT	3.194	0.002008	0.012152
	ALB	-3.1526	0.002279	0.012152
	SCA	-2.1607	0.033709	0.11742
	TP	-2.0545	0.043193	0.11742
	CK	-1.978	0.051371	0.11742
	LDH	-1.7817	0.078587	0.15717

Table 4.7. Fold change analysis for RP compared to CCP (RP/CCP) for metabolomics data

Metabolite	**Fold change (RP/CCP)**	**p.value**
alpha-Ketoglutarate	0.724568	0.196767
Uric acid	0.598083	0.078713
Indoleacrylate	0.631762	0.2454
Allantoin	0.372438	0.009124
Uridine	0.542886	0.036214
S-Adenosyl-L-methioninamine	0.97674	0.93986
Xylose	0.770332	0.115634
Taurine	0.668531	0.197207
Arginine	0.892785	0.491743
Tryptophan	1.045125	0.743274
Serine	0.774025	0.214143
Creatine	0.295335	0.001054
Citrulline	1.166122	0.518447
Alanine/Sarcosine	0.461614	0.002627
Valine/betaine	0.687569	0.201204
Tyrosine	0.828572	0.362614
Proline	0.888966	0.530212
Phenylalanine	0.681895	0.098501
Ornithine	1.056064	0.83341
Cystine	0.988447	0.96667
N-Acetylornithine	3.842559	0.000283
Methionine	0.545381	0.03917
Homoserine/Threonine	0.774824	0.297029

Table 4.7 continued

Glutamine	0.611119	0.085949
Cystathionine	0.777079	0.10732
Creatinine	0.911952	0.63489

Table 4.8. Metaboanalyst results from T-Test comparisons between diet (C vs. S) for metabolites

Metabolite	**t.stat**	**p.value**	**FDR**
N-Acetylornithine	3.5499	0.000628	0.14928
254.1395	-3.3856	0.001072	0.14928
Taurine	3.3077	0.001374	0.14928
380.2437	-3.2342	0.001732	0.14928
199.1335	-3.1841	0.002022	0.14928
243.1234	-3.1719	0.0021	0.14928
Glutamine	3.1629	0.002159	0.14928
261.1339	-3.1014	0.002605	0.15759
Cystine	3.0386	0.003148	0.16928
449.2626	-2.9641	0.003926	0.19004
Citrulline	2.9155	0.004528	0.19922
459.3049	-2.8684	0.005189	0.20929
S-Adenosyl-L-methioninamine	2.835	0.005712	0.21265
Ornithine	2.799	0.006328	0.21338
414.3332	-2.7264	0.007758	0.21338
211.1336	-2.6854	0.008692	0.21338
Methionine	2.6707	0.00905	0.21338
336.1812	2.661	0.009296	0.21338
326.2331	2.647	0.009659	0.21338
Homoserine/Threonine	2.6369	0.009927	0.21338
238.1445	2.623	0.01031	0.21338
361.2703	2.6217	0.010346	0.21338
432.2746	-2.616	0.010508	0.21338
384.2386	-2.6134	0.010581	0.21338
270.2072	-2.5864	0.011381	0.21515

Table 4.8 continued

216.16	-2.5745	0.011749	0.21515
243.1233	-2.5655	0.012035	0.21515
Uridine	2.5486	0.012591	0.21515
252.1602	-2.5397	0.012891	0.21515
329.2159	-2.5107	0.013922	0.22232
142.1234	-2.5021	0.014239	0.22232
271.2103	-2.4569	0.016025	0.23216
Valine/betaine	2.4472	0.016431	0.23216
alpha-Ketoglutarate	2.4397	0.016753	0.23216
242.1112	-2.424	0.017448	0.23216
229.1633	-2.4113	0.018026	0.23216
369.2747	2.4044	0.018348	0.23216
356.2436	-2.3987	0.018614	0.23216
252.1237	-2.3968	0.018707	0.23216
408.2749	-2.3444	0.021363	0.25257
356.2435	-2.336	0.021816	0.25257
Serine	2.3268	0.022325	0.25257
286.2018	-2.3236	0.022506	0.25257
501.3041	-2.3006	0.023836	0.25257
222.1493	-2.2982	0.023978	0.25257
268.1913	-2.2977	0.024005	0.25257
413.265	2.2855	0.024741	0.25395
220.0975	2.2783	0.025185	0.25395
186.1495	-2.2439	0.027405	0.26287
264.2157	-2.2356	0.027967	0.26287
466.2911	-2.229	0.02842	0.26287

Table 4.8 continued

151.0873	-2.2189	0.029128	0.26287
188.1006	-2.2177	0.02921	0.26287
202.1081	-2.2113	0.029667	0.26287
209.004	-2.2048	0.030139	0.26287
305.1754	-2.201	0.030415	0.26287
217.0293	2.1636	0.033268	0.28249
369.2392	-2.1363	0.035496	0.29566
477.3249	-2.1299	0.036041	0.29566
392.2436	-2.1171	0.037137	0.29957
140.0714	-2.0935	0.039254	0.30601
209.1542	-2.0773	0.040759	0.30601
191.0711	-2.0773	0.04076	0.30601
Alanine/Sarcosine	2.074	0.041073	0.30601
306.1787	-2.0705	0.0414	0.30601
116.9722	-2.0639	0.042039	0.30601
251.1523	-2.0549	0.04292	0.30601
307.1547	2.0542	0.042994	0.30601
374.9682	2.0362	0.044809	0.30867
175.0858	-2.0327	0.045165	0.30867
215.1284	-2.0239	0.046083	0.30867
270.1342	-2.0239	0.046088	0.30867
322.2015	-2.0169	0.046826	0.30867
125.7532	-2.0135	0.047193	0.30867
146.8665	-2.0066	0.047928	0.3093
334.2381	-1.9782	0.051112	0.32114
369.1158	1.972	0.051823	0.32114

Table 4.8 continued

307.1581	1.9697	0.052093	0.32114
360.2578	-1.9669	0.052417	0.32114
429.2963	-1.9457	0.054958	0.32884
598.4149	-1.9451	0.055034	0.32884
360.9761	1.9339	0.056414	0.33056
450.2857	-1.9261	0.057392	0.33056
283.1029	-1.9236	0.057707	0.33056
230.1756	-1.9192	0.058277	0.33056
278.1756	-1.9156	0.058736	0.33056
182.0818	-1.9032	0.060365	0.33392
485.3228	1.8945	0.061516	0.33392
xylose	1.8919	0.061863	0.33392
309.2179	-1.8902	0.062093	0.33392
228.16	-1.8728	0.064488	0.34163
358.2423	-1.867	0.065312	0.34163
446.2907	-1.8646	0.065644	0.34163
305.2117	-1.8416	0.068974	0.35514
248.9599	-1.83	0.070719	0.35523
383.327	-1.8259	0.071336	0.35523
Indoleacrylate	1.8233	0.07173	0.35523
627.5379	-1.8182	0.072519	0.35523
242.1757	-1.8173	0.072661	0.35523
320.2224	1.8114	0.073566	0.35606
170.0431	1.8027	0.074937	0.35664
Phenylalanine	1.7967	0.0759	0.35664
399.2857	-1.7789	0.078797	0.35664

Table 4.8 continued

119.0347	-1.7776	0.079007	0.35664
241.1079	-1.7762	0.079235	0.35664
328.2124	1.7745	0.079512	0.35664
238.1081	-1.7744	0.079538	0.35664
448.2698	-1.7741	0.079581	0.35664
169.0866	1.7632	0.081417	0.3614
302.1966	-1.759	0.082137	0.3614
250.1809	-1.7359	0.086168	0.37278
318.2108	-1.7353	0.086264	0.37278
338.2332	-1.7261	0.087917	0.37562
334.2019	-1.7076	0.091327	0.37562
370.2785	-1.7037	0.092046	0.37562
135.0813	-1.701	0.092548	0.37562
312.2174	-1.6988	0.092981	0.37562
113.097	-1.6911	0.094435	0.37562
255.1234	-1.689	0.094848	0.37562
370.2589	-1.6875	0.09514	0.37562
434.2542	-1.6855	0.095511	0.37562
Allantoin	1.6844	0.095732	0.37562
418.2593	-1.6805	0.096497	0.37562
231.179	-1.678	0.09698	0.37562
371.2545	-1.6757	0.097422	0.37562
381.2105	-1.6739	0.097785	0.37562

Table 4.9. Metaboanalyst results from T-Test comparisons between sex (mare vs. gelding) for metabolites

Metabolite	**t.stat**	**p.value**	**FDR**
Creatine	-5.9958	4.63E-08	2.24E-05
Cystine	-5.7997	1.08E-07	2.61E-05
Alanine/Sarcosine	-5.5842	2.69E-07	3.81E-05
Taurine	-5.547	3.15E-07	3.81E-05
Serine	-5.3606	6.87E-07	5.91E-05
Allantoin	-5.3451	7.32E-07	5.91E-05
Glutamine	-5.286	9.35E-07	6.46E-05
165.128	5.1739	1.48E-06	8.95E-05
Valine/betaine	-5.142	1.69E-06	9.07E-05
Phenylalanine	-4.7807	7.15E-06	0.000346
alpha-Ketoglutarate	-4.5786	1.57E-05	0.00069
S-Adenosyl-L-methioninamine	-4.4384	2.67E-05	0.001079
213.1322	4.2656	5.10E-05	0.001836
Homoserine/Threonine	-4.2546	5.31E-05	0.001836
Uridine	-4.2359	5.69E-05	0.001836
Tryptophan	-4.1614	7.47E-05	0.00226
Indoleacrylate	-4.1338	8.26E-05	0.002352
xylose	-4.0584	0.000108	0.002916
434.2542	3.8803	0.000204	0.005192
Cystathionine	-3.8212	0.00025	0.005779
Tyrosine	-3.8207	0.000251	0.005779
Ornithine	-3.7736	0.000295	0.006492
Methionine	-3.6992	0.00038	0.008005
198.1018	3.5296	0.000671	0.012935

Table 4.9 continued

188.1006	3.5254	0.00068	0.012935
330.2281	3.519	0.000695	0.012935
762.5618	3.5059	0.000726	0.013007
Citrulline	-3.4081	0.000997	0.017238
230.1545	3.3378	0.001249	0.020815
229.1633	3.3277	0.00129	0.020815
334.202	3.3095	0.001367	0.02134
128.1079	3.2725	0.001536	0.023228
236.1652	3.2016	0.001916	0.028105
278.1756	3.1544	0.002216	0.031543
501.3041	3.1256	0.00242	0.033461
383.2779	3.0857	0.002731	0.036498
285.2177	3.0743	0.002827	0.036498
261.1339	3.0605	0.002947	0.036498
254.1395	3.0601	0.002951	0.036498
292.1745	3.0486	0.003054	0.036498
202.1081	3.0446	0.003092	0.036498
414.3332	2.9629	0.00394	0.045405
242.1757	2.954	0.004045	0.045526
292.1914	2.9366	0.004257	0.046823
305.1754	2.9216	0.004447	0.04747
311.205	2.9167	0.004512	0.04747
177.1328	2.8571	0.005361	0.055202
Creatinine	-2.8446	0.005557	0.055519
360.2385	-2.8406	0.005621	0.055519
199.0972	2.8309	0.005778	0.055927

Table 4.9 continued

459.3049	2.8075	0.006176	0.058613
264.1318	2.791	0.006472	0.060243
326.1969	2.7521	0.007221	0.065279
269.2118	2.749	0.007283	0.065279
271.2104	2.7397	0.007476	0.065788
395.1682	2.7325	0.007628	0.065925
295.0518	2.7152	0.008004	0.067183
257.1392	2.7131	0.008051	0.067183
306.1787	2.6971	0.008417	0.069045
270.2072	2.6862	0.008672	0.069957
177.0597	2.6555	0.009436	0.074872
231.179	2.6447	0.009717	0.075857
313.213	2.6237	0.010289	0.079049
175.0858	2.6078	0.010744	0.081248
116.9722	2.5868	0.011367	0.084638
343.2594	-2.5781	0.011637	0.085335
203.1115	2.5371	0.01298	0.093768
382.2746	2.5238	0.013446	0.095703
252.1237	2.5161	0.013723	0.096259
135.0813	2.5021	0.01424	0.098459
386.291	2.4314	0.017115	0.11667
200.1288	2.4136	0.017919	0.12045
268.1913	2.4015	0.018483	0.12255
302.2332	2.394	0.018841	0.12296
322.2383	2.3896	0.019054	0.12296
175.1165	2.3784	0.019605	0.12485

Table 4.9 continued

422.2905	2.3731	0.01987	0.1249
277.1439	2.3291	0.022196	0.13543
398.2652	2.3274	0.022293	0.13543
202.1526	2.3258	0.022385	0.13543
248.9599	2.3145	0.023024	0.13758
137.0605	2.3009	0.023816	0.13996
Uric acid	-2.2978	0.024001	0.13996
293.0486	2.2905	0.024442	0.14083
141.0166	2.2775	0.025239	0.14371
248.1651	2.2689	0.02578	0.1445
184.1702	2.2658	0.025975	0.1445
409.2419	-2.2509	0.026943	0.14819
441.3327	-2.2168	0.029276	0.15921
227.1479	2.2024	0.030313	0.16249
242.1112	2.198	0.030634	0.16249
228.16	2.1946	0.030886	0.16249
87.04483	-2.1819	0.031847	0.16574
236.2016	2.1737	0.032477	0.16722
243.1233	2.1554	0.033921	0.17163
600.5022	2.154	0.034042	0.17163
446.2907	2.139	0.035271	0.17599
232.0134	-2.126	0.036373	0.17964
386.2693	2.1128	0.037519	0.18343
463.317	2.0963	0.03899	0.18786
466.2911	2.094	0.039203	0.18786
448.2698	2.0789	0.040607	0.19061

Table 4.9 continued

225.1492	2.0758	0.040899	0.19061
411.2857	2.0752	0.040958	0.19061
262.1807	2.0474	0.043667	0.20128
196.0612	2.0406	0.044354	0.20252
127.001	2.0287	0.045582	0.20619
305.2117	2.0088	0.047693	0.21374
271.2103	1.9911	0.049641	0.22043
299.2053	1.9784	0.05109	0.22452
253.1441	1.9749	0.05149	0.22452
200.0536	1.9662	0.052501	0.22688
321.0795	1.9553	0.053792	0.2281
181.1231	1.9469	0.054805	0.2281
204.0914	1.9439	0.055178	0.2281
281.1863	-1.943	0.055291	0.2281
461.3097	1.9426	0.055332	0.2281
238.1081	1.9404	0.055611	0.2281
202.0119	1.9337	0.056444	0.22957
263.1285	1.9211	0.058027	0.23404
339.1809	1.9106	0.059382	0.23753
187.0972	1.8881	0.062389	0.24751
356.2435	1.8838	0.062977	0.24781
322.2015	1.8795	0.063567	0.24812
145.014	1.8686	0.065086	0.25113
293.1867	1.8569	0.066754	0.25113
284.2053	-1.8565	0.066811	0.25113
322.1322	1.8517	0.067502	0.25113

Table 4.9 continued

214.1443	1.8497	0.067798	0.25113
315.1922	1.8487	0.067944	0.25113
294.2067	-1.8441	0.068609	0.25113
369.1158	1.8412	0.069035	0.25113
252.1602	1.8397	0.069265	0.25113
434.2542	1.8379	0.069527	0.25113
598.4149	1.8252	0.071438	0.25612
209.1542	1.8182	0.072515	0.25689
399.2857	1.8165	0.072771	0.25689
212.1652	1.8127	0.073364	0.25689
284.1498	1.8101	0.073778	0.25689
146.8665	1.806	0.07441	0.25724
329.2159	1.7804	0.078534	0.26865
194.9461	1.7759	0.079281	0.26865
238.1445	1.7754	0.079374	0.26865
266.1509	1.7435	0.084821	0.28346
87.04486	1.7429	0.084922	0.28346
278.1473	1.7386	0.085682	0.28404
370.2785	1.735	0.086325	0.28423
156.9904	1.7264	0.087858	0.28732
292.1551	1.7208	0.088879	0.28756
230.1756	1.7195	0.089121	0.28756
248.2016	1.7092	0.091019	0.29174
229.1439	-1.6991	0.092919	0.29393
370.2589	-1.6973	0.093247	0.29393

Table 4.9 continued

327.2366	1.6959	0.093524	0.29393
397.2702	1.69	0.094657	0.29557
361.2014	1.675	0.097564	0.3027

Table 4.10. Metaboanalyst results from T-Test comparisons between age group (below 20 vs. 20 and above) for metabolites

Metabolite	**t.stat**	**p.value**	**FDR**
Creatine	4.8452	5.55E-06	0.002685
Alanine/Sarcosine	3.5068	0.000723	0.17503
181.1231	-2.7932	0.006432	0.94452
Methionine	2.3907	0.019	0.94452
Allantoin	2.3768	0.019682	0.94452
135.0813	-2.3649	0.020287	0.94452
87.04483	2.2813	0.025001	0.94452
285.1258	2.1792	0.032048	0.94452
238.1445	2.0992	0.038733	0.94452
Uridine	2.0911	0.039469	0.94452
250.1809	2.0403	0.044385	0.94452
Homoserine/Threonine	1.9935	0.049377	0.94452
202.1081	-1.9614	0.053073	0.94452
248.2016	-1.9523	0.05415	0.94452
279.2435	1.9481	0.054662	0.94452
397.2702	-1.9272	0.057254	0.94452
293.1754	-1.9191	0.058289	0.94452
Indoleacrylate	1.9185	0.058369	0.94452
380.2437	-1.9146	0.058869	0.94452
199.0972	1.9143	0.058904	0.94452
294.2067	-1.8887	0.062307	0.94452
alpha-Ketoglutarate	1.853	0.067316	0.94452
360.2385	1.8411	0.069059	0.94452
277.1805	1.8285	0.070937	0.94452

Table 4.10 continued

283.1029	-1.8083	0.074053	0.94452
162.965	-1.7913	0.076758	0.94452
292.1914	-1.7761	0.079248	0.94452
231.179	-1.7611	0.081783	0.94452
204.0914	-1.7586	0.082207	0.94452
125.7532	-1.7512	0.083474	0.94452
250.1444	-1.7423	0.085038	0.94452
514.3166	1.7407	0.085315	0.94452
223.1335	-1.7371	0.085958	0.94452
N-Acetylornithine	-1.7341	0.086487	0.94452
299.2048	1.7182	0.089361	0.94452
330.2281	-1.6951	0.093683	0.94452
271.2103	-1.6888	0.094873	0.94452
311.2224	-1.6809	0.096407	0.94452
Tyrosine	1.6773	0.097109	0.94452

Table 4.11. Statistically significant features between CCP and RP lipid profiles. Blue features are more abundant in the CCP while red features are more abundant in the RP.

Feature	Fold change	Raw p value
Unknown-297.08447	0.001108	4.02E-05
Unknown-393.29761	0.051082	0.096742
Unknown-422.14059	0.074808	7.47E-05
Unknown-297.13846	0.075972	0.006507
Unknown-377.1424	0.086377	6.78E-05
Unknown-197.12833	0.097359	0.00036
Unknown-517.14807	0.12151	3.43E-05
Unknown-424.15585	0.14949	0.000216
Unknown-323.15436	0.15485	0.057681
Unknown-540.14825	0.15492	0.000291
Unknown-410.17609	0.15628	0.000113
RIKEN N-VS1 ID-1238 from Mouse_Feces_WT_N_Ctr	0.17075	0.000206
Unknown-426.17126	0.17853	0.00012
Unknown-846.89752	0.18549	0.024565
RIKEN N-VS1 ID-1251 from Mouse_Feces_WT_N_Ctr	0.18951	4.83E-05
Unknown-888.94598	0.20176	0.006464
Unknown-235.12328	0.20215	0.075996
Unknown-860.91467	0.2404	0.014629
Unknown-1294.36084	0.27739	0.009625
Unknown-477.24973	0.28085	0.00132
Unknown-355.01068	0.29402	0.033562
Unknown-491.133	0.29652	0.000219

Table 4.11 continued

Unknown-343.9949	0.29731	0.011111
Unknown-902.95947	0.30527	0.025399
Unknown-299.1543	0.31712	0.008038
Unknown-229.15443	0.32556	0.001255
Unknown-297.13837	0.32771	0.011736
Unknown-1052.49683	0.34745	0.019316
Unknown-400.1553	0.35597	0.001918
Unknown-547.21802	0.36365	0.000202
Unknown-448.3905	0.36855	0.001107
Unknown-430.38022	0.37678	0.000775
Unknown-818.86688	0.386	0.019491
Unknown-315.13406	0.38821	0.002359
Unknown-514.13281	0.392	0.002299
Unknown-341.85742	0.39636	0.045501
Unknown-204.12305	0.40842	0.001569
Unknown-498.90146	0.41289	0.020315
Unknown-702.21295	0.41359	0.033596
Unknown-313.11942	0.42122	0.001983
Unknown-477.83231	0.42981	0.021128
Unknown-319.22208	0.43027	0.000507
Unknown-583.25574	0.43946	0.022616
TG 56:7|TG 16:0_18:2_22:5, TG 56:7|TG 16:0_18:2_22:5	0.44245	0.000172
Unknown-419.31598	0.45536	0.057003
DGCC 36:2	0.49395	0.037802

Table 4.11 continued

RIKEN P-VS1 ID-13366 from Mouse_Brain_WT_N_F1	0.51855	0.016398
Unknown-565.56635	0.53052	0.099544
Unknown-546.81781	0.53096	0.002313
Unknown-792.85852, Unknown-792.85852	0.5374	0.092172
Unknown-565.56671	0.54028	0.093359
Unknown-537.53546	0.54365	0.009476
RIKEN N-VS1 ID-1263 from Mouse_Feces_WT_N_Ctr	0.54459	0.006726
Unknown-399.25012	0.55497	0.057774
Unknown-293.04886	0.55809	0.021668
PC O-38:6	0.57391	0.004185
Unknown-998.28656	0.57656	0.021214
Unknown-627.75818	0.57878	0.090869
TG 56:8|TG 16:0_18:3_22:5	0.58469	0.001867
Unknown-210.88419	0.58502	0.060895
Unknown-342.85458	0.59783	0.088596
Unknown-772.27216	0.60068	0.003366
TG 45:1|TG 14:0_15:0_16:1	0.60951	0.097599
Unknown-199.85077	0.61024	0.084656
Unknown-846.29242	0.61165	0.018941
TG 48:0|TG 14:0_16:0_18:0	0.61232	0.081192
Unknown-559.51721	0.61439	0.044989
Unknown-593.59833	0.61664	0.00676
Unknown-275.90616	0.61689	0.073528

Table 4.11 continued

TG 48:0|TG 16:0_16:0_16:0	0.61836	0.079363
Unknown-168.83632	0.62037	0.02184
Unknown-197.96317	0.62396	0.023411
Unknown-316.94778, Unknown-316.94778	0.62615	0.022482
Unknown-170.83336	0.62702	0.044653
Unknown-920.30884	0.62833	0.020372
Unknown-428.18759	0.62858	0.03675
Unknown-225.06168	0.63152	0.023143
Unknown-437.23965	0.63562	0.040528
Unknown-294.93842	0.63875	0.049232
Unknown-392.25433	0.6397	0.065832
Unknown-582.59277	0.64512	0.046321
Unknown-1368.38342	0.64746	0.040085
Unknown-264.15945, Unknown-264.15945	0.64796	0.021455
PC O-36:5|PC O-16:1_20:4	0.64821	0.005693
Unknown-520.90961, Unknown-520.90961	0.65014	0.029352
TG 49:3;O|TG 16:0_16:1_17:2;O	0.65022	0.073929
RIKEN P-VS1 ID-19012 from Mouse_Macrophage_WT_N_F1AA	0.65039	0.039775
Unknown-160.84203	0.65039	0.045317
Unknown-288.92148	0.65403	0.045528
Unknown-610.18402	0.65842	0.021199

Table 4.11 continued

DG 34:0	0.66036	0.034704
Unknown-475.4144, Unknown-475.4144	0.66124	0.022671
Unknown-435.33286	0.66366	0.041872
Unknown-684.20197	0.66428	0.037865
LPC 18:2/0:0	1.5042	0.001969
PC 38:3|PC 20:1_18:2	1.5199	0.002215
TG 50:6|TG 14:0_18:3_18:3, TG 50:6|TG 14:0_18:3_18:3	1.5491	0.004696
PC 37:2|PC 19:0_18:2	1.5493	0.001268
PI 36:3|PI 18:1_18:2	1.5598	0.000721
CE 18:3	1.5821	0.008658
RIKEN P-VS1 ID-11485 from Mouse_Brain_WT_N_F1	1.5847	0.009894
PE 36:2|PE 18:0_18:2	1.5929	0.061994
Unknown-1250.17444	1.6538	0.040018
PC 38:2, PC 38:2	1.7156	0.003447
TG 54:9|TG 18:3_18:3_18:3, TG 54:9|TG 18:3_18:3_18:3	1.7221	0.002681
PE 36:3|PE 18:1_18:2	1.7352	0.007359
CE 18:1	1.7396	0.001194
LPC 16:1/0:0	1.7646	0.002755
Unknown-648.70099	1.7731	0.089313
PC 33:1, PC 33:1	1.7768	0.000253
Unknown-1324.18408	1.782	0.050586
PI 36:1|PI 18:0_18:1	1.8296	0.009704

Table 4.11 continued

PC 34:1|PC 16:0_18:1	1.8544	0.000644
LPC 16:0/0:0	1.8683	0.000677
Unknown-1076.52429	1.8722	0.016872
Unknown-1628.11035	1.8827	0.038247
LPC 16:0, LPC 16:0	1.9441	0.000132
LPC 15:0/0:0	1.9848	0.000246
PC 35:2, PC 35:2, PC 35:2	1.9855	3.77E-05
LPC 18:3/0:0	2.0288	0.000303
Unknown-636.67639	2.0371	0.077076
PC O-34:2	2.0466	0.005804
LPC 17:0, LPC 17:0	2.0663	0.000207
LPC 18:1/0:0	2.0712	0.000172
RIKEN P-VS1 ID-12188 from Mouse_Kidney_WT_N_F1EPA	2.0737	0.00467
Unknown-1008.53979	2.1088	0.009349
RIKEN N-VS1 ID-6109 from Mouse_Plasma_ApoEKO_N_F1DHA	2.1583	0.013606
LPC 18:1, LPC 18:1	2.1721	0.000346
Unknown-1560.11853	2.3005	0.055638
PC 36:1|PC 18:0_18:1	2.3205	0.000298
Unknown-673.73291	2.3267	0.085205
LPC 14:0/0:0	2.4245	0.000125
PC 34:1	2.4429	0.003834
Unknown-617.66986	2.4961	0.072409
Unknown-561.60675	2.4998	0.076311
PC 37:2	2.5081	0.000101

Table 4.11 continued

Unknown-589.63947	2.5109	0.06905
RIKEN P-VS1 ID-19454 from Mouse_AdrenalGlands_fads2KO_N_Ctr	2.5381	0.01761
PC 38:1	2.5768	0.000613
PC 35:1, PC 35:1	2.5888	0.000151
PC 36:1	2.5927	0.000496
LPC 20:0/0:0	2.6441	0.000178
RIKEN P-VS1 ID-11818 from Cell_HeLa_WT_N_Ctr	2.8808	0.002852
RIKEN N-VS1 ID-6571 from Mouse_BAT_fads2KO_N_Ctr	2.9504	0.007913
Unknown-1036.56848	3.0555	0.008202

CHAPTER 5.
ADVANCED VISUALIZATION TECHNIQUES TO CLASSIFY OXIDIZED LIPIDS IN COMPLEX MIXTURES

Modernizing Classic Graphical Methods for Lipidomics: A New Approach to Analyzing Complex Datasets

5.1 Abstract

The deduction of conclusive scientific evidence from untargeted mass spectrometry analyses is a constant work in progress among the mass spectrometry community. Statistical algorithms, data processing programs, and data visualization techniques are continuously being developed to manage the profound amount of data obtained from untargeted analyses and more efficiently reach a scientific conclusion. Two of the oldest and most utilized techniques to visualize large, complex datasets are van Krevelen Diagrams and Kendrick Mass Defect plots. Each of these graphical techniques have been successful in classifying compound classes among complex mixtures, especially when the mixture contains compounds that differ by repeating units. Considering lipids meet these criteria as they represent different subclasses (e.g., different headgroups) and are composed of repeating units (i.e., tail length), it is surprising that little research has been done on using these graphical methods to analyze complex lipidomics datasets. In this study, a newly developed Python program that generates traditional and modernized versions of van Krevelen Diagrams and Kendrick Mass Defect plots is utilized to measure the potential for these techniques to properly classify oxidized lipids in lipidomics datasets. Here, a modernized version of the Kendrick Mass Defect plot that incorporates a third dimension measuring heteroatom content was constructed and shows promise as a lipid classification model in untargeted lipidomics analyses.

5.2 Introduction

The ability to confine complex mass spectrometry data to a simple visual that yields informative results has been desired for decades. In 1950, van Krevelen condensed data from an analysis of coal to a simple two-dimensional graph that plotted the oxygen-to-carbon (OC) and hydrogen-to-carbon (HC) ratios of analytes, yielding structural information on the components in the mixture; this graphical method was termed the van Krevelen (vK) Diagram.[147-149] Some years later, Kendrick developed a graphical method (i.e., Kendrick Mass Defect or KMD plots) to evaluate petrochemical mixtures that illustrated each compound class as a distinct series.[150, 151] While both of these orthogonal

visualization methods have been heavily utilized to characterize complex mixtures for years, their use cases are quite specific. For example, KMD plots have mainly been useful in the analysis of petrochemicals, where analytes primarily differ by units of CH_2. vK diagrams have been applied to multiple complex matrices, including petroleum and biological matrices.[148]

Several attempts have been made to increase the utility of graphical methods in modern mass spectrometry analyses. For example, a re-evaluation of the compound classification boundaries in vK diagrams was conducted using publicly available data, yielding an entirely new set of classification constraints that promoted a more accurate prediction of compound classes.[148] Modifications to traditional vK plots were conducted by Kew and co-workers who developed a Python-based program that allows plots to be generated in an interactive environment, termed *i*-van Krevelen.[149] Similarly, the generation of multidimensional (i.e., 3D) vK plots was found to be successful in differentiating nitrogenous compounds in coal mixtures.[152]

At the current time, little work has been devoted to using these traditional and modernized graphical techniques to investigate lipid composition and, more specifically, their ability to predict lipid oxidation. Considering vK diagrams can differentiate compound classes and KMD can be used to differentiate series within a class, it was proposed that a combination of these methods could be used to identify constraints of lipid oxidation. Herein, a Python-based, 3D plotting method is developed and utilized to explore potential benefits of combining vK and KMD plots in lipidomics.

5.3 Results and discussion

5.3.1 ***Traditional 2D van Krevelen and Kendrick Mass Defect plots are unable to isolate oxidized lipid species***

A data compilation of 4771 lipid species comprising approximately 130 lipid classes (including 424 oxidized lipids of 6 phospholipid classes) was used to generate traditional vK and KMD plots. A summarized list of the species used in the model can be found in **Appendix Table 5.1** and information on lipid nomenclature can be found in the

Experimental section. A KMD evaluation (**Figure 5.1**) of the dataset primarily showed a large cluster of lipids with some species (i.e., CLs, PIMs, and CoAs) clustering in small groups together. In this 2D plot, however, oxidized lipids were overlaid with non-oxidized lipids of the same class. Little information could be derived from the 2D vK plot (**Figure 5.2**) of the lipid dataset as no distinct clusters could be observed and, similar to the KMD plot, oxidized lipids were unable to be differentiated from non-oxidized lipids. Upon application of classic boundaries for vK plots (**Figure 5.3**), it is clear why this classification scheme required re-evaluation as many lipid species were classified incorrectly. Though the stoichiometric classification developed by Rivas-Ubach[148] was not completely able to capture the lipid species, it performed substantially better than the previous set of boundaries (**Figure 5.4**). Regardless, the classic 2D plots were insufficient at resolved oxidized lipid species.

*5.3.2 **Modernized 3D KMD plots to differentiate lipid species***

To evaluate the potential separation capacity of a combined vK and KMD plot, the lipid dataset was plotted against a traditional vK (OC vs. HC) with an additional dimension representing the KMD (**Figure 5.5**). The resulting plot displayed one large cluster with an indication of multiple layers that may be graphically explained by an exponential curve. Unlike some of the previous plots, series of lipid species could not readily be distinguished.

One study[152] has indicated the importance of heteroatoms in vK analyses. Thus, a 3D plot with stoichiometric boundaries[148] was generated for the comparison OC, HC, and heteroatom content (O + N + S + P; **Figure 5.6**). With the added dimension of heteroatoms, the stoichiometric boundaries[148] largely encompassed the lipid dataset. Upon a closer investigation of the 3D graphical representation, it appears that some series were fully separated (i.e., the PS series was separated from other phospholipids). Additionally, most oxidized phospholipids were separated from non-oxidized phospholipids.

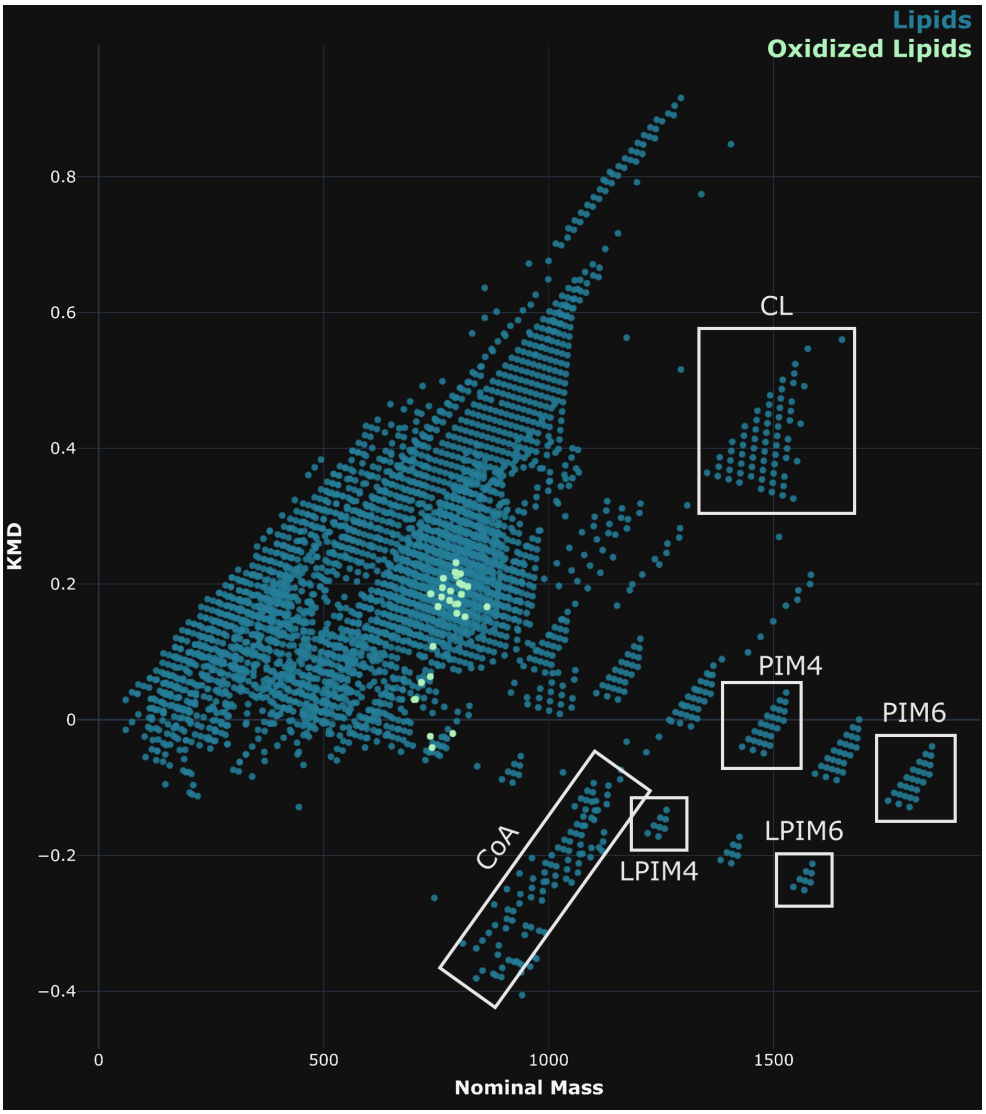

Figure 5.1. Traditional KMD of lipids and oxidized lipids from LIPID MAPS® with specific clusters of species highlighted in the white boxes.

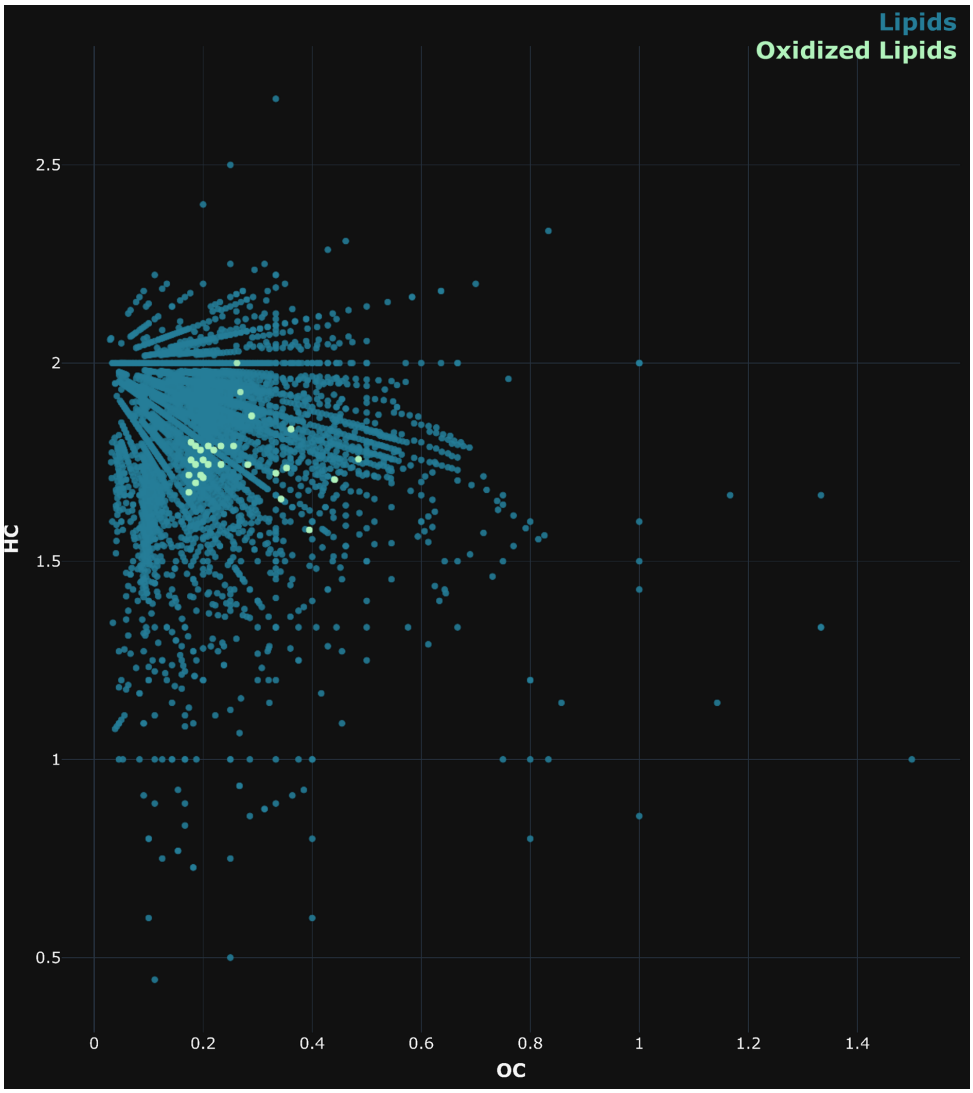

Figure 5.2. vK diagram of lipids and oxidized lipids from LIPID MAPS®.

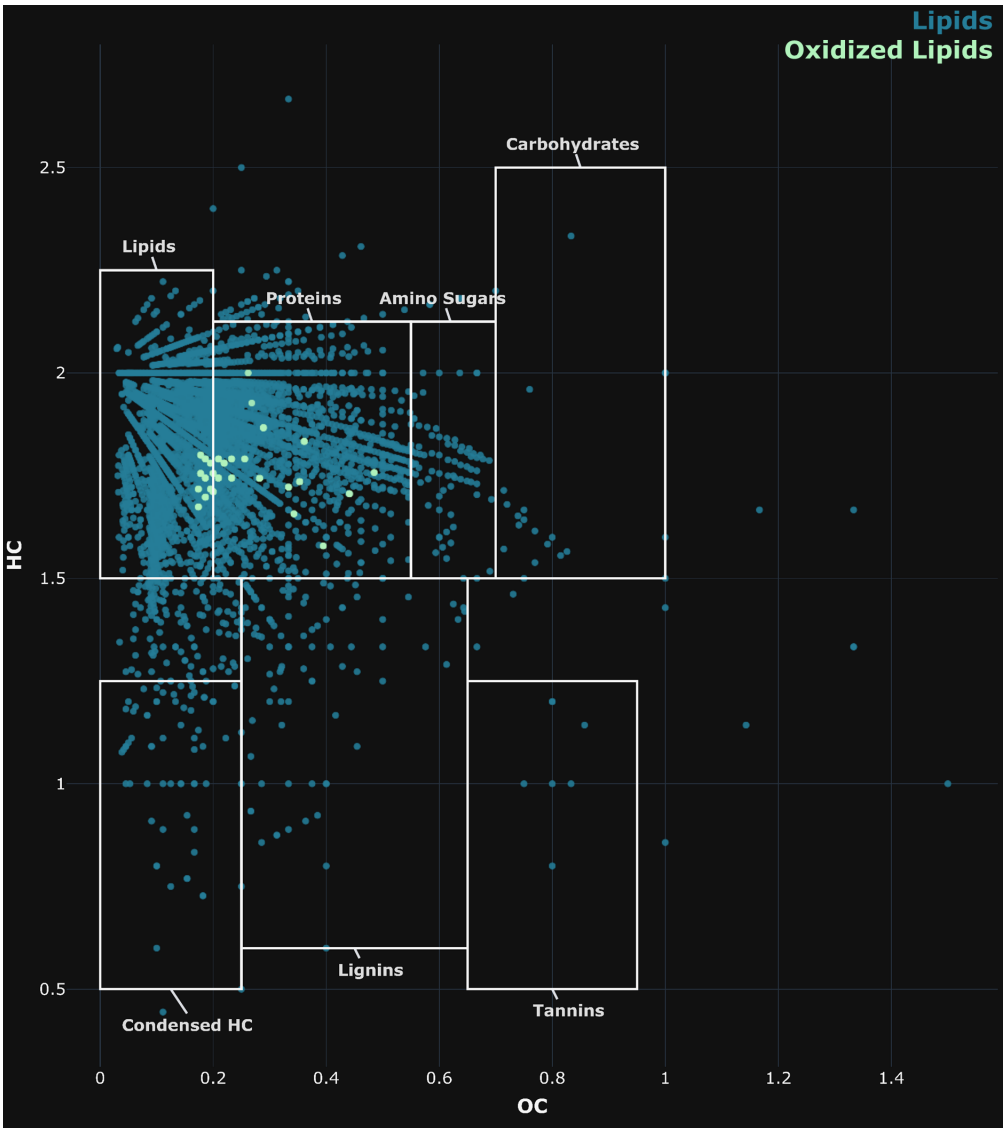

Figure 5.3. vK diagram of lipids and oxidized lipids from LIPID MAPS® with classic boundaries.[147]

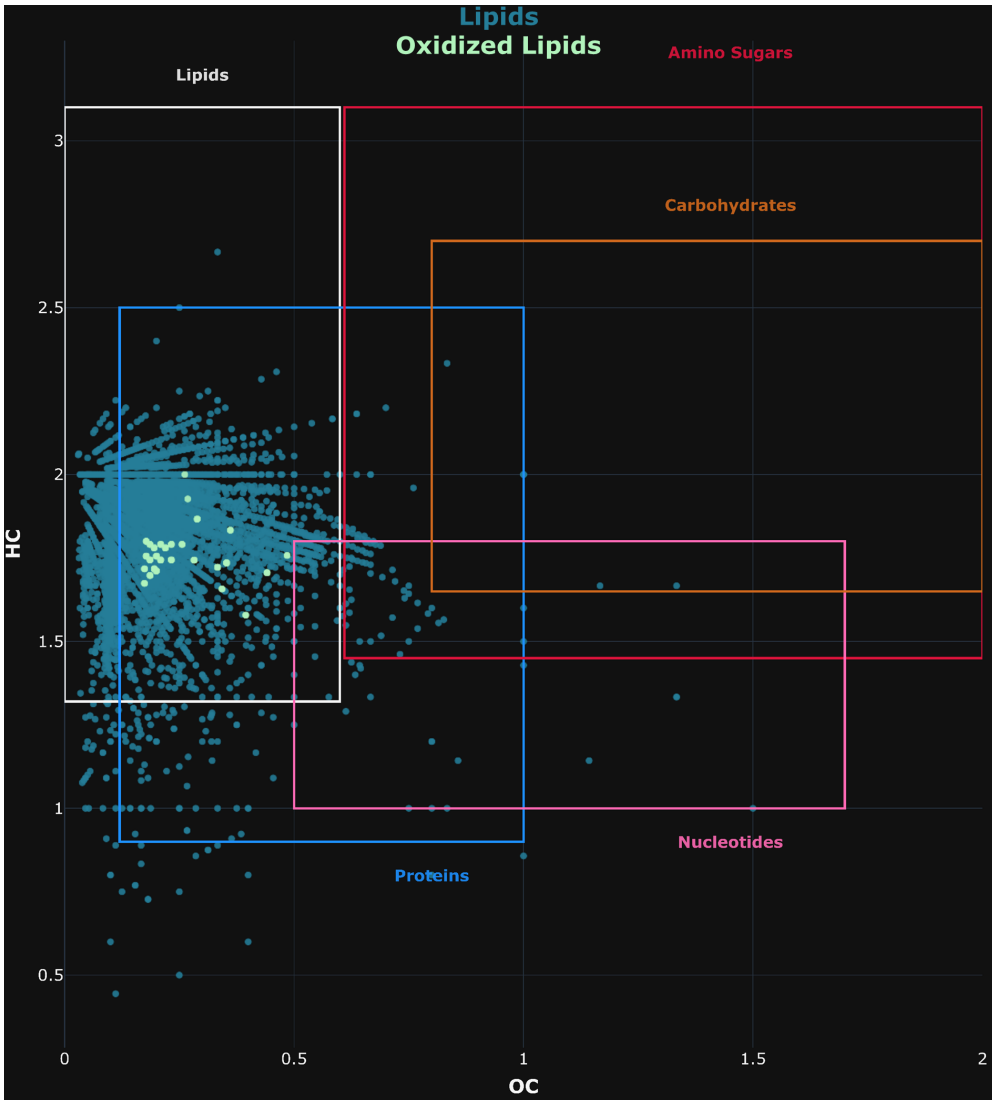

Figure 5.4. vK diagram of lipids and oxidized lipids from LIPID MAPS® with re-evaluated stoichiometric boundaries.[148]

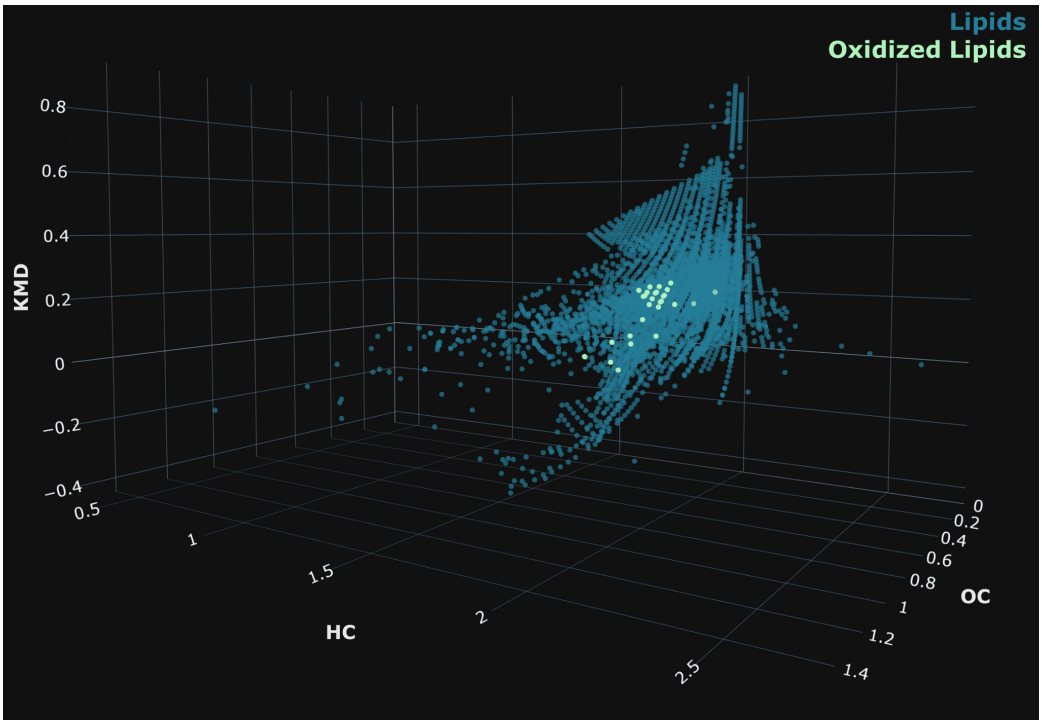

Figure 5.5. Combination vK and KMD plot of lipids and oxidized lipids from LIPID MAPS®.

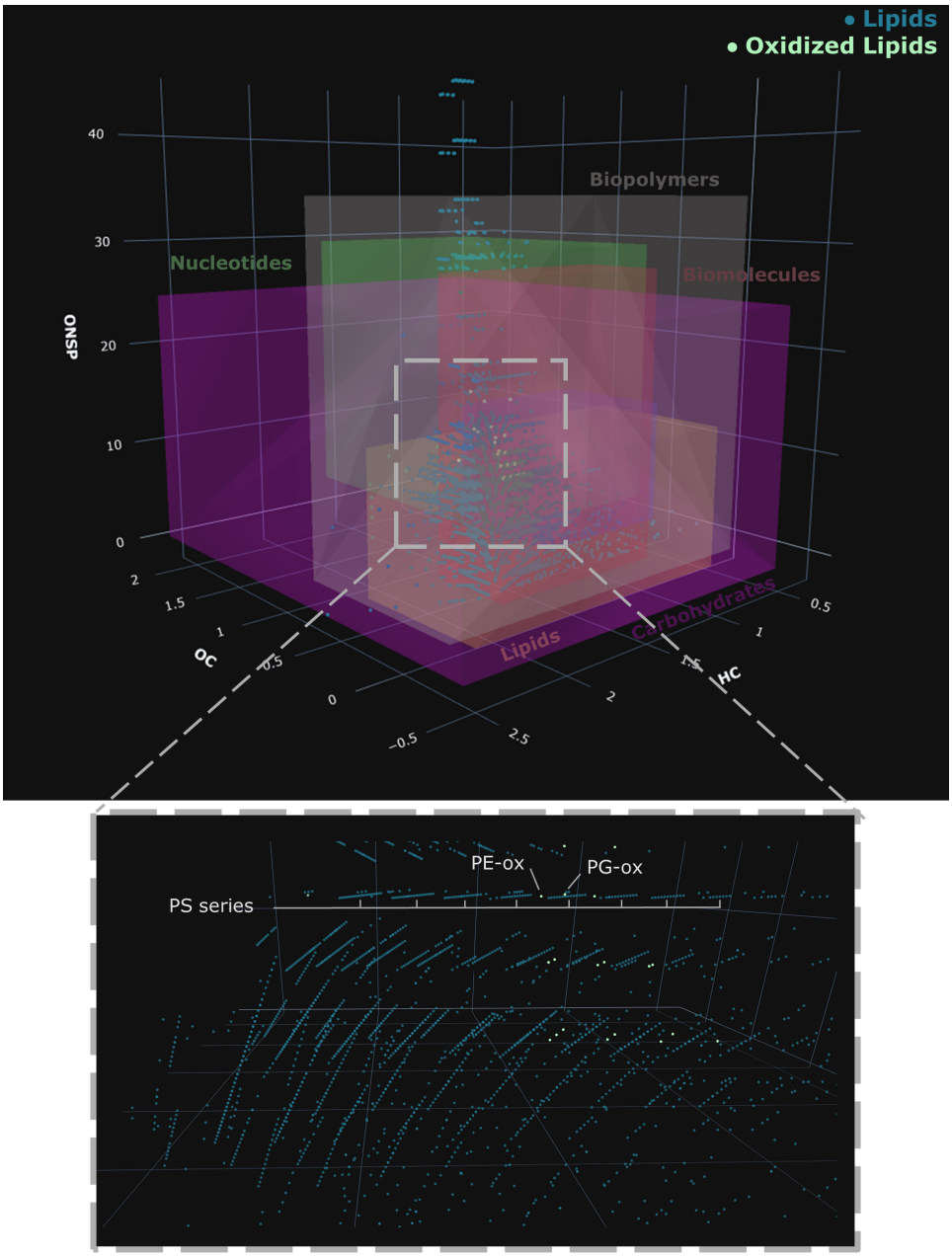

Figure 5.6. 3D vK diagram with z-axis representing the sum of heteroatoms (O, N, S and P) of lipids and oxidized lipids from LIPID MAPS® with re-evaluated stoichiometric boundaries.[148] A zoomed-in visual of the data without boundaries is shown in the lined box.

The ability of the traditional KMD plot to differentiate some lipid classes combined with the separation offered by heteroatom count led to the amalgamation of a traditional KMD plot with an additional heteroatom axis (**Figure 5.7**). Though the visuals are complex, substantial ladder-like spatial separation between many lipid classes was observed in this plot, which was termed a "modernized KMD plot". To reduce complexity, all species other than oxidized and non-oxidized phospholipid species were removed and the separation capability was further evaluated (**Figure 5.8**). Clearly, headgroups such as PI and PI-O are almost completely separated from other groups and levels of unsaturation within the lipid species are separated linearly. Importantly, within the modernized KMD plot, oxidized PCs and PEs were offset from non-oxidized phospholipids at the same level (**Figure 5.9**). This spatial difference may have been achieved in traditional 2D KMD plots as this offset is a result of KMD; however, the modernized KMD promotes the tiered separation of headgroups and results in a more extensive separation between oxidized and non-oxidized phospholipids.

To evaluate this model using an experimental dataset, a lipidomics analysis (refer to **Chapter 4**) expected to contain unannotated oxidized lipids was applied. Chemical formulae were generated (based on exact mass and fragmentation data) for unannotated features and used to create a dataset of unknown features. When plotted in the modernized KMD format (**Figure 5.10**), the data resembled the tiered format illustrated by the known lipids data derived from LIPID MAPS®. An overlay of known oxidized and non-oxidized phospholipids with the unknown features suggested that many unknown features may be unannotated, known phospholipids as they fall in the same series. Importantly, multiple data points that were offset from linear phospholipid series were present, suggesting that these features represent unannotated and potentially uncharacterized oxidized lipids.

5.4 Conclusions

In this investigation, classic and modernized graphical methods (i.e., vK diagrams and KMD plots) to visualize complex lipids datasets were evaluated. Using a database

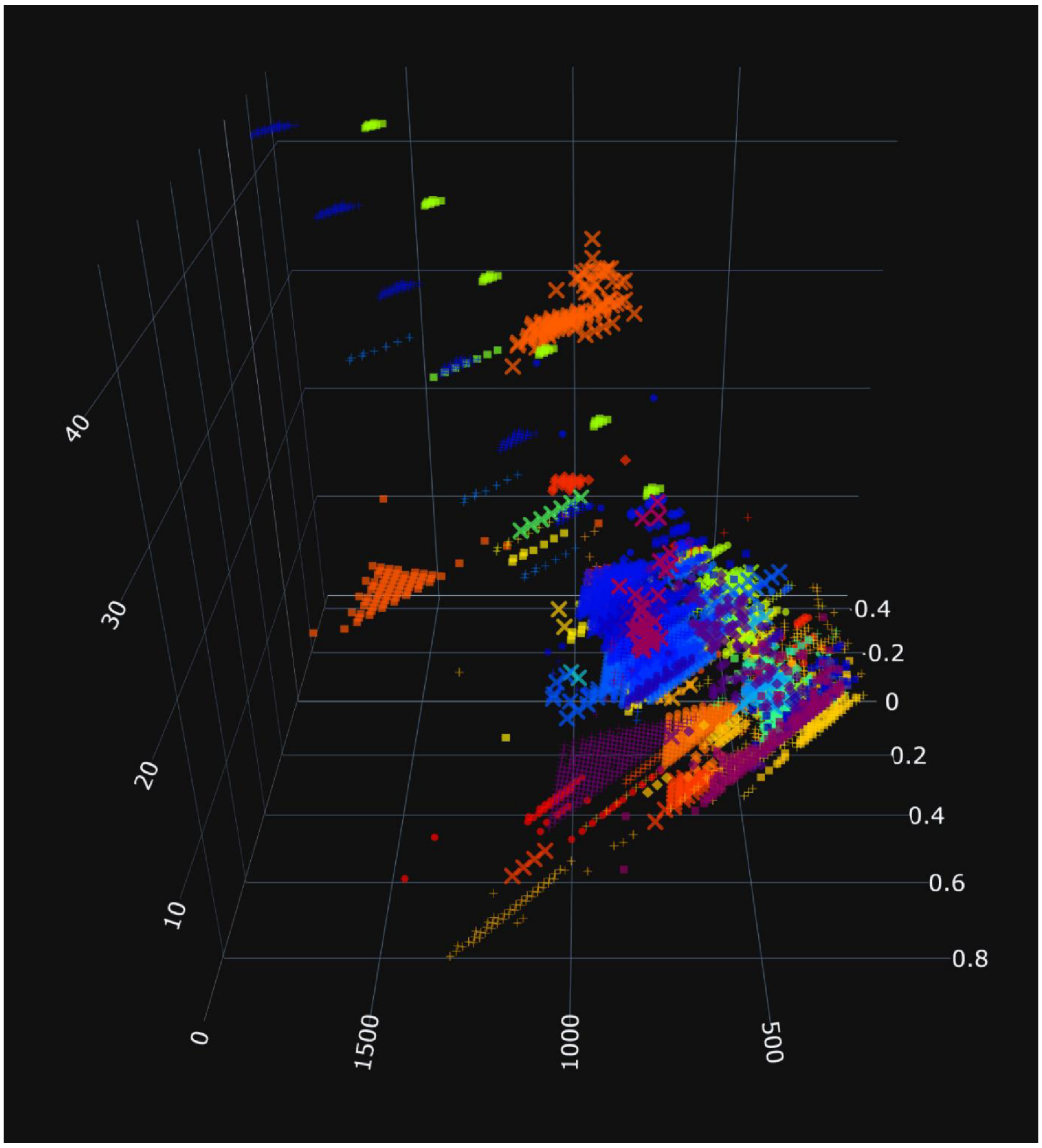

Figure 5.7. Modernized KMD plot illustrating lipids and oxidized lipids from LIPID MAPS®, where each lipid class is represented by a different color and symbol.

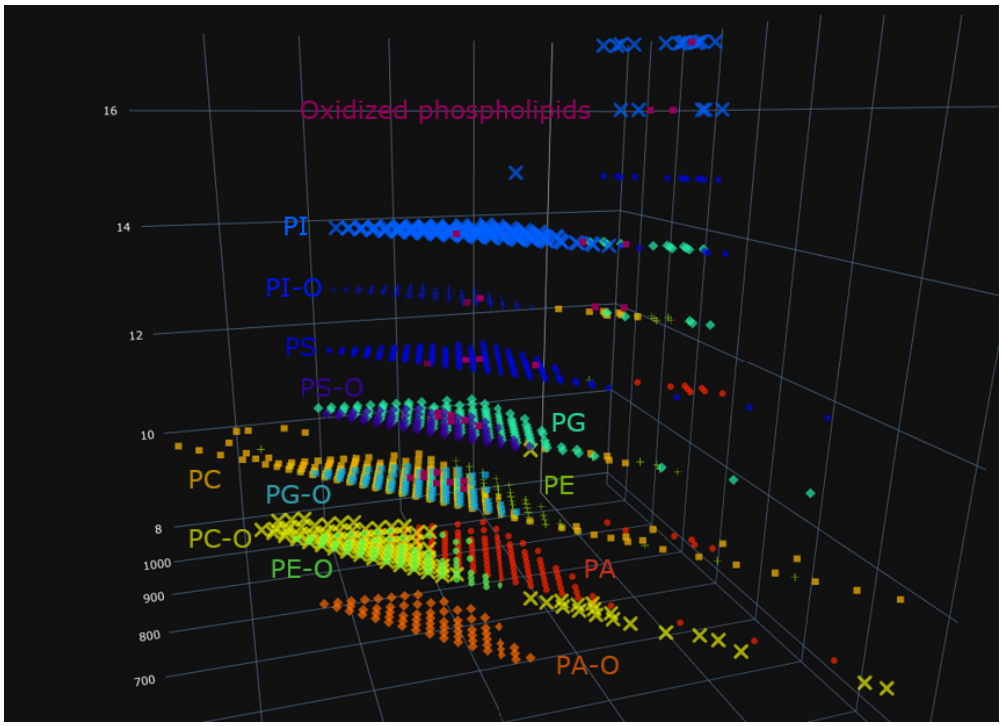

Figure 5.8. Modernized KMD plot illustrating phospholipids and oxidized phospholipids from LIPID MAPS®, where each phospholipid class is represented by a different color and symbol.

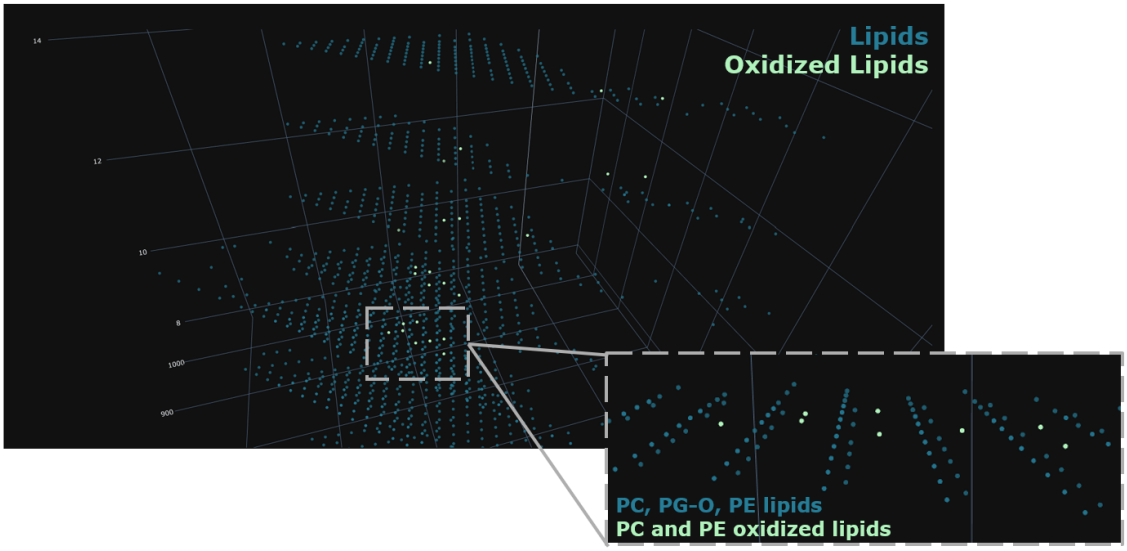

Figure 5.9. Zoomed in visual of modernized KMD plot illustrating separation between phospholipids and oxidized phospholipids from LIPID MAPS.

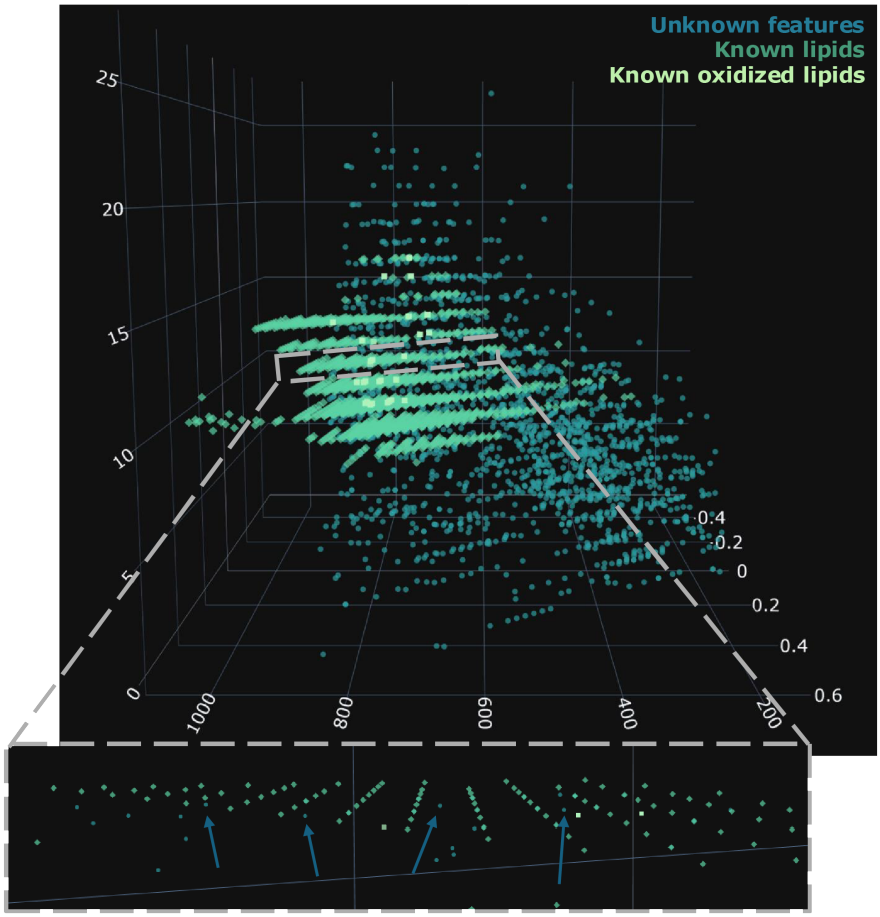

Figure 5.10. Modernized KMD overlay of unknown features, known lipids, and known oxidized lipids. Known features were obtained from LIPID MAPS®. Blue arrows point to features suspected to be oxidized lipids based on their series location.

containing thousands of well-characterized lipids (both oxidized and non-oxidized), it was evident that classic 2D vK and KMD plots were unsuccessful at differentiating many lipid classes and could not distinguish oxidized lipids from non-oxidized lipids. To provide an extra dimension of separation, 3D plots of vK and KMD plots were assessed. KMD plots showed greater success at lipid species separation than vK plots. In fact, a modernized KMD plot, which combined a traditional 2D KMD plot with a third dimensions representing heteroatom count, was the most successful graphical method at differentiating both lipid classes and oxidized lipids. This 3D plot also revealed potential unannotated oxidized lipids in an experimental lipidomics dataset, illustrating its value in untargeted lipidomics studies. Although the generation of these plots are highly useful for drawing conclusions from complex lipids datasets, a lipid classification algorithm based on the coordinates in these plots would be ideal for streamlining data processing. Future work will consist of using Python-based machine learning to classify untargeted lipidomics datasets and predict the lipid class of a data point and whether or not that feature is oxidized.

5.5 Experimental section

The Python codes developed and used for this investigation were based on the *i*-van Krevelen code provided by Kew and co-workers[149], which can be found at https://wkew.github.io/FTMSViz/SRFA-plot.html or https://github.com/wkew/FTMSVisualization. The code used in the current study can be obtained from the Shawn R. Campagna lab (campagna@utk.edu), but a description of the code function can be found in **Appendix Figure 5.11**. Code was initially developed using publicly available data from PubChem (https://pubchem.ncbi.nlm.nih.gov/). Scatter plots in .html format were generated using the Python plotly express package. In this manner, each plot can be interacted with; specifically, certain data points can be investigated, vantage points of 3D plots can be changed, etc. For lipidomics applications, publicly available lipid data was downloaded from LIPID MAPS® (https://www.lipidmaps.org/) and formulated as a database. For experimental datasets, lipidomics data from **Chapter 4** was processed using MS-Dial 4.9[91] and formulae were generated based on exact mass

using SIRIUS version 6.0.5 (https://bio.informatik.uni-jena.de/software/sirius/). Lipid nomenclature can be found at the following website: https://systemsomicslab.github.io/compms/msdial/lipidnomenclature.html.

Appendix

Table 5.1. List of species headgroup and class used for modeling.

Species headgroup	Class
ACer	Lipids
Am-Hex-LPE	Lipids
Am-Hex-PE	Lipids
Am-Hex-PE O	Lipids
AMP	Lipids
CAR	Lipids
CDP-DG	Lipids
CDP-DG dO	Lipids
CE	Lipids
Cer	Lipids
CerP	Lipids
CerPE	Lipids
CL	Lipids
CoA	Lipids
CPA	Lipids
DG	Lipids
DG dO	Lipids
DG O	Lipids
DGCC	Lipids
DGDG	Lipids
DGDG O	Lipids
DGMG	Lipids
DGTA	Lipids
DGTS	Lipids
FA	Lipids
FA O	Lipids
FAHFA	Lipids
FAL	Lipids
FMC-	Lipids

Table 5.1 continued

FOH	Lipids
GlcADG	Lipids
Glc-GP	Lipids
HexCer	Lipids
HexDG	Lipids
Hex-HexNAc-Cer	Lipids
LPS	Lipids
LPS O	Lipids
LSM	Lipids
LSQMG	Lipids
M(IP)C	Lipids
MG	Lipids
MG O	Lipids
MGDG	Lipids
MGMG	Lipids
MGTS	Lipids
MIPC	Lipids
NA	Lipids
NAAla	Lipids
NAArg	Lipids
NAASN	Lipids
NAE	Lipids
NAGln	Lipids
NAGlu	Lipids
NAGly	Lipids
NAHis	Lipids
NAIle	Lipids
NALeu	Lipids
NALys	Lipids
NAMet	Lipids
NAOrn	Lipids

Table 5.1 continued

NAPE	Lipids
NAPhe	Lipids
NAPro	Lipids
NASer	Lipids
NASer:	Lipids
NAT	Lipids
NAThr	Lipids
NAThr L	Lipids
NATrp	Lipids
NATyr	Lipids
PEth	Lipids
PG	Lipids/oxidized lipids
PG dO	Lipids
PG O	Lipids
PGP	Lipids
PI	Lipids/oxidized lipids
PI dO	Lipids
PI O	Lipids
PIM	Lipids
PIP	Lipids
PPA	Lipids
PS	Lipids/oxidized lipids
PS dO	Lipids
PS O	Lipids
PS-NAc	Lipids
PT	Lipids
SFE	Lipids
SHexCer	Lipids
SLBPA	Lipids
SM	Lipids
SPB	Lipids

Table 5.1 continued

SPBP	Lipids
SQDG	Lipids
SQMG	Lipids
SQMG O	Lipids
ST	Lipids
ST:O	Lipids
ST_O	Lipids
TG	Lipids
TG O	Lipids
WD	Lipids
WE	Lipids

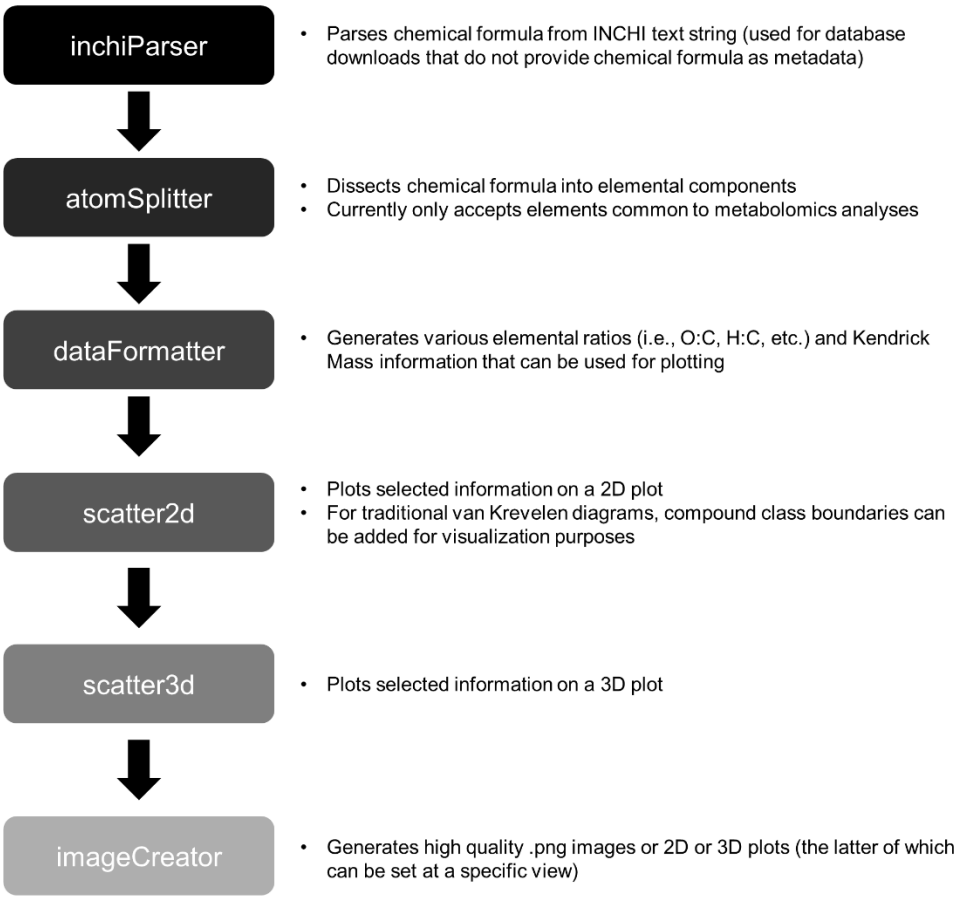

Figure 5.11. Workflow of Python code used to generate van Krevelen and Kendrick Mass plots.

CONCLUSION

In this collection of work, fundamental studies and applications of oxidation in MS were investigated. Specifically, this work delved into two types of oxidation affecting MS: oxidized products stemming from in-source oxidation and biological oxidation. In the first study, the in-source oxidation of hydrocarbons in APCI was explored and proposed to be akin to mechanisms of combustion, producing in-source oxidation products that resemble byproducts of combustion. A novel homolytic mechanism to explain this combustion-like in-source oxidation was proposed, contesting the existing proposed heterolytic mechanisms of in-source oxidation. The next study focused on mitigating the effects of in-source oxidation in order to properly characterize a metabolic cycle (i.e., the AMC) that was prone to oxidation. In this investigation, sulfur-containing metabolites in the AMC were derivatized to prevent chemical transformations in source. The characterization of the AMC combined with other profiling methods (i.e., untargeted metabolomics and lipidomics) lead to the understanding that the formation of AI-2 in *E. coli* was simply a byproduct of metabolism. These data confirmed the notion that this molecule was not used by *E. coli* for quorum sensing, like it is used by other organisms (i.e., *V. harveyi*). A separate study evaluating the downstream effects of biological oxidation derived from oxidative stress was performed on malnourished equine during a rehabilitation program. Here, a clear difference in metabolism was evident between malnourished equine and equine who had progressed beyond the first stage of the rehabilitation program. These data indicated a significant difference in metabolites that were important to liver and kidney function and muscle wasting, suggesting that malnourished equine were severely affected by oxidative stress. In the final study, a novel graphical method to evaluate potential lipid peroxidation in lipidomics data was developed. This data visualization method, which utilizes the series separation of KMD plots with heteroatom content as a third dimension, successfully separated multiple species of lipids in a tiered format. Importantly, this method was also effective in separating non-oxidized and oxidized lipids in both characterized standards and

biological samples. In summary, this body of work presents a comprehensive evaluation of various types of oxidation in MS, offering new insights into in-source oxidation mechanisms, practical strategies for overcoming and evaluating oxidation in MS, and novel methods for distinguishing oxidation thereby advancing the theoretical understanding and practice applications of mass spectrometry in complex mixture analysis.

REFERENCES

(1) Griffiths, J. A Brief History of Mass Spectrometry. *Analytical Chemistry* **2008**, *80* (15), 5678-5683. DOI: 10.1021/ac8013065.

(2) Carroll, D. I.; Dzidic, I.; Horning, E. C.; Stillwell, R. N. Atmospheric Pressure Ionization Mass Spectrometry. *Applied Spectroscopy Reviews* **1981**, *17* (3), 337-406.

(3) Tarr, M. A.; Zhu, J.; Cole, R. B. Atmospheric Pressure Ionization Mass Spectrometry. In *Encyclopedia of Analytical Chemistry*, John Wiley & Sons, L. Ed.; John Wiley & Sons, Ltd., 2006; pp 1-34.

(4) Abdillahi, A. M.; Lee, K. W.; McLuckey, S. A. Mass Analysis of Macro-molecular Analytes via Multiply-Charged Ion Attachment. *Analytical Chemistry* **2020**, *92* (24), 16301-16306. DOI: 10.1021/acs.analchem.0c04335.

(5) Skoog, D. A.; Holler, F. J.; Crouch, S. R. *Principles of instrumental analysis*; Thomson Brooks/Cole, 2007.

(6) Wilm, M. Principles of electrospray ionization. (1535-9484 (Electronic)). From 2011 Jul.

(7) Powers, J. B.; Campagna, S. R. Design and Evaluation of a Gas Chromatograph-Atmospheric Pressure Chemical Ionization Interface for an Exactive Orbitrap Mass Spectrometer. *J Am Soc Mass Spectr* **2019**, *30* (11), 2369-2379. DOI: 10.1007/s13361-019-02311-6.

(8) *Molecular Dissociation Technology Overview*. ThermoFisher Scientific, https://www.thermofisher.com/us/en/home/industrial/mass-spectrometry/mass-spectrometry-learning-center/mass-spectrometry-technology-overview/dissociation-technique-technology-overview.html (accessed 09/10/2024).

(9) Scientific, T. *Mass Analyzer Technology Overview*. https://www.thermofisher.com/us/en/home/industrial/mass-spectrometry/mass-spectrometry-learning-center/mass-spectrometry-technology-overview/mass-analyzer-technology-overview.html (accessed 09/10/2024).

(10) Pitt, J. J. Principles and applications of liquid chromatography-mass spectrometry in clinical biochemistry. (0159-8090 (Print)). From 2009 Feb.

(11) Jones, M. *Gas chromatography - mass spectrometry: a national historic chemical landmark*. https://www.acs.org/education/whatischemistry/landmarks/gas-chromatography-mass-spectrometry.html (accessed 2023.

(12) Fiehn, O. Metabolomics by Gas Chromatography-Mass Spectrometry: Combined Targeted and Untargeted Profiling. (1934-3647 (Electronic)). From 2016 Apr 1.

(13) Brown, T.; LeMay, H.; Burstein, B.; Murphy, C.; Woodward, P. *Chemistry: The Central Science*; Pearson, 2012.

(14) Jones, L.; Laverman, L.; Atkins, P. *Chemical Principles: The Quest for Insight*; W. H. Freeman, 2009.

(15) Xie, X.; Wang, Z.; Li, Y.; Zhan, L.; Nie, Z. Investigation and Applications of In-Source Oxidation in Liquid Sampling-Atmospheric Pressure Afterglow Microplasma Ionization (LS-APAG) Source. *J Am Soc Mass Spectrom* **2017**, *28* (6), 1036-1047. DOI: 10.1007/s13361-016-1550-6.
(16) Pasilis, S. P.; Kertesz, V.; Van Berkel, G. J. Unexpected analyte oxidation during desorption electrospray ionization-mass spectrometry. *Anal Chem* **2008**, *80* (4), 1208-1214. DOI: 10.1021/ac701791w.
(17) Ayrton, S. T.; Jones, R.; Douce, D. S.; Morris, M. R.; Cooks, R. G. Uncatalyzed, Regioselective Oxidation of Saturated Hydrocarbons in an Ambient Corona Discharge. *Angew Chem Int Ed Engl* **2018**, *57* (3), 769-773. DOI: 10.1002/anie.201711190.
(18) Rauf, A.; Khalil, A. A.; Awadallah, S.; Khan, S. A.; Abu-Izneid, T.; Kamran, M.; Hemeg, H. A.; Mubarak, M. S.; Khalid, A.; Wilairatana, P. Reactive oxygen species in biological systems: Pathways, associated diseases, and potential inhibitors-A review. *Food Sci Nutr* **2024**, *12* (2), 675-693. DOI: 10.1002/fsn3.3784 From NLM PubMed-not-MEDLINE.
(19) Main, S. C.; Brown, L. A.-O.; Melvin, K. R.; Campagna, S. R.; Voy, B. A.-O.; Castro, H. F.; Strickland, L. G.; Hines, M. T.; Jacobs, R. D.; Gordon, M. E.; et al. Metabolomic Profiles in Starved Light Breed Horses during the Refeeding Process. LID - 10.3390/ani12192527 [doi] LID - 2527. (2076-2615 (Print)). From 2022 Sep 21.
(20) Ayala, A. A.-O.; Muñoz, M. F.; Argüelles, S. Lipid peroxidation: production, metabolism, and signaling mechanisms of malondialdehyde and 4-hydroxy-2-nonenal. (1942-0994 (Electronic)). From 2014.
(21) Xie, Y.; May, A. L.; Chen, G.; Brown, L. P.; Powers, J. B.; Tague, E. D.; Campagna, S. R.; Loffler, F. E. Pseudomonas sp. Strain 273 Incorporates Organofluorine into the Lipid Bilayer during Growth with Fluorinated Alkanes. *Environ Sci Technol* **2022**, *56* (12), 8155-8166. DOI: 10.1021/acs.est.2c01454.
(22) Xie, Y.; Chen, G.; May, A. L.; Yan, J.; Brown, L. P.; Powers, J. B.; Campagna, S. R.; Loffler, F. E. Pseudomonas sp. Strain 273 Degrades Fluorinated Alkanes. *Environ Sci Technol* **2020**, *54* (23), 14994-15003. DOI: 10.1021/acs.est.0c04029.
(23) Romanczyk, M. Chemical compositional analysis of jet fuels: Contributions of mass spectrometry in the 21st century. *Mass Spectrom Rev* **2022**, e21825. DOI: 10.1002/mas.21825.
(24) Mihelic, R.; Winter, H.; Powers, J. B.; Das, S.; Lamour, K.; Campagna, S. R.; Voy, B. H. Genes controlling polyunsaturated fatty acid synthesis are developmentally regulated in broiler chicks. *Br Poult Sci* **2020**, *61* (5), 508-517. DOI: 10.1080/00071668.2020.1759788.
(25) Manheim, J. M.; Milton, J. R.; Zhang, Y.; Kenttamaa, H. I. Fragmentation of Saturated Hydrocarbons upon Atmospheric Pressure Chemical Ionization Is Caused by Proton-Transfer Reactions. *Anal Chem* **2020**, *92* (13), 8883-8892. DOI: 10.1021/acs.analchem.0c00681.

(26) Rebane, R.; Kruve, A.; Liigand, P.; Liigand, J.; Herodes, K.; Leito, I. Establishing Atmospheric Pressure Chemical Ionization Efficiency Scale. *Anal Chem* **2016**, *88* (7), 3435-3439. DOI: 10.1021/acs.analchem.5b04852.
(27) David, W. J. Applications of Mass Spectrometric Techniques to the Analysis of Fuels and Lubricants. In *Mass Spectrometry*, Mahmood, A. Ed.; IntechOpen, 2017; p Ch. 7.
(28) Chacón-Patiño, M. L.; Gray, M. R.; Rüger, C.; Smith, D. F.; Glattke, T. J.; Niles, S. F.; Neumann, A.; Weisbrod, C. R.; Yen, A.; McKenna, A. M.; et al. Lessons Learned from a Decade-Long Assessment of Asphaltenes by Ultrahigh-Resolution Mass Spectrometry and Implications for Complex Mixture Analysis. *Energy & Fuels* **2021**, *35* (20), 16335-16376. DOI: 10.1021/acs.energyfuels.1c02107.
(29) Romanczyk, M.; Loegel, T. Qualitative characterization of oxygen-containing compounds in fuel extracts by using (-) electrospray ionization coupled to a linear quadrupole ion trap/orbitrap mass spectrometer. *Fuel* **2024**, *359*, 130502. DOI: https://doi.org/10.1016/j.fuel.2023.130502.
(30) Williams, S.; Knighton, W. B.; Midey, A. J.; Viggiano, A. A.; Irle, S.; Wang, Q.; Morokuma, K. Oxidation of Alkyl Ions, CnH2n+1+ (n = 1−5), in Reactions with O2 and O3 in the Gas Phase. *The Journal of Physical Chemistry A* **2004**, *108* (11), 1980-1989. DOI: 10.1021/jp031099+.
(31) Cody, R. B. Aperture Size Influences Oxidation in Positive-Ion Nitrogen Direct Analysis in Real Time Mass Spectrometry. *J Am Soc Mass Spectrom* **2022**, *33* (7), 1329-1334. DOI: 10.1021/jasms.2c00115.
(32) Yang, Z.; Attygalle, A. B. Aliphatic hydrocarbon spectra by helium ionization mass spectrometry (HIMS) on a modified atmospheric-pressure source designed for electrospray ionization. *J Am Soc Mass Spectrom* **2011**, *22* (8), 1395-1402. DOI: 10.1007/s13361-011-0149-1.
(33) Cody, R. B. Observation of molecular ions and analysis of nonpolar compounds with the direct analysis in real time ion source. *Anal Chem* **2009**, *81* (3), 1101-1107. DOI: 10.1021/ac8022108.
(34) Weber, M.; Wolf, J. C.; Haisch, C. Gas Chromatography-Atmospheric Pressure Inlet-Mass Spectrometer Utilizing Plasma-Based Soft Ionization for the Analysis of Saturated, Aliphatic Hydrocarbons. *J Am Soc Mass Spectrom* **2021**, *32* (7), 1707-1715. DOI: 10.1021/jasms.0c00476.
(35) Hagenhoff, S.; Korf, A.; Markgraf, U.; Brandt, S.; Schutz, A.; Franzke, J.; Hayen, H. Screening of semifluorinated n-alkanes by gas chromatography coupled to dielectric barrier discharge ionization mass spectrometry. *Rapid Commun Mass Spectrom* **2018**, *32* (13), 1092-1098. DOI: 10.1002/rcm.8139.
(36) Nunome, Y.; Kodama, K.; Ueki, Y.; Yoshiie, R.; Naruse, I.; Wagatsuma, K. Direct analysis of saturated hydrocarbons using glow discharge plasma ionization source for mass spectrometry. *Talanta* **2019**, *204*, 310-319. DOI: https://doi.org/10.1016/j.talanta.2019.05.115.

(37) Hunt, D. F., Harvey, M.T. Nitric oxide chemical ionization mass spectra of alkanes. *Analytical Chemistry* **1975**, *47* (12), 1965-1969.
(38) Marotta, E.; Paradisi, C. A mass spectrometry study of alkanes in air plasma at atmospheric pressure. *J Am Soc Mass Spectrom* **2009**, *20* (4), 697-707. DOI: 10.1016/j.jasms.2008.12.005.
(39) Starikovskiy, A. Physics and chemistry of plasma-assisted combustion. *Philos Trans A Math Phys Eng Sci* **2015**, *373* (2048). DOI: 10.1098/rsta.2015.0074.
(40) Ju, Y. G.; Sun, W. T. Plasma assisted combustion: Dynamics and chemistry. *Prog Energ Combust* **2015**, *48*, 21-83. DOI: 10.1016/j.pecs.2014.12.002.
(41) Mahle, N. H.; Cooks, R. G.; Korzeniowski, R. W. Hydroxylation of aromatic hydrocarbons in mass spectrometer ion sources under atmospheric pressure ionization and chemical ionization conditions. *Analytical Chemistry* **1983**, *55* (14), 2272-2275. DOI: 10.1021/ac00264a017.
(42) Dutton, J.; Rees, D. B.; Llewellynjones, F. Ionization Coefficients in Helium at High Pressures. *Nature* **1963**, *200* (490), 58-&. DOI: DOI 10.1038/200058a0.
(43) Seol, Y. A.-O.; Choi, M.; Chang, H.; You, S. Study on OH Radical Production Depending on the Pulse Characteristics in an Atmospheric-Pressure Nanosecond-Pulsed Plasma Jet. LID - 10.3390/ma16103846 [doi] LID - 3846. (1996-1944 (Print)). From 2023 May 19.
(44) Timerghazin, Q. K.; Khursan, S. L.; Shereshovets, V. V. Theoretical study of the reaction between ozone and C–H bond: gas-phase reactions of hydrocarbons with ozone. *Journal of Molecular Structure: THEOCHEM* **1999**, *489* (1), 87-93. DOI: https://doi.org/10.1016/S0166-1280(99)00081-0.
(45) Jungkamp, T. P. W.; Smith, J. N.; Seinfeld, J. H. Atmospheric oxidation mechanism of n-butane: The fate of alkoxy radicals. *J Phys Chem A* **1997**, *101* (24), 4392-4401. DOI: DOI 10.1021/jp970212r.
(46) Zeng, J.; Cao, L.; Xu, M.; Zhu, T.; Zhang, J. Z. H. Complex reaction processes in combustion unraveled by neural network-based molecular dynamics simulation. *Nat Commun* **2020**, *11* (1), 5713. DOI: 10.1038/s41467-020-19497-z.
(47) Masunov, A. E.; Wait, E.; Vasu, S. S. Quantum Chemical Study of CH3 + O2 Combustion Reaction System: Catalytic Effects of Additional CO Molecule. *J Phys Chem A* **2017**, *121* (30), 5681-5689. DOI: 10.1021/acs.jpca.7b04897.
(48) Mackay, G. I.; Betowski, L. D.; Payzant, J. D.; Schiff, H. I.; Bohme, D. K. Rate constants at 297.degree.K for proton-transfer reactions with hydrocyanic acid and acetonitrile. Comparisons with classical theories and exothermicity. *The Journal of Physical Chemistry* **1976**, *80* (26), 2919-2922. DOI: 10.1021/j100567a019.
(49) Reisz, E., Naumov, S. The Reaction of Ozone with the C-H Bond Revisited. *Ozone: Science & Engineering* **2024**, 1-15. DOI: 10.1080/01919512.2024.2314603.
(50) Bogaerts, A.; De Bie, C.; Snoeckx, R.; Kozák, T. Plasma based CO2 and CH4 conversion: A modeling perspective. *Plasma Processes and Polymers* **2017**, *14* (6), 1600070.

(51) Wang, W.; Snoeckx, R.; Zhang, X.; Cha, M. S.; Bogaerts, A. Modeling Plasma-based CO2 and CH4 Conversion in Mixtures with N2, O2, and H2O: The Bigger Plasma Chemistry Picture. *The Journal of Physical Chemistry C* **2018**, *122* (16), 8704-8723. DOI: 10.1021/acs.jpcc.7b10619.
(52) Energy, D. o. *Alternative Fuels Data Center*. https://afdc.energy.gov/fuels/properties (accessed 5/23/2024).
(53) Tose, L. V.; Cardoso, F. M. R.; Fleming, F. P.; Vicente, M. A.; Silva, S. R. C.; Aquije, G. M. F. V.; Vaz, B. G.; Romão, W. Analyzes of hydrocarbons by atmosphere pressure chemical ionization FT-ICR mass spectrometry using isooctane as ionizing reagent. *Fuel* **2015**, *153*, 346-354. DOI: https://doi.org/10.1016/j.fuel.2015.03.004.
(54) Valadbeigi, Y.; Causon, T. Significance of Competitive Reactions in an Atmospheric Pressure Chemical Ionization Ion Source: Effect of Solvent. *J Am Soc Mass Spectr* **2022**, *33* (6), 961-973. DOI: 10.1021/jasms.2c00034.
(55) Vendeville, A.; Winzer, K.; Heurlier, K.; Tang, C. M.; Hardie, K. R. Making 'sense' of metabolism: autoinducer-2, LUXS and pathogenic bacteria. *Nature Reviews Microbiology* **2005**, *3* (5), 383-396. DOI: 10.1038/nrmicro1146.
(56) Winzer, K.; Hardie, K. R.; Williams, P. LuxS and autoinducer-2: their contribution to quorum sensing and metabolism in bacteria. *Adv Appl Microbiol* **2003**, *53*, 291-396. DOI: 10.1016/s0065-2164(03)53009-x.
(57) Boban, T.; Nadar, S.; Tauro, S. Breaking down bacterial communication: a review of quorum quenching agents. *Future Journal of Pharmaceutical Sciences* **2023**, *9* (1), 77. DOI: 10.1186/s43094-023-00526-9.
(58) Miller, M. B.; Bassler, B. L. Quorum sensing in bacteria. (0066-4227 (Print)). From 2001.
(59) Moore, L. D.; Le, T.; Fan, G. DNA methylation and its basic function. *Neuropsychopharmacology* **2013**, *38* (1), 23-38. DOI: 10.1038/npp.2012.112.
(60) Bogdanovic, O.; Lister, R. DNA methylation and the preservation of cell identity. *Curr Opin Genet Dev* **2017**, *46*, 9-14. DOI: 10.1016/j.gde.2017.06.007.
(61) Surette, M. G.; Miller, M. B.; Bassler, B. L. Quorum sensing in Escherichia coli, Salmonella typhimurium, and Vibrio harveyi: a new family of genes responsible for autoinducer production. *Proc Natl Acad Sci U S A* **1999**, *96* (4), 1639-1644. DOI: 10.1073/pnas.96.4.1639.
(62) Zhang, X. H.; He, X.; Austin, B. Vibrio harveyi: a serious pathogen of fish and invertebrates in mariculture. (2662-1746 (Electronic)). From 2020.
(63) Cao, J. G.; Meighen, E. A. Purification and structural identification of an autoinducer for the luminescence system of Vibrio harveyi. *J Biol Chem* **1989**, *264* (36), 21670-21676.
(64) Semmelhack, M. F.; Campagna, S. R.; Hwa, C.; Federle, M. J.; Bassler, B. L. Boron binding with the quorum sensing signal AI-2 and analogues. *Org Lett* **2004**, *6* (15), 2635-2637. DOI: 10.1021/ol048976u.
(65) Miller, S. T.; Xavier, K. B.; Campagna, S. R.; Taga, M. E.; Semmelhack, M. F.; Bassler, B. L.; Hughson, F. M. Salmonella typhimurium recognizes a chemically

distinct form of the bacterial quorum-sensing signal AI-2. *Mol Cell* **2004**, *15* (5), 677-687. DOI: 10.1016/j.molcel.2004.07.020.
(66) Chen, X.; Schauder, S.; Potier, N.; Van Dorsselaer, A.; Pelczer, I.; Bassler, B. L.; Hughson, F. M. Structural identification of a bacterial quorum-sensing signal containing boron. *Nature* **2002**, *415* (6871), 545-549. DOI: 10.1038/415545a.
(67) Kendall Melissa, M.; Sperandio, V. Cell-to-Cell Signaling in Escherichia coli and Salmonella. *EcoSal Plus* **2014**, *6* (1), 10.1128/ecosalplus.ESP-0002-2013. DOI: 10.1128/ecosalplus.esp-0002-2013 (acccessed 2024/08/22).
(68) Defoirdt, T.; Sorgeloos, P. Monitoring of Vibrio harveyi quorum sensing activity in real time during infection of brine shrimp larvae. *The ISME Journal* **2012**, *6* (12), 2314-2319. DOI: 10.1038/ismej.2012.58.
(69) Gooding, J. R.; May, A. L.; Hilliard, K. R.; Campagna, S. R. Establishing a quantitative definition of quorum sensing provides insight into the information content of the autoinducer signals in Vibrio harveyi and Escherichia coli. *Biochemistry* **2010**, *49* (27), 5621-5623. DOI: 10.1021/bi1001163.
(70) Xavier, K. B.; Bassler, B. L. Regulation of uptake and processing of the quorum-sensing autoinducer AI-2 in Escherichia coli. (0021-9193 (Print)). From 2005 Jan.
(71) Campagna, S. R.; Gooding, J. R.; May, A. L. Direct quantitation of the quorum sensing signal, autoinducer-2, in clinically relevant samples by liquid chromatography-tandem mass spectrometry. *Anal Chem* **2009**, *81* (15), 6374-6381. DOI: 10.1021/ac900824j.
(72) Halliday, N. M.; Hardie, K. R.; Williams, P.; Winzer, K.; Barrett, D. A. Quantitative liquid chromatography-tandem mass spectrometry profiling of activated methyl cycle metabolites involved in LuxS-dependent quorum sensing in Escherichia coli. *Anal Biochem* **2010**, *403* (1-2), 20-29. DOI: 10.1016/j.ab.2010.04.021.
(73) Kredich Nm Fau - Hershfield, M. S.; Hershfield, M. S. S-adenosylhomocysteine toxicity in normal and adenosine kinase-deficient lymphoblasts of human origin. (0027-8424 (Print)). From 1979 May.
(74) Fukumoto, K.; Ito, K.; Saer, B.; Taylor, G.; Ye, S.; Yamano, M.; Toriba, Y.; Hayes, A.; Okamura, H.; Fustin, J.-M. Excess S-adenosylmethionine inhibits methylation via catabolism to adenine. *Communications Biology* **2022**, *5* (1), 313. DOI: 10.1038/s42003-022-03280-5.
(75) Kanehisa, M.; Goto, S. KEGG: kyoto encyclopedia of genes and genomes. (0305-1048 (Print)). From 2000 Jan 1.
(76) Shetty, S.; Varshney, U. Regulation of translation by one-carbon metabolism in bacteria and eukaryotic organelles. *Journal of Biological Chemistry* **2021**, *296*, 100088. DOI: https://doi.org/10.1074/jbc.REV120.011985.
(77) Shi, L.; Tu, B. P. Acetyl-CoA and the regulation of metabolism: mechanisms and consequences. (1879-0410 (Electronic)). From 2015 Apr.

(78) Leonardi R Fau - Jackowski, S.; Jackowski, S. Biosynthesis of Pantothenic Acid and Coenzyme A. LID - 10.1128/ecosalplus.3.6.3.4 [doi]. (2324-6200 (Print)). From 2007 Apr.
(79) Ryback, B.; Vorholt, J. A. Coenzyme biosynthesis in response to precursor availability reveals incorporation of beta-alanine from pantothenate in prototrophic bacteria. *J Biol Chem* **2023**, *299* (8), 104919. DOI: 10.1016/j.jbc.2023.104919.
(80) Ruby, E. G.; Nealson, K. H. Pyruvate production and excretion by the luminous marine bacteria. *Applied and Environmental Microbiology* **1977**, *34* (2), 164-169. DOI: 10.1128/aem.34.2.164-169.1977 (acccessed 2024/08/20).
(81) Nackerdien, Z. E.; Keynan A Fau - Bassler, B. L.; Bassler Bl Fau - Lederberg, J.; Lederberg J Fau - Thaler, D. S.; Thaler, D. S. Quorum sensing influences Vibrio harveyi growth rates in a manner not fully accounted for by the marker effect of bioluminescence. (1932-6203 (Electronic)). From 2008 Feb 27.
(82) Zhou, T.; Wang, J.; Todd, J. D.; Zhang, X.-H.; Zhang, Y. Quorum Sensing Regulates the Production of Methanethiol in Vibrio harveyi. *Microorganisms* **2024**, *12* (1), 35.
(83) Gooding, J. R. Development and application of liquid chromatography-tandem mass spectrometry methods to the understanding of metabolism and cell-cell signaling in several biological systems. University of Tennessee Knoxville , TRACE: Tennessee Research and Creative Exchange, 2011. https://trace.tennessee.edu/utk_graddiss/1183.
(84) Cronan, J. E.; Thomas, J. Bacterial fatty acid synthesis and its relationships with polyketide synthetic pathways. (1557-7988 (Electronic)). From 2009.
(85) Thomès, L.; Lescure, A. Mosaic Evolution of the Phosphopantothenate Biosynthesis Pathway in Bacteria and Archaea. *Genome Biology and Evolution* **2020**, *13* (2). DOI: 10.1093/gbe/evaa262 (acccessed 8/21/2024).
(86) Baba, T.; Ara T Fau - Hasegawa, M.; Hasegawa M Fau - Takai, Y.; Takai Y Fau - Okumura, Y.; Okumura Y Fau - Baba, M.; Baba M Fau - Datsenko, K. A.; Datsenko Ka Fau - Tomita, M.; Tomita M Fau - Wanner, B. L.; Wanner Bl Fau - Mori, H.; Mori, H. Construction of Escherichia coli K-12 in-frame, single-gene knockout mutants: the Keio collection. (1744-4292 (Electronic)). From 2006.
(87) Rabinowitz, J. D.; Kimball, E. Acidic acetonitrile for cellular metabolome extraction from Escherichia coli. *Anal Chem* **2007**, *79* (16), 6167-6173. DOI: 10.1021/ac070470c.
(88) Chen, L.; Lu, W.; Wang, L.; Xing, X.; Chen, Z.; Teng, X.; Zeng, X.; Muscarella, A. D.; Shen, Y.; Cowan, A.; et al. Metabolite discovery through global annotation of untargeted metabolomics data. *Nature Methods* **2021**, *18* (11), 1377-1385. DOI: 10.1038/s41592-021-01303-3.
(89) Bligh Eg Fau - Dyer, W. J.; Dyer, W. J. A rapid method of total lipid extraction and purification. DOI: D - CLML: 5936:45513:209:311 OTO - NLM From 1959 Aug.
(90) Schmid, R.; Heuckeroth, S.; Korf, A.; Smirnov, A.; Myers, O.; Dyrlund, T. S.; Bushuiev, R.; Murray, K. J.; Hoffmann, N.; Lu, M.; et al. Integrative analysis of

multimodal mass spectrometry data in MZmine 3. *Nat Biotechnol* **2023**, *41* (4), 447-449. DOI: 10.1038/s41587-023-01690-2.
(91) Tsugawa, H.; Cajka, T.; Kind, T.; Ma, Y.; Higgins, B.; Ikeda, K.; Kanazawa, M.; VanderGheynst, J.; Fiehn, O.; Arita, M. MS-DIAL: data-independent MS/MS deconvolution for comprehensive metabolome analysis. *Nature Methods* **2015**, *12* (6), 523-526. DOI: 10.1038/nmeth.3393.
(92) Pang, Z.; Lu, Y.; Zhou, G.; Hui, F.; Xu, L.; Viau, C.; Spigelman, A. F.; MacDonald, P. E.; Wishart, D. S.; Li, S.; et al. MetaboAnalyst 6.0: towards a unified platform for metabolomics data processing, analysis and interpretation. *Nucleic Acids Res* **2024**. DOI: 10.1093/nar/gkae253.
(93) Lenz, T. R. The Unwanted Horse in the United States: An Overview of the Issue. *Journal of Equine Veterinary Science* **2009**, *29* (5), 253-258. DOI: 10.1016/j.jevs.2009.04.001.
(94) Schneider, L. G.; Cox Self, A.; Hines, M. T.; Lin-Zambito Ivey, J. Clinical Factors Associated With Survival Outcomes in Starved Equids: A Retrospective Case Series. *Journal of Equine Veterinary Science* **2021**, *101*, 103370. DOI: 10.1016/j.jevs.2020.103370.
(95) Becvarova, I.; Pleasant, R. S.; Thatcher, C. D. Clinical assessment of nutritional status and feeding programs in horses. *Veterinary Clinics of North America: Equine Practice* **2009**, *25* (1), 1-21.
(96) Stull, C. L.; Hullinger, P. J.; Rodiek, A. V. Fat Supplementation to Alfalfa Diets for Refeeding the Starved Horse. *The Professional animal scientist* **2003**, *19* (1), 47-54. DOI: 10.15232/S1080-7446(15)31375-9.
(97) Merriam-Webster. Malnutrition. **2022**.
(98) Finn, P. F.; Dice, J. F. Proteolytic and lipolytic responses to starvation. *Nutrition.* **2006**, *22* (7-8), 830-844. DOI: 10.1016/j.nut.2006.04.008.
(99) Henneke, D. R.; Potter, G. D.; Kreider, J. L.; Yeates, B. F. Relationship between condition score, physical measurements and body fat percentage in mares. *Equine Veterinary Journal* **1983**, *15* (4), 371-372. DOI: 10.1111/j.2042-3306.1983.tb01826.x.
(100) Dettmer, K.; Aronov, P. A.; Hammock, B. D. Mass spectrometry-based metabolomics. *Mass Spectrometry Reviews* **2007**, *26* (1), 51-78. DOI: 10.1002/mas.20108.
(101) Jiang, P.; Stanstrup, J.; Thymann, T.; Sangild, P. T.; Dragsted, L. O. Progressive Changes in the Plasma Metabolome during Malnutrition in Juvenile Pigs. *Journal of Proteome Research* **2016**, *15* (2), 447-456. DOI: 10.1021/acs.jproteome.5b00782.
(102) Beachler, T. M.; Gracz, H. S.; Morgan, D. R.; Bembenek Bailey, S. A.; Borst, L.; Ellis, K. E.; Von Dollen, K. A.; Lyle, S. K.; Nebel, A.; Andrews, N. C.; et al. Plasma metabolomic profiling of healthy pregnant mares and mares with experimentally induced placentitis. *Equine Veterinary Journal* **2021**, *53* (1), 85-93. DOI: 10.1111/evj.13262.

(103) Escalona, E. E.; Leng, J.; Dona, A. C.; Merrifield, C. A.; Holmes, E.; Proudman, C. J.; Swann, J. R. Dominant components of the Thoroughbred metabolome characterised by¹H-nuclear magnetic resonance spectroscopy: A metabolite atlas of common biofluids. *Equine Veterinary Journal* **2015**, *47* (6), 721-730. DOI: 10.1111/evj.12333.
(104) Keen, B.; Cawley, A.; Reedy, B.; Fu, S. Metabolomics in clinical and forensic toxicology, sports anti-doping and veterinary residues. *Drug Test Anal* **2022**, *14* (5), 794-807. DOI: 10.1002/dta.3245.
(105) Klein, D. J.; Anthony, T. G.; McKeever, K. H. Metabolomics in equine sport and exercise. *Journal of Animal Physiology and Animal Nutrition* **2021**, *105* (1), 140-148. DOI: 10.1111/jpn.13384.
(106) Freemark, M. Metabolomics in Nutrition Research: Biomarkers Predicting Mortality in Children with Severe Acute Malnutrition. *Food and Nutrition Bulletin* **2015**, *36* (1_suppl1), S88-S92. DOI: 10.1177/15648265150361s114.
(107) Yang, Q.-J.; Zhao, J.-R.; Hao, J.; Li, B.; Huo, Y.; Han, Y.-L.; Wan, L.-L.; Li, J.; Huang, J.; Lu, J.; et al. Serum and urine metabolomics study reveals a distinct diagnostic model for cancer cachexia. *Journal of Cachexia, Sarcopenia and Muscle* **2018**, *9* (1), 71-85. DOI: 10.1002/jcsm.12246.
(108) Pusterla, N.; Barnum, S.; Miller, J.; Varnell, S.; Dallap-Schaer, B.; Aceto, H.; Simeone, A. Investigation of an EHV-1 Outbreak in the United States Caused by a New H752 Genotype. *Pathogens* **2021**, *10* (6), 747. DOI: 10.3390/pathogens10060747.
(109) Fleurance, G. R.; Duncan, P.; Mallevaud, B. Daily intake and the selection of feeding sites by horses in heterogeneous wet grasslands. *Animal Research* **2001**, *50* (2), 149-156. DOI: 10.1051/animres:2001123.
(110) O'Connor, C. I.; Nielsen, B. D.; Woodward, A. D.; Spooner, H. S.; Ventura, B. A.; Turner, K. K. Mineral balance in horses fed two supplemental silicon sources. *Journal of Animal Physiology and Animal Nutrition* **2008**, *92* (2), 173-181. DOI: 10.1111/j.1439-0396.2007.00724.x.
(111) Saastamoinen, M.; Sarkijarvi, S.; Suomala, H. Protein Source and Intake Effects on Diet Digestibility and N Excretion in Horses-A Risk of Environmental N Load of Horses. *Animals (Basel)* **2021**, *11* (12). DOI: 10.3390/ani11123568 From NLM PubMed-not-MEDLINE.
(112) Parraga, M. E.; Carlson, G. P.; Thurmond, M. Serum protein concentrations in horses with severe liver disease: a retrospective study and review of the literature. *J Vet Intern Med* **1995**, *9* (3), 154-161. DOI: 10.1111/j.1939-1676.1995.tb03289.x.
(113) Hollis, A. R.; Boston, R. C.; Corley, K. T. Blood glucose in horses with acute abdominal disease. *J Vet Intern Med* **2007**, *21* (5), 1099-1103. DOI: 10.1892/0891-6640(2007)21[1099:bgihwa]2.0.co;2.
(114) Toribio, R. E. Essentials of equine renal and urinary tract physiology. *Vet Clin North Am Equine Pract* **2007**, *23* (3), 533-561, v. DOI: 10.1016/j.cveq.2007.09.006.

(115) Urayama, S.; Arima, D.; Mizobe, F.; Shinzaki, Y.; Nomura, M.; Minamijima, Y.; Kusano, K. Blood glucose is unlikely to be a prognostic biomarker in acute colitis with systemic inflammatory response syndrome in Thoroughbred racehorses. *J Equine Sci* **2018**, *29* (1), 15-19. DOI: 10.1294/jes.29.15.
(116) Klein, R.; Nagy, O.; Tothova, C.; Chovanova, F. Clinical and Diagnostic Significance of Lactate Dehydrogenase and Its Isoenzymes in Animals. *Vet Med Int* **2020**, *2020*, 5346483. DOI: 10.1155/2020/5346483.
(117) Zoppini, G.; Cacciatori, V.; Negri, C.; Stoico, V.; Lippi, G.; Targher, G.; Bonora, E. The aspartate aminotransferase-to-alanine aminotransferase ratio predicts all-cause and cardiovascular mortality in patients with type 2 diabetes. *Medicine (Baltimore)* **2016**, *95* (43), e4821. DOI: 10.1097/MD.0000000000004821.
(118) Ono, T.; Yamada, Y.; Hata, A.; Shimokawa Miyama, T.; Shibano, K.; Iwata, E.; Ohzawa, E.; Kitagawa, H. Reference values of hematological and blood biochemical parameters for the Noma horse. *J Equine Sci* **2019**, *30* (3), 69-73. DOI: 10.1294/jes.30.69.
(119) FIELDER, S. E. *Serum Biochemical Reference Ranges*. Merck, 2015. https://www.merckvetmanual.com/special-subjects/reference-guides/serum-biochemical-reference-ranges (accessed.
(120) Jang, C.; Chen, L.; Rabinowitz, J. D. Metabolomics and Isotope Tracing. *Cell* **2018**, *173* (4), 822-837. DOI: 10.1016/j.cell.2018.03.055.
(121) Ghone, R. A.; Suryakar, A. N.; Kulhalli, P. M.; Bhagat, S. S.; Padalkar, R. K.; Karnik, A. C.; Hundekar, P. S.; Sangle, D. A. A study of oxidative stress biomarkers and effect of oral antioxidant supplementation in severe acute malnutrition. *J Clin Diagn Res* **2013**, *7* (10), 2146-2148. DOI: 10.7860/JCDR/2013/6019.3454.
(122) Foroutan, A.; Fitzsimmons, C.; Mandal, R.; Piri-Moghadam, H.; Zheng, J.; Guo, A.; Li, C.; Guan, L. L.; Wishart, D. S. The Bovine Metabolome. *Metabolites* **2020**, *10* (6), 233. DOI: 10.3390/metabo10060233.
(123) Parenti, M.; McClorry, S.; Maga, E. A.; Slupsky, C. M. Metabolomic changes in severe acute malnutrition suggest hepatic oxidative stress: a secondary analysis. *Nutr Res* **2021**, *91*, 44-56. DOI: 10.1016/j.nutres.2021.05.005.
(124) Wishart, D. S.; Tzur, D.; Knox, C.; Eisner, R.; Guo, A. C.; Young, N.; Cheng, D.; Jewell, K.; Arndt, D.; Sawhney, S.; et al. HMDB: the Human Metabolome Database. *Nucleic Acids Research* **2007**, *35* (Database), D521-D526. DOI: 10.1093/nar/gkl923.
(125) Cohen, S.; Nathan, J. A.; Goldberg, A. L. Muscle wasting in disease: molecular mechanisms and promising therapies. *Nature Reviews Drug Discovery* **2015**, *14* (1), 58-74. DOI: 10.1038/nrd4467.
(126) Schuback, K.; Essén-Gustavsson, B.; Persson, S. G. B. Effect of creatine supplementation on muscle metabolic response to a maximal treadmill exercise test in Standardbred horses. *Equine Veterinary Journal* **2010**, *32* (6), 533-540. DOI: 10.2746/042516400777584578.

(127) Bergero, D.; Assenza, A.; Schiavone, A.; Piccione, G.; Perona, G.; Caola, G. Amino acid concentrations in blood serum of horses performing long lasting low-intensity exercise. *J Anim Physiol Anim Nutr (Berl)* **2005**, *89* (3-6), 146-150. DOI: 10.1111/j.1439-0396.2005.00556.x.
(128) Zhou, Y.; Qiu, L.; Xiao, Q.; Wang, Y.; Meng, X.; Xu, R.; Wang, S.; Na, R. Obesity and diabetes related plasma amino acid alterations. *Clin Biochem* **2013**, *46* (15), 1447-1452. DOI: 10.1016/j.clinbiochem.2013.05.045.
(129) Sarabhai, T.; Roden, M. Hungry for your alanine: when liver depends on muscle proteolysis. *J Clin Invest* **2019**, *129* (11), 4563-4566. DOI: 10.1172/JCI131931.
(130) Ishikawa, T.; Aw, W.; Kaneko, K. Metabolic Interactions of Purine Derivatives with Human ABC Transporter ABCG2: Genetic Testing to Assess Gout Risk. *Pharmaceuticals* **2013**, *6* (11), 1347-1360. DOI: 10.3390/ph6111347.
(131) Kanehisa, M. Toward understanding the origin and evolution of cellular organisms. *Protein Sci* **2019**, *28* (11), 1947-1951. DOI: 10.1002/pro.3715.
(132) Kanehisa, M.; Furumichi, M.; Sato, Y.; Ishiguro-Watanabe, M.; Tanabe, M. KEGG: integrating viruses and cellular organisms. *Nucleic Acids Res* **2021**, *49* (D1), D545-D551. DOI: 10.1093/nar/gkaa970.
(133) Kanehisa, M.; Goto, S. KEGG: kyoto encyclopedia of genes and genomes. *Nucleic Acids Res* **2000**, *28* (1), 27-30. DOI: 10.1093/nar/28.1.27.
(134) Zhang, Y.; Guo, S.; Xie, C.; Fang, J. Uridine Metabolism and Its Role in Glucose, Lipid, and Amino Acid Homeostasis. *BioMed Research International* **2020**, *2020*, 1-7. DOI: 10.1155/2020/7091718.
(135) Paddon-Jones, D.; Børsheim, E.; Wolfe, R. R. Potential Ergogenic Effects of Arginine and Creatine Supplementation. *The Journal of Nutrition* **2004**, *134* (10), 2888S-2894S. DOI: 10.1093/jn/134.10.2888s.
(136) Worley, B.; Halouska, S.; Powers, R. Utilities for quantifying separation in PCA/PLS-DA scores plots. *Analytical biochemistry* **2013**, *433* (2), 102-104.
(137) Klein, C. J.; Stanek, G. S.; Wiles, C. E., 3rd. Overfeeding macronutrients to critically ill adults: metabolic complications. *J Am Diet Assoc* **1998**, *98* (7), 795-806. DOI: 10.1016/S0002-8223(98)00179-5.
(138) Mahmud, I. A.-O.; Kabir, M.; Haque, R.; Garrett, T. A.-O. X. Decoding the Metabolome and Lipidome of Child Malnutrition by Mass Spectrometric Techniques: Present Status and Future Perspectives. (1520-6882 (Electronic)). From 2019 Dec 3.
(139) Squali Houssaïni, F. Z.; Foulon, T.; Payen, N.; Iraqi, M. R.; Arnaud, J.; Groslambert, P. Plasma fatty acid status in Moroccan children: increased lipid peroxidation and impaired polyunsaturated fatty acid metabolism in protein-calorie malnutrition. *Biomedicine & Pharmacotherapy* **2001**, *55* (3), 155-162. DOI: https://doi.org/10.1016/S0753-3322(01)00041-5.
(140) Hansen, S. E. J.; Madsen, C. M.; Varbo, A.; Nordestgaard, B. G. Body Mass Index, Triglycerides, and Risk of Acute Pancreatitis: A Population-Based Study of

118 000 Individuals. *The Journal of Clinical Endocrinology & Metabolism* **2019**, *105* (1), 163-174. DOI: 10.1210/clinem/dgz059 (acccessed 8/30/2024).
(141) Dean, J. M.; Lodhi, I. A.-O. Structural and functional roles of ether lipids. (1674-8018 (Electronic)). From 2018 Feb.
(142) Council, N. R. *Nutrient Requirements of Horses*; National Academic Press, 2007.
(143) Heusner, G. Ad libitum feeding of mature horses to achieve rapid weight gain. In *Proc. 13th Equine Nutr. Physiol. Symp., Gainesville, FL*, 1993; p 86.
(144) Weaver, K.; Feldman, M.; Stewart, C.; Thayer, T. Metabolic responses of chronically starved horses to refeeding with three isoenergetic diets. *J Am Vet Med Assoc* **1998**, *212*, 691-696.
(145) Bazurto, J. V.; Dearth, S. P.; Tague, E. D.; Campagna, S. R.; Downs, D. M. Untargeted metabolomics confirms and extends the understanding of the impact of aminoimidazole carboxamide ribotide (AICAR) in the metabolic network of Salmonella enterica. *Microb Cell* **2017**, *5* (2), 74-87. DOI: 10.15698/mic2018.02.613 From NLM PubMed-not-MEDLINE.
(146) Pang, Z.; Chong, J.; Zhou, G.; David, A.; Chang, L.; Barrette, M.; Gauthier, C.; Jacques, P.-É.; Li, S.; Xia, J. MetaboAnalyst 5.0: narrowing the gap between raw spectra and functional insights. *Nucleic Acids Research* **2021**, *49* (W1), W388-W396. DOI: 10.1093/nar/gkab382.
(147) Krevelen, V. Graphical-statistical method for the study of structure and reaction processes of coal. *Fuel* **1950**, *29*, 269-284.
(148) Rivas-Ubach, A.; Liu, Y.; Bianchi, T. S.; Tolić, N.; Jansson, C.; Paša-Tolić, L. Moving beyond the van Krevelen Diagram: A New Stoichiometric Approach for Compound Classification in Organisms. *Analytical Chemistry* **2018**, *90* (10), 6152-6160. DOI: 10.1021/acs.analchem.8b00529.
(149) Kew, W.; Blackburn, J. W.; Clarke, D. J.; Uhrin, D. Interactive van Krevelen diagrams - Advanced visualisation of mass spectrometry data of complex mixtures. *Rapid Commun Mass Spectrom* **2017**, *31* (7), 658-662. DOI: 10.1002/rcm.7823.
(150) Kendrick, E. A Mass Scale Based on CH2 = 14.0000 for High Resolution Mass Spectrometry of Organic Compounds. *Analytical Chemistry* **1963**, *35* (13), 2146-2154. DOI: 10.1021/ac60206a048.
(151) Hughey, C. A.; Hendrickson, C. L.; Rodgers, R. P.; Marshall, A. G.; Qian, K. Kendrick Mass Defect Spectrum: A Compact Visual Analysis for Ultrahigh-Resolution Broadband Mass Spectra. *Analytical Chemistry* **2001**, *73* (19), 4676-4681. DOI: 10.1021/ac010560w.
(152) Wu, Z.; Rodgers, R. P.; Marshall, A. G. Two- and Three-Dimensional van Krevelen Diagrams: A Graphical Analysis Complementary to the Kendrick Mass Plot for Sorting Elemental Compositions of Complex Organic Mixtures Based on Ultrahigh-Resolution Broadband Fourier Transform Ion Cyclotron Resonance Mass Measurements. *Analytical Chemistry* **2004**, *76* (9), 2511-2516. DOI: 10.1021/ac0355449.

VITA

Lindsay P. Brown became interested in analytical chemistry during the obtainment of her B.S. degree in Chemistry at Appalachian State University from the years 2011 to 2015. She completed undergraduate research under the advisement of Dr. Carol Babyak working on developing methods to detect metals in organic matrices (i.e., biodiesel) using inductively coupled plasma – optical emission spectroscopy. During the summer of 2014, she completed an internship with the Appalachian Energy Center focusing on chemical methods to recycle plastic waste. Prior to graduation, she also completed an internship at Regeneron Pharmaceuticals, Inc. in Rensselaer, NY working under the mentorship of Holly Rousseau. Together, they developed methods to detect contaminants in leachables/extractables samples using gas chromatography – flame ionization detection and investigated processes to increase the efficiency of extracting non-volatile leachables/extractables from biological matrices. At the conclusion of the internship, Lindsay accepted a job offer to work with the QC Analytical Sciences Division under the advisement of Dr. Stacey Helming at Regeneron post-graduation. From 2016 to 2019, Lindsay worked on various projects relating to developing/qualifying QC methods, performing leachables/extractable studies, and supporting product manufacturing – all using mass spectrometry. Thanks to the outstanding mentorship of Dr. Helming, Lindsay developed a passion for mass spectrometry. Lindsay decided to return to academia to obtain a PhD in analytical chemistry focused on mass spectrometry and familial circumstances led her to attend the University of Tennessee Knoxville. Her love for mass spectrometry drew her to the lab of Dr. Shawn Campagna, who was closely associated with the Biological and Small Molecule Mass Spectrometry Core. Here, she was able to perform research focused on mass spectrometry and collaborate on many interdisciplinary projects thanks to consistent funding provided by the University of Tennessee Oak Ridge Innovation Institute.